ABSTRACT

Title of dissertation: NUMERICAL STUDIES
OF QUANTUM CHAOS
IN VARIOUS DYNAMICAL SYSTEMS

Efim Rozenbaum
Doctor of Philosophy, 2020

Dissertation directed by: Professor Victor Galitski
Department of Physics

We study two classes of quantum phenomena associated with classical chaos in a variety of quantum models: (i) dynamical localization and its extension and generalization to interacting few- and many-body systems and (ii) quantum exponential divergences in high-order correlators and other diagnostics of quantum chaos.

Dynamical localization (DL) is a subtle phenomenon related to Anderson localization. It hinges on quantum interference and is typically destroyed in presence of interactions. DL often manifests as a failure of a driven system to heat up, violating the foundations of statistical physics. Kicked rotor (KR) is a prototypical chaotic classical model that exhibits linear energy growth with time. The quantum kicked rotor (QKR) features DL instead: its energy saturates. Multiple attempts of many-body generalizations faced difficulties in preserving DL. Recently, DL was shown in a special integrable many-body model. We study non-integrable models of few- and many-body QKR-like systems and provide direct evidence that DL can persist there. In addition, we show how a novel related concept of localization

landscape can be applied to study transport in rippled channels.

Out-of-time-ordered correlator (OTOC) was proposed as an indicator of quantum chaos, since in the semiclassical limit, this correlator's possible exponential growth rate (CGR) resembles the classical Lyapunov exponent (LE). We show that the CGR in QKR is related, but distinct from the LE in KR. We also show a singularity in the OTOC at the Ehrenfest time t_E due to a delay in the onset of quantum interference. Next, we study scaling of OTOC beyond t_E. We then explore how the OTOC-based approach to quantum chaos relates to the random-matrix-theoretical description by introducing an operator we dub the Lyapunovian. Its level statistics is calculated for quantum stadium billiard, a seminal model of quantum chaos, and aligns perfectly with the Wigner-Dyson surmise. In the semiclassical limit, the Lyapunovian reduces to the matrix of uncorrelated finite-time Lyapunov exponents, connecting the CGR at early times, when the quantum effects are weak, to universal level repulsion that hinges on strong quantum interference. Finally, we consider quantum polygonal billiards: their classical counterparts are non-chaotic. We show exponential growth of the OTOCs in these systems, sharply contrasted with the classical behavior even before quantum interference develops.

NUMERICAL STUDIES OF QUANTUM CHAOS
IN VARIOUS DYNAMICAL SYSTEMS

by

Efim Rozenbaum

Advisory Committee:
Professor Victor Galitski, Chair/Advisor
Professor Christopher Jarzynski
Professor Gretchen Campbell
Professor Jay Deep Sau
Professor James Williams

Dedication

To Ksenia

Acknowledgments

I will begin by expressing my eternal gratitude to my dearly loved, infinitely devoted, and unimaginably wise wife, Ksenia. We walked this road together all the way from being two physics freshmen at St. Petersburg State University (SPbSU) – in my hometown, but some 1400 miles away from hers – to becoming two Doctors of Physics within two consecutive days here, in the U.S., 11 years later. Her role in my life cannot be overestimated.

Next, let me thank my beloved parents, Boris and Inna, who did so much to bring me up to their very high standards of a decent human being and an accomplished professional. My childhood fell on the earliest years of formation of the new country – Russia – on the ruins of the former Soviet Union, and this time was catastrophically hard, with empty shelfs in grocery and all other stores and no decent jobs. And yet my parents always made sure to supply me with everything I needed to succeed.

Next, I'd like to thank Professor Vladimir M. Shabaev and Professor Dmitry A. Telnov. They shaped my early research interests and co-advised my first works as a physicist during my late Bachelor and Master years at the SPbSU in 2010-2014, and it is thanks to this research that I was competitive enough to be admitted to the PhD program at UMD.

I should note that I owe a lot to my wonderful school teachers for the education that I got in St. Petersburg in 2003-2008 at the Lyceum #30 with an emphasis in Physics and Mathematics (as a matter of fact, it is a fantastic versatile school with

an emphasis in most of the subjects, which I always admired and enjoyed). It is this education and the celebrated Russian Olympiad movement that allowed me to get into the most competitive focus group at the SPbSU Physics department (where I also met my wife).

Then, let me acknowledge the people who helped me at various points of my studies and research during PhD: Professor Sriram Ganeshan, Professor Victor Yakovenko, late Professor Shmuel Fishman (his memory will always be with me), Dr. Colin Rylands, Professor Felix Mikhailovich Izrailev, Professor Thomas H. Seligman, a legendary Professor Leonid Abramovich Bunimovich, Professor Christopher Jarzynski, and my advisor, Professor Victor Galitski. I also thank my dissertation committee for their kind support and participation: Professor Christopher Jarzynski, Professor Jay Deep Sau, Professor Gretchen Campbell, Professor James Williams, and my advisor, Professor Victor Galitski. Besides, I can't leave out the contribution of the anonymous referees who devoted their time and efforts to the thoughtful reviews of my papers and helped me quite considerably with their highly appreciated expertise.

I'd like to also extend my gratitude to those who made my life at UMD brighter and showed me other sides of it: Sean (Xiao) Li, Tommy Wyderko, Dennis So Ting Fong, Louise Sumner, Anny Sadler, Albert Shih, Kristina-Maria Constantinou, and many other members of the BAM family.

Finally, I thank Professor Christopher Monroe for helping me out very seriously, when I got stuck in Russia awaiting my U.S. visa renewal for almost 5 months – being already four years into the PhD program. If not for his responsiveness

and unconditional support, it is uncertain whether I would be granted reentry soon enough to continue my PhD (or ever), see my wife again, be able to finish my PhD, and get a job in the U.S.

Table of Contents

List of Figures

List of Abbreviations

BGS   Bohigas-Giannoni-Schmit (conjecture)

CGR   Correlator's growth rate (for the OTOC)

DL   Dynamical localization
DMBL   Dynamical many-body localization (the same as MBDL)

GHD   Generalized hydrodynamics
GOE   Gaussian Orthogonal Ensemble
GUE   Gaussian Unitary Ensemble
GSE   Gaussian Symplectic Ensemble

IOM   Integral of motion

KAM   Kolmogorov-Arnold-Moser
KR   Kicked rotor (also called Chirikov standard map)
KS   Kolmogorov-Sinai (entropy; also called metric entropy)

LE   Lyapunov exponent
LL   Lieb-Liniger (model)
LQKR   Linear (dispersion relation) quantum kicked rotor

MB   Many-body
MBDL   Many-body dynamical localization (the same as DMBL)
MBL   Many-body localization

OTOC   Out-of-time-ordered correlator
OTOO   Out-of-time-ordered operator

RKR   Relativistic kicked rotor

QKR   Quantum kicked rotor
QLE   Quantum Lyapunov exponent
QRKR   Quantum relativistic kicked rotor

TG   Tonks-Girardeau (gas)

WD   Wigner-Dyson (distribution)

List of Publications

The present dissertation (except Chapter 4 and Sec. 5.5) is based on the author's following publications:

1. Efim B. Rozenbaum and Victor Galitski, "Dynamical localization of coupled relativistic kicked rotors," Phys. Rev. B **95**, 064303 (2017).

2. Efim B. Rozenbaum, Sriram Ganeshan, and Victor Galitski, "Lyapunov Exponent and Out-of-Time-Ordered Correlators Growth Rate in a Chaotic System," Phys. Rev. Lett. **118**, 086801 (2017).

3. Efim B. Rozenbaum, Sriram Ganeshan, and Victor Galitski, "Universal level statistics of the out-of-time-ordered operator," Phys. Rev. B **100**, 035112 [Editors' Suggestion] (2019).

4. Efim B. Rozenbaum, Leonid A. Bunimovich, and Victor Galitski, "Early-Time Exponential Instabilities in Non-Chaotic Quantum Systems," arXiv:1902.05466 (2019).

5. Colin Rylands, Efim Rozenbaum, Victor Galitski, and Robert Konik, "Many-Body Dynamical Localization in a Kicked Lieb-Liniger Gas," arXiv:1904.09473 (2019).

Chapter 1:   Introduction

1.1   Quantum Mechanics and Classical Chaos

The first quarter of the twentieth century marked the birth of quantum mechanics, a fundamental theory that described the world on small scales and successfully solved a multitude of puzzles in atomic, optical, and solid state physics, to name a few. The classical physics, thoroughly tested in endless scenarios before, naturally could not be discarded, however, and instead was thought of as a specific limiting case of the quantum theory, the one in which all relevant parameters are far greater than the corresponding "quanta." For example, the typical action would then have to be much larger than the Planck's constant in order for classical mechanics to apply. This implies that under such conditions, the predictions of the classical and quantum theories should agree for all practical purposes. This idea stands behind the famous corresponding principle formulated first by Bohr for atomic energy levels [1] and then assumed for more general physical circumstances. However, the situation with the correspondence principle turned out to be far more complicated than that in another groundbreaking discovery of the early twentieth century, the special relativity, which transforms into the classical mechanics in the limit, in which all relevant speeds are far lower than the speed of light (or the formal

$c \to \infty$ limit). In particular, it turned out that there is no way to introduce quantum theory such that all observables would collapse to the classical predictions in the formal $\hbar \to 0$ limit. This limit is singular, and only certain statistical agreement is achievable, while higher-order correlators cannot generally be matched.

Many "regular" models satisfy the correspondence principle at a certain level of generality. However, as it often happens in science, there appeared to be a "minor" inconsistency that lead to the development of a whole new field of physics. The surprise came from an already enigmatic and exquisite field founded in the late nineteenth century on the intersection between mathematics, physics, and weather prediction. It would later be coined the chaos theory by James A. Yorke [2]. Because of an extremely fast, exponential rate of generation of fine structures in the phase space of chaotic (classical) systems, these structures very quickly reach the scale of finesse at which quantum mechanics operates, and at this point predictions of quantum and classical theories no longer agree. This marks the practical breakdown of the correspondence principle, because formally, the correspondence could only be recovered for so exponentially large systems that even cosmic bodies are not large enough [3]. In other words, in a reasonably short, observable time (typically, the so-called Ehrenfest time t_E [4, 5]), the quantum and classical predictions for the dynamics start to disagree. It would not necessarily be a serious issue, however, if we did not have vast experimental validation that the classical physics predictions are correct and accurate in such scenarios. This is difficult to accept, given that all these large chaotic systems physically consist of small constituents whose behavior is surely governed by quantum, and not classical mechanics.

Two paths can lead from this complication, and both turn out to be possible. In the vastly dominant one, inclusion of more details about the system into a quantum model – such as decoherence by environment or interactions – allows to correctly reproduce physical reality captured by the classical description. There is, however, the second path, following which one attempts to create states of matter, which violate classical predictions even in the semiclassical parameter regime. These attempts require delicate engineering of models and parameter regimes and are easily turned into the former case, though. The essence of both of these opportunities is in examining and defining the characteristics that one would typically regard as sub-dominant, such as many-body effects or weak environment coupling. Of course, the study of quantum systems with classically chaotic counterparts went very far beyond simple dynamics comparison, and many discoveries have been made on the quantum signatures of chaos (see, e.g., Ref. [6]). The field formed around these studies is typically referred to as quantum chaos, although Berry argued that the name "quantum chaology" would be less paradoxical and thus preferential [7], because typically, quantum mechanics washes out many classical chaotic properties after the Ehrenfest time.

1.2   Quantum Kicked Rotor

A periodically driven – kicked – rotor (KR) [also know as Chirikov standard map] [8] is a fundamental classical model that exhibits a transition from mostly regular phase space with small chaotic islands to globally connected chaotic sea

throughout the whole phase space with just small islands of stability. Associated with the chaotic sea, there is a diffusion in the angular-momentum space. KR can be visualized as a particle confined to move on a ring and periodically kicked by an external force in a fixed direction. It can also be thought of as a pendulum, for which the gravity is periodically switched on and off. In case of the usual quadratic dispersion relation, the angular-momentum diffusion translates into the linear energy growth with time. The model's quantum counterpart, the quantum kicked rotor (QKR) [5] is a seminal example of how quantum dynamics can drastically differ from classical one. Instead of the momentum-space diffusion and linear energy growth, QKR demonstrates a complete lack of thereof – dynamical localization (DL) [5, 9, 10], – so that its energy under external drive saturates after a finite time. This and related models are discussed in more details in Chapters 2 and 5.

When generalized to a many-body system, DL means the lack of heating and contradicts the intuitive axioms of statistical physics and thermodynamics. However, multiple attempts of such generalizations faced tremendous difficulties in preserving the localization effect in the presence of interactions or other means of modeling many-body effects, such as via introducing environment/decoherence or non-linearities.

1.3   Dynamical Localization

One of the famous effects that can be attributed to quantum-to-classical correspondence breaking is localization. It has various manifestations in different sys-

tems, but the best known one is Anderson localization in disordered solids [11], which causes zero conductivity. In essence, localization means that the electronic eigenstates in the system are not itinerant – or extended throughout the space, – as is the case in periodic crystals (due to the famous Bloch theorem). Instead, the eigenstates decay exponentially with distance from their core, more similarly to bound states in isolated atoms. A less widely known representative of this family of phenomena is DL [5, 9, 10], mentioned above in Sec. 1.2 – the effect which prohibits energy absorption from an external source and contradicts classical mechanics and statistical physics. In other words, a system does not heat up under external drive. More precisely, it consists in a similar exponential decay of eigenstates, but in the momentum space of a driven dynamical system. The connection between the dynamical and Anderson localization was established formally in Refs. [12, 13, 14, 15] and then further generalized in Ref. [16]. DL is based on a delicate destructive interference, and complications such as interactions, non-linearities, or decoherence typically destroy it. This property can be very useful for creation of various stable quantum devices, such as those for quantum computing, quantum memory, and quantum sensing, to name a few. Fundamentally, replication of this phenomenon in larger systems is also very important, because it directly violates some of the foundations of statistical physics (and thermodynamics) and thereby presents ways around its theorems and rules.

Let us discuss the expectations for this phenomenon in a many-body case. Following the first of two paths outlined in Sec. 1.1, one can account for the fact that there are many degrees of freedom that can exchange energy. Typically, this

consideration is sufficient to rule out localization and restore the usual energy transport consistent with classical and statistical physics. However, as we discover in Chapters 2 and 3, the second path is achievable, too, i.e. systems can be engineered, in which dynamical localization survives interactions and scales to infinite-size systems. We coined this effect Dynamical Many-Body Localization (DMBL) in Chapter 2 and then a bit more precisely – Many-Body Dynamical Localization (MBDL) – in Chapter 3.

1.4 Transport in Rippled Channels and Localization Landscape

A new approach to disordered or irregular systems based on a concept called localization landscape has been suggested recently [17]. It allows one to extract tremendous amount of information about a system without solving its Schrödinger equation and features a dramatically lower complexity than the latter one. In Chapter 4, we test this approach in application to a problem of transport in rippled channels and demonstrate how localization landscape predicts Anderson-like localization in this case and hence the transport properties of a channel.

1.5 Quantum Lyapunov Exponents

One of the fundamental characteristics of chaotic systems is their Kolmogorov-Sinai entropy (KS-entropy) [18, 19, 20], which, due to the Pesin's theorem [21, 22, 23], is usually equal to the sum of all system's positive Lyapunov exponents (LEs). The spectrum of Lyapunov exponents [24, 25] defines whether and to what degree

it is chaotic, as they constitute exponential stretch/squeeze rates along the principal axes in the phase space. Description of quantum-to-classical correspondence and description of quantum systems in general would not be complete without understanding what role these parameters play in the quantum realm. But the very definition of them is problematic in the quantum setting, as it relies on such classical concepts as trajectories, as well as infinite divisibility of the phase space down to arbitrarily small scales, which is not the case in quantum mechanics that imposes the lower limit of $\hbar$ on the phase-space scales. On the other hand, it is natural to expect that in a certain way, the presence of positive Lyapunov exponents should play an important role in dynamics of larger quantum systems. In Chapter 5, we discuss a novel way to calculate these important parameters for general quantum systems based on the so-called out-of-time-ordered correlator (OTOC) [26, 27, 28]. It was suggested that OTOC may serve as a useful characteristic and even an indicator of quantum-chaotic behavior due to its simple interpretation in the semi-classical limit. In particular, in the limit of $\hbar \to 0$, the expression for the rate of possible exponential growth of OTOC resembles the definition of the classical Lyapunov exponent.

We calculate the OTOC for the classical and quantum kicked rotor and compare its growth rate at initial times with the standard definition of the classical Lyapunov exponent. Using both quantum and classical arguments, we show that the OTOC's growth rate and the Lyapunov exponent are in general distinct quantities, corresponding to the logarithm of phase-space-averaged divergence rate of classical trajectories and to the phase-space average of the logarithm, respectively.

The difference appears to be more pronounced in the regime where no classical chaos exists globally. In this case, the Lyapunov exponent quickly decreases with the chaoticity parameter, while the OTOC's growth rate may decrease much slower showing higher sensitivity to small chaotic islands in the phase space. We also show that the quantum OTOC as a function of time exhibits a clear singularity. The underlying physics of this singularity can be related to that in the theory of weak (dynamical) localization and is due to a delay in the onset of quantum interference effects. Finally, we go beyond the Ehrenfest time t_E and demonstrate scaling of the OTOC as a function of time, such that the only dependence of the OTOC on the effective quantum parameter $\hbar_{\text{eff}}$ and time is through a single variable – the combination t/t_E, where the Ehrenfest time t_E is a function of $\hbar_{\text{eff}}$.

1.6   Level Statistics and Lyapunov Operator

One of the most famous and very successful tools developed in quantum chaos and widely accepted within and outside of the field is statistical analysis of energy spectra. And one of the primary types of such analysis consists in calculating the probability density for spacings between adjacent energy levels of a quantum system, known in short as level statistics (this concept comes from the random-matrix theory). This statistical approach allows to discover local correlations within the spectrum. Following the conjecture by Bohigas, Giannoni, and Schmit (BGS conjecture) [29] [1], the quantum systems with Poisson level statistics are identified with classically regular systems and quantum systems with Wigner-Dyson level statistics

---

[1]It was, in fact, first formulated by Casati, Valz-Gris, and Guarneri in Ref. [30]

are identified with classically chaotic ones. This conjecture works very well for many prototypical systems, but does not hold in general. For instance, many quantum models with Wigner-Dyson level statistics do not have a classical counterpart or it is not known (e.g., Sachdev-Ye-Kitaev model [27, 31]) and some classically chaotic dynamical systems acquire Poisson level statistics upon quantization, such as systems that show localization. Moreover, ergodic, but not chaotic classical systems often have quantum counterparts whose level statistics obeys Wigner-Dyson distribution (see, e.g., Ref. [32]).

We explore how the OTOC-based approach to quantum chaos relates to the random-matrix theoretical description, and then we proceed to merge them together. To do so, in Chapter 6 we consider the operator that generates the OTOC (out-of-time-ordered operator, OTOO), and suggest a hybrid diagnostic of chaos in quantum systems: level statistics of the OTOO or level statistics of the Lyapunovian – the operator logarithm of OTOO. This approach proves to be more general and allows to connect early-time classical-like and late-time deeply quantum features associated with chaos. We calculate the Lyapunovian's level statistics explicitly for the quantum stadium billiard, a canonical model of quantum chaos with a textbook classical counterpart – Bunimovich stadium billiard [33, 34, 35, 36, 37, 38, 39] – a seminal model of classical chaos.

We show that in the bulk of the filtered spectrum, the eigenvalue-spacing statistics for the Lyapunovian perfectly aligns with the Wigner-Dyson distribution. One of the advantages of looking at the spectral statistics of this operator is that it has a well-defined semiclassical limit where it reduces to the matrix of uncorrelated

classical finite-time Lyapunov exponents in a partitioned phase space. We provide a heuristic picture interpolating these two limits using Moyal quantum mechanics. Our results show that the Lyapunovian may serve as a useful tool to characterize quantum chaos and in particular quantum-to-classical correspondence in chaotic systems. Specifically, it connects the semiclassical Lyapunov growth at early times, when the quantum effects are weak, to universal level repulsion that hinges on strong quantum interference effects.

1.7   Exponential Divergences in Non-Chaotic Quantum Systems

Having studied Lyapunov exponents extracted from the OTOC in classically chaotic quantum systems, we then turn back to the question of quantum-to-classical correspondence breaking from a particularly intriguing side. Normally, as we mentioned in Sec. 1.1, in chaotic systems with few degrees of freedom, the correspondence is broken shortly after the beginning of the evolution, at the Ehrenfest time, which is logarithmic in the system's size [4, 5]. Exponential instabilities characteristic of chaos vanish around this time, but until then are reproduced in quantum dynamics. However, if the system is not classically chaotic, then one would expect no exponential features in both its classical and quantum dynamics. A series of fundamental examples of violation of these natural expectations is found in Chapter 7, where we consider quantum systems with classical counterparts that are non-chaotic (integrable or ergodic/mixing). We show that the existence of isolated unstable points in classical phase space is sufficient to generate chaotic divergences on the quantum

side – the disagreement that should only become more prominent when the system size is increased and effects of interactions or decoherence are accounted for. It could be regarded as a novel type of quantum-to-classical correspondence breaking, but we prefer to take a more conservative position and interpret this observation as a peculiarity of the OTOC in this kind of scenarios.

Specific calculations are performed for a variety of polygonal billiards, whose classical Lyapunov exponents are always zero, but the quantum OTOC demonstrates a fast exponential-like growth at early times with Planck's-constant-dependent rates. This behavior is sharply contrasted with the slow early-time growth of the analog of the OTOC in the systems' classical counterparts. These results suggest that classical-to-quantum correspondence in dynamics is violated in the OTOC even before quantum interference develops. When interactions or other decoherence-inducing effects are present, the early-time window – defined as the Ehrenfest-time-long time interval after the point when there were no quantum interferences in the system – becomes very important, because the quantum coherence is repeatedly destroyed. Therefore, the correspondence violation should extend to arbitrarily long times in these realistic cases, as far as the OTOC is concerned. Note that the OTOC is ultimately not an observable quantity, at least if we avoid certain additional assumptions, such as a perfect invertibility of time or existence of two perfect copies of a complex quantum system with identical control.

Chapter 2: Dynamical Localization of Coupled Relativistic Kicked Rotors

2.1 Introduction

Since the discovery of Anderson localization in 1958 [11], significant efforts—both analytical and numerical—have been made to understand how localization is affected by interactions. In 2005, Basko, Aleiner, and Altshuler [40] demonstrated that, under certain conditions, localization can survive in the presence of interactions. This phenomenon was called many-body localization (MBL). The MBL state is a peculiar state of matter characterized by a number of counter-intuitive properties including ergodicity breaking [41], and it has been attracting a lot of attention recently (see, e.g., Refs. [42, 43, 44, 45, 46] and references therein; for reviews, see Refs. [47, 48]).

A different but closely related phenomenon to Anderson localization is dynamical localization. It was first introduced by Casati, Chirikov, Ford, and Izrailev [5, 49, 50] for a prototypical dynamical model of quantum kicked rotor (QKR)—a quantum analog of the classical kicked rotor (KR) also known as the Chirikov standard map [5, 8]. Experimentally, it was first observed by Moore *et al.* [51]. Dy-

namical localization manifests itself in quantum suppression of the chaotic classical diffusion, which for KR occurs in the angular-momentum space when the kicking strength exceeds a critical value. As opposed to Anderson localization in disordered systems, dynamical localization is not related to genuine disorder or intrinsic randomness and is a consequence of deterministic system dynamics. However, in 1982 Fishman *et al.* [12] showed that the QKR model can be directly mapped onto the Anderson model with quasidisorder, and that dynamical localization in QKR corresponds to localization in the Anderson-type lattice model. In particular, in the Floquet formalism, the free rotor evolution between the kicks generates a lattice of angular-momentum states (dimensionless angular momentum is integer due to quantization on a ring), and kicking embodies hopping between the "sites" of this lattice.

The role of interactions in both Anderson and dynamical localization has been studied for a long time. During a few decades, it was believed that interactions generally destroy localization due to the associated dephasing. In particular, interactions were studied directly [52, 53, 54, 55, 56, 57, 58, 59, 60, 61, 62, 63, 64, 65, 66], and modeled by introducing noise [67, 68, 69, 70, 71, 72, 73, 74, 75], dissipation [72, 76, 77, 78], and nonlinearity [79, 80, 81, 82, 83, 84, 85, 86, 87, 88]. Some experimental probes [89, 90, 91, 92, 93, 94] also tentatively suggested delocalization. However, in some special cases of two interacting QKRs, dynamical localization was found to be preserved, although weakened—specifically, for a single 2D QKR [95] and for the interaction potential local in rotor angular-momentum space in 1D [96, 97, 98, 99, 100, 101].

Although dynamical localization for two coupled QKRs was predicted to disappear in the presence of coordinate-dependent interactions [52, 53, 64, 65], in 2007 Toloui *et al.* [102, 103] reported localized regimes in two coupled QKRs. Furthermore, recently Keser *et al.* [104] showed that coupled many-body systems can possess dynamical localization, and the corresponding phenomenon was dubbed dynamical many-body localization (DMBL). However, DMBL has been found only for a specific integrable system of linear quantum kicked rotors (LQKRs) so far, and the existence of this phenomenon in more general, nonintegrable cases remains unclear. In this paper, we propose a nonintegrable model of coupled quantum relativistic kicked rotors (QRKRs). We explicitly show dynamical localization for up to three coupled rotors (see Sec. 2.5), and independently of these explicit calculations we argue that the DMBL state in a many-body ensemble of such systems is possible for a wide range of parameters without fine-tuning to integrability. The many-body LQKR Hamiltonian has the form

$$H_{\text{LQKR}}^{\text{MB}} = \sum_{\ell=1}^{L} H_{\ell}^{\text{LQKR}}(p_\ell, x_\ell) + V_{\text{int}}(x_1, \ldots, x_L; t), \qquad (2.1)$$

where the single-particle part $H_{\ell}^{\text{LQKR}}(p_\ell, x_\ell)$ defined in Eqs. (2.5), (2.8), and (2.17) depends on angular momentum linearly as $C_\ell p_\ell$. And this many-body Hamiltonian is a high-angular-momentum limit of the many-body QRKR Hamiltonian given by

$$H_{\text{QRKR}}^{\text{MB}} = \sum_{\ell=1}^{L} H_{\ell}^{\text{QRKR}}(p_\ell, x_\ell) + V_{\text{int}}(x_1, \ldots, x_L; t), \qquad (2.2)$$

14

where $H_\ell^{\text{QRKR}}(p_\ell, x_\ell)$ defined in Eqs. (2.5), (2.7), and (2.8) depends on angular momentum as $\sqrt{(C_\ell p_\ell)^2 + M_\ell^2}$, since

$$\sqrt{(Cp)^2 + M^2} \simeq Cp, \quad \text{as} \ \ Cp/M \to \infty \tag{2.3}$$

(parameter definitions are given below). Therefore, any possible delocalization stops at sufficiently high angular momenta where this asymptotic dominates. On the other hand, outside of this asymptotic regime, the classical counterpart of the QRKR model exhibits chaotic behavior, and a quantum Anderson-type mechanism is necessary to induce localization. We show that this mechanism also works to some extent in the presence of interactions and conclude that in the general many-body case, localization can result from an interplay of both effects.

Apart from the dynamical localization, we also address regimes where the single relativistic kicked rotor exhibits novel transport behavior and examine them in the interacting case. We find that interactions facilitate this behavior and increase the number of such regimes.

New interesting transport effects can be found if the asymptotic behavior of the dispersion relation at low angular momentum is different from the behavior at high angular momentum. In 2003, Matrasulov *et al.* [105, 106] suggested a model of QRKR, a quantum version of a classical relativistic kicked rotor (RKR) [107]. Both RKR and QRKR models naturally possess this dispersion property. It is important to note that from the viewpoint of the dispersion relation, QRKR interpolates between conventional QKR at low angular momenta and exactly solvable LQKR

[13, 108, 109, 110] at high angular momenta. Recently, Zhao *et al.* [111] discovered rich transport properties of RKR and QRKR that included various regimes ranging from localization to superballistic transport.

In general, the transport properties can be classified by the value of the index ν in the time dependence of the mean-squared generalized "coordinate." For a rotor, the relevant choice is the angular-momentum space:

$$\langle p^2 \rangle \sim t^\nu. \tag{2.4}$$

In the case of pure localization $\nu = 0$. The values of $\nu > 0$ correspond to various types of delocalization. $\nu = 1$ corresponds to the standard diffusion $\langle p^2 \rangle \sim t$, while the case $\nu \neq 1$ is called anomalous diffusion. In particular, $\nu \in (0, 1)$ is dubbed subdiffusion and $\nu \in (1, 2)$ is superdiffusion. The regime with $\nu = 2$ corresponds to ballistic transport. There is also a special, less studied case of transient anomalous diffusion called superballistic transport that corresponds to $\nu > 2$. Only a few examples of this regime are known to date [112, 113, 114, 115]. Interestingly, both RKR and QRKR exhibit the superballistic transport regime [111].

Besides the angular-momentum dynamics, QRKR also naturally possesses a spin-like degree of freedom, and dynamics in this "spin" space is quite peculiar (strictly speaking, it is the particle-antiparticle space of the 1D Dirac equation, but we will refer to it as spin for brevity). The first spinful kicked rotor model—spin-1/2 QKR—was suggested by Scharf [116] and later studied in Refs. [117, 118, 119, 120, 121], but the evolution of the spin in either of models did not receive much attention.

16

In the present paper, first we review the QRKR model and introduce its spin dynamics properties that, to the best of our knowledge, have not been discussed in the literature. Then we numerically demonstrate robust localization upon driving for the model with up to 3 interacting QRKRs. Most importantly, it means that in this model interparticle coupling that corresponds to infinite-range interaction in the respective lattice model does not always destroy few-body localization (as opposed to the case in Refs. [52, 53, 54, 55, 56, 57, 58, 59, 60, 61, 62, 63, 64, 65, 66, 67, 68, 69, 70, 71, 72, 72, 73, 74, 75, 76, 77, 78, 79, 80, 81, 82, 83, 84, 85, 86, 87, 88, 90, 91, 94], but similarly to the one in Refs. [102, 103]). More generally, we show that the coupled model inherits the transport regimes of the single QRKR model. If generalized to a many-body system of QRKRs, this statement results in DMBL similar to that found in Ref. [104], but for a nonintegrable system. Independently of the numerics, but in agreement with it, we argue that this is the case because the difference between the dynamics of the many-body QRKRs model and the integrable model considered in Ref. [104] vanishes as the angular-momentum terms increase and overwhelm the mass terms.

2.2   Quantum Relativistic Kicked Rotor

In this section, we review the QRKR model (see also Ref. [111]) and study the spin dynamics and spin-momentum entanglement in this model. We find a number of unusual dynamic regimes involving the spin. From this point on, we mostly refer to the rotors' angular momenta simply as momenta for shortness.

As for any kicked system, the Hamiltonian of the QRKR model reads

$$\hat{H}(t) = \hat{H}_0 + V \sum_{n=-\infty}^{\infty} \delta(t-n), \qquad (2.5)$$

where t is a dimensionless time (measured in the units of the kicking period, T). Throughout the paper, we use the notation

$$\Delta(t) \equiv \sum_{n=-\infty}^{\infty} \delta(t-n). \qquad (2.6)$$

For QRKR, the free part $\hat{H}_0$ is the dimensionless 1D Dirac Hamiltonian:

$$\hat{H}_0(p) = 2\pi\alpha p\hat{\sigma}^x + M\hat{\sigma}^z, \qquad (2.7)$$

$$V(x) = K\cos(qx), \qquad (2.8)$$

where K is an effective kicking strength, and $q \in \mathbb{N}$ specifies the spatial period of the potential. Note that the kicking potential (2.8) is proportional to the unit matrix in the spin space.

In order to quantify the role of quantum and relativistic effects in QRKR as compared to RKR and QKR, respectively (see Sec. 2.5 for the coupled rotors case), we make connection to the actual Dirac equation for a kicked relativistic spin-1/2 particle of mass m confined to a 1D ring of radius R:

$$i\hbar\frac{\partial}{\partial t_p}\Psi = \left[cp_p\hat{\sigma}^x + mc^2\hat{\sigma}^z + kR\cos(qx)\Delta\left(\frac{t_p}{T}\right) \right]\Psi, \qquad (2.9)$$

18

where $t_p = tT$ is physical time, c is the speed of light, $p_p = \hbar p / R$ is physical (linear) momentum, and k is the amplitude of the kicking force. Introduce a dimensionless "effective Planck constant":

$$\hbar_{\text{eff}} = \frac{\hbar T}{mR^2}.$$ (2.10)

In the dimensionless Dirac equation, we absorb $\hbar_{\text{eff}}$ into the other parameters, so that the Hamiltonian (2.5), (2.7), (2.8) enters it as follows:

$$i\frac{\partial}{\partial t}\Psi = [Cp\hat{\sigma}^x + M\hat{\sigma}^z + K\cos(qx)\Delta(t)]\,\Psi,$$ (2.11)

where

$$C \equiv 2\pi\alpha = \frac{cT}{R},$$ (2.12)

$$M = \frac{mc^2T}{\hbar} = \frac{C^2}{\hbar_{\text{eff}}},$$ (2.13)

$$K = \frac{kTR}{\hbar} = \frac{K_{\text{RKR}}}{\hbar_{\text{eff}}},$$ (2.14)

and K_{RKR} is the dimensionless kicking strength in the nonquantum RKR model [see Eq. (2.20) below]. Note that this straightforward interpretation is not related to the feasible physical realizations. Some of the latter are proposed in Sec. 2.6.

Consider integer times t only. Since the Hamiltonian is periodic in time—$H(t+1) = H(t)$—and the external potential has a kicking form, the stroboscopic single-period evolution of the wave functions governed by Eq. (2.11) is given by the Floquet operator $\hat{F}$ as

$$\Psi(t+1) = \hat{F}\Psi(t),$$ (2.15)

19

where

$$\hat{F} = \exp\left[-i\hat{H}_0(p)\right]\exp\left[-iV(x)\right] \tag{2.16}$$

$$= \exp\left[-i\left(2\pi\alpha p\hat{\sigma}^x + M\hat{\sigma}^z\right)\right]\exp\left[-iK\cos(qx)\right].$$

An efficient way of calculating the evolution (2.15) numerically is by switching from the coordinate representation to the momentum representation back and forth, applying each part of the Floquet operator (2.16) in its eigenbasis. This approach allowed us to reproduce the results for single QRKR obtained in Ref. [111]. The details of the numerical implementation of this method are given for coupled QRKRs in Sec. 2.4.

As we mentioned above, in the high-momentum region the QRKR model can be approximated by the LQKR model. It is determined by Hamiltonian (2.5) with the free part:

$$H_0^{\text{LQKR}}(p) = 2\pi\alpha p \tag{2.17}$$

and kicking potential (2.8). This model has been proved to be integrable in any dimension by Figotin and Pastur [122].

During the free evolution between the kicks, the local eigenspinors of $\hat{H}_0(p)$, i.e. the eigenspinors at any given p as a parameter, acquire the phases $\varphi_\pm(p) = \pm\sqrt{(2\pi\alpha p)^2 + M^2}$, where the quantized momentum p takes only integer values. As discussed in Ref. [111], the transport regime in QRKR is determined by the phases $\varphi_\pm(p)$ along with the kicking potential parameter q and initial conditions. Specifically, in the low-

momentum region ($2\pi\alpha p \ll M$), QRKR is always localized (for the same reason as QKR and LQKR), because propagators $\exp[-i\varphi_\pm(p)]$ act as quasi-random-number generators for a sequence of integers p. In the high-momentum limit, QRKR tends to LQKR, and the behavior of $\exp[-i\varphi_\pm(p)]$ is determined by the rationality of α. Namely, irrational values of α give rise to the localized phase, and rational values—$\alpha = r/s$ ($r, s \in \mathbb{Z}$ are relatively prime)—lead to delocalization (in particular, to ballistic transport) if $q/s \in \mathbb{Z}$. In the remaining case of $\alpha = r/s$, but $q/s \notin \mathbb{Z}$, the dynamics is bounded, but this is not related to the Anderson-type localization [109, 111]. In the general case of the wave function containing components with $2\pi\alpha p \sim M$, an additional pattern—the superballistic transport—arises due to the leakage of the wave function from the low-momentum region to the high-momentum one [111]. Specifically, following the qualitative argument from Ref. [111], there are three contributions to the momentum-space transport. One contribution is constant and comes from localization in the disordered region at small momenta. Another one is ballistic; i.e., the momentum variance grows quadratically in time. It comes from the periodic nondisordered (in terms of $\exp[-i\varphi_\pm]$) high-momentum region. And the third contribution is superballistic. It is related to the transfer of population from the moderate-momentum to the high-momentum region and can be qualitatively described by $\int_0^t dt' \Gamma(t-t')Dt'^2$, where $\Gamma(t)$ is a population transfer rate and D is a coefficient of ballistic transport. In the simplest case of $\Gamma(t) \approx$ const, this integral readily gives cubic growth of momentum variance.

Besides the rich dynamics that QRKR shows in the momentum space, it also possesses very peculiar patterns in spin dynamics, even if the kicking is spin-

independent, as in Eq. (2.8). These patterns are related to the entanglement between the spin and momentum degrees of freedom that occurs at each step as a result of the combination of free evolution and kicking. We performed a series of calculations of the spin evolution in the case of spin-independent kicking (2.8). In Figs. 2.1 – 2.3 and 2.6, we show trajectories of the tip of the spin vector—more precisely, the vector $2\,\mathbf{s}(t) = \langle\Psi(t)\,|\hat{\sigma}|\,\Psi(t)\rangle$ —within the Bloch sphere in four representative regimes. Figs. 2.1 – 2.3 correspond to the localized phase, while Fig. 2.6 describes the spin dynamics in the delocalized phase. As an initial state, we chose a Gaussian $\Psi(p, t = 0) \sim \exp\left[-(p - p_0)^2/(2\Delta_p^2)\right]\chi_\sigma$, where $\chi_\sigma = |\uparrow\rangle + i\,|\downarrow\rangle$ in Fig. 2.1 and $\chi_\sigma = |\uparrow\rangle$ in all other cases.

In Fig. 2.1, $M/2\pi\alpha$ is much larger than the initial momentum spread centered around zero, and due to localization, the mass remains two orders of magnitude greater than $2\pi\alpha p$ for the highest populated momentum components. In this case, the spin-tip trajectory is a flat disk that lies in the XY plane and constitutes rotation via $\exp\left[-iM\hat{\sigma}^z\right]$. The radius of the spin trajectory is determined by the degree of the spin-momentum entanglement and is oscillating in time within certain boundaries.

In Fig. 2.2, the mass M and the initial momentum p_0 are equal, which leads to the flat trajectory tilted at an angle—$\tan(\theta) \approx M/(2\pi\alpha p_0) = 1/(2\pi\alpha)$—to the YZ plane. When the ratio between $2\pi\alpha p_0$ and M is varied, the trajectory remains flat in a certain range of parameters, and only tilt angle changes accordingly.

In Fig. 2.3, $2\pi\alpha p_0 \gg M$, and the momentum spread $\Delta_p \gg M$. In this case, we have alternating regimes of dynamics. When the majority of the momentum-space population is far away from $p = M/(2\pi\alpha) \ll p_0$, the spin-tip trajectory
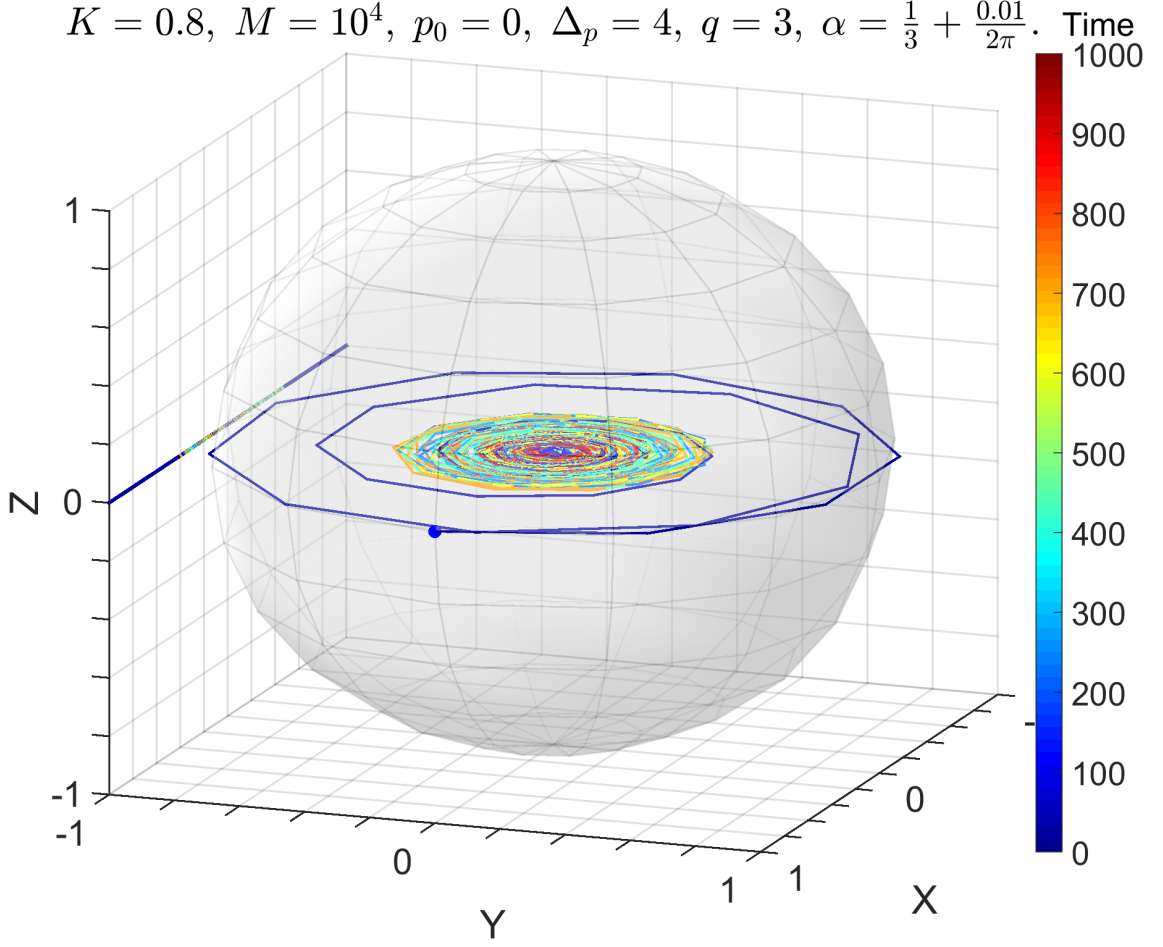
Figure 2.1: Spin dynamics with a large mass, zero average initial momentum, and small initial momentum-distribution width Δ_p (parameters are shown above the figure). The blue marker indicates the initial point, and the color indicates time (in the units of the kicking period). The projection of the spin trajectory is shown on the XZ coordinate plane.

is flat—in this case, it constitutes rotation in the YZ plane due to the action of $\exp\left[-i2\pi\alpha p\hat{\sigma}^x\right]$. The wave function dynamics far away from $p = M/(2\pi\alpha)$ consists of periodic splitting into two parts and recombining back. One of these parts corresponds to classical acceleration due to in-phase kicking and another one—to deceleration due to out-of-phase kicking. As a manifestation of localization, these parts span only very limited vicinity of the initial wave packet; Fig. 2.4(a) shows these parts at the largest separation alongside the initial state. When the wave
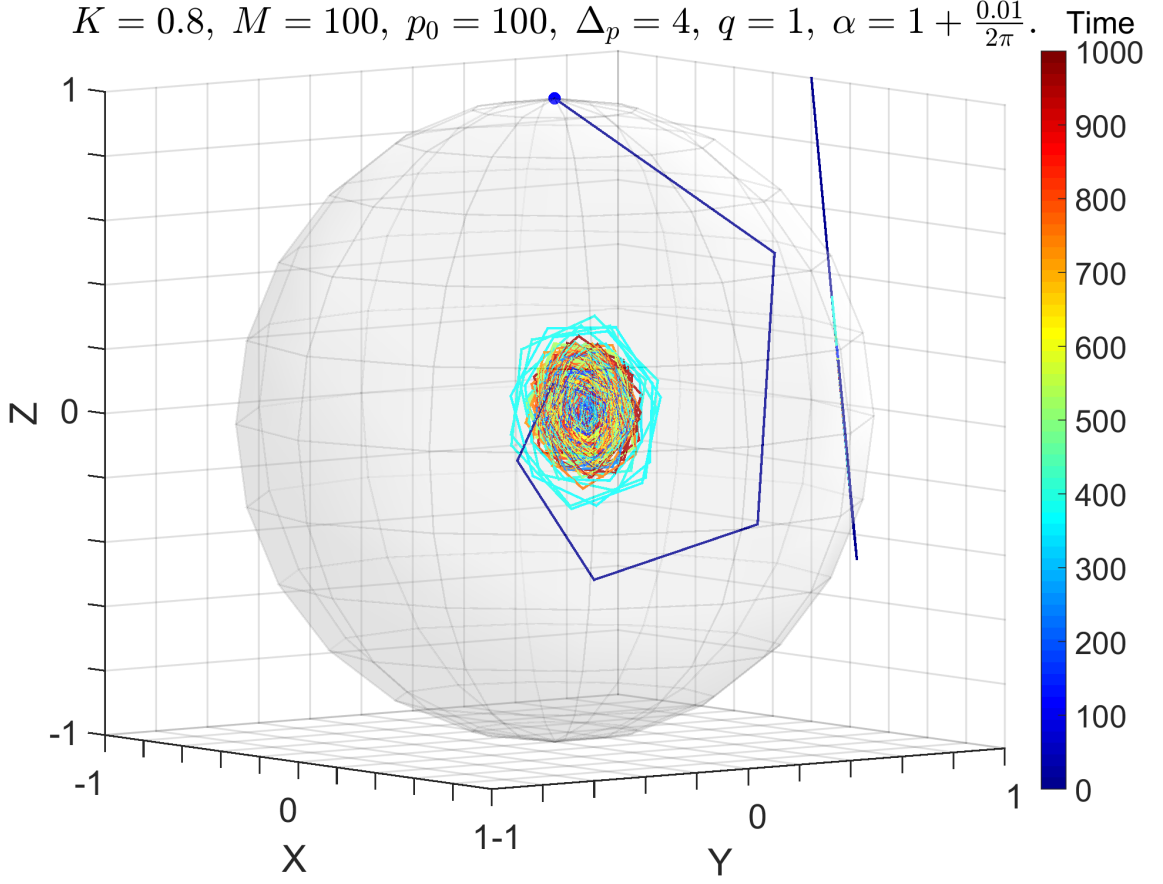
Figure 2.2: Spin dynamics with a medium mass equal to the average initial momentum, and small initial momentum-distribution width Δ_p (parameters are shown above the figure). The blue marker indicates the initial point, and the color indicates time. The projection of the spin trajectory is shown on the XZ coordinate plane.

function components are split, the spin tip stays very close to some point X_0 at the X axis. And when the components recombine, the spin tip comes to the surface of the Bloch sphere developing a flat part of the trajectory that is parallel to the YZ plane and crosses the point X_0. However, if the initial wave function is centered close enough to $p = M/(2\pi\alpha)$, as is the case in Fig. 2.3, one of the split components goes through this point, and the spin tip starts to move along the X axis until that component leaves the vicinity of $p = M/(2\pi\alpha)$. Once the components of the wave function recombine, a new flat disk parallel to YZ plane develops, and then
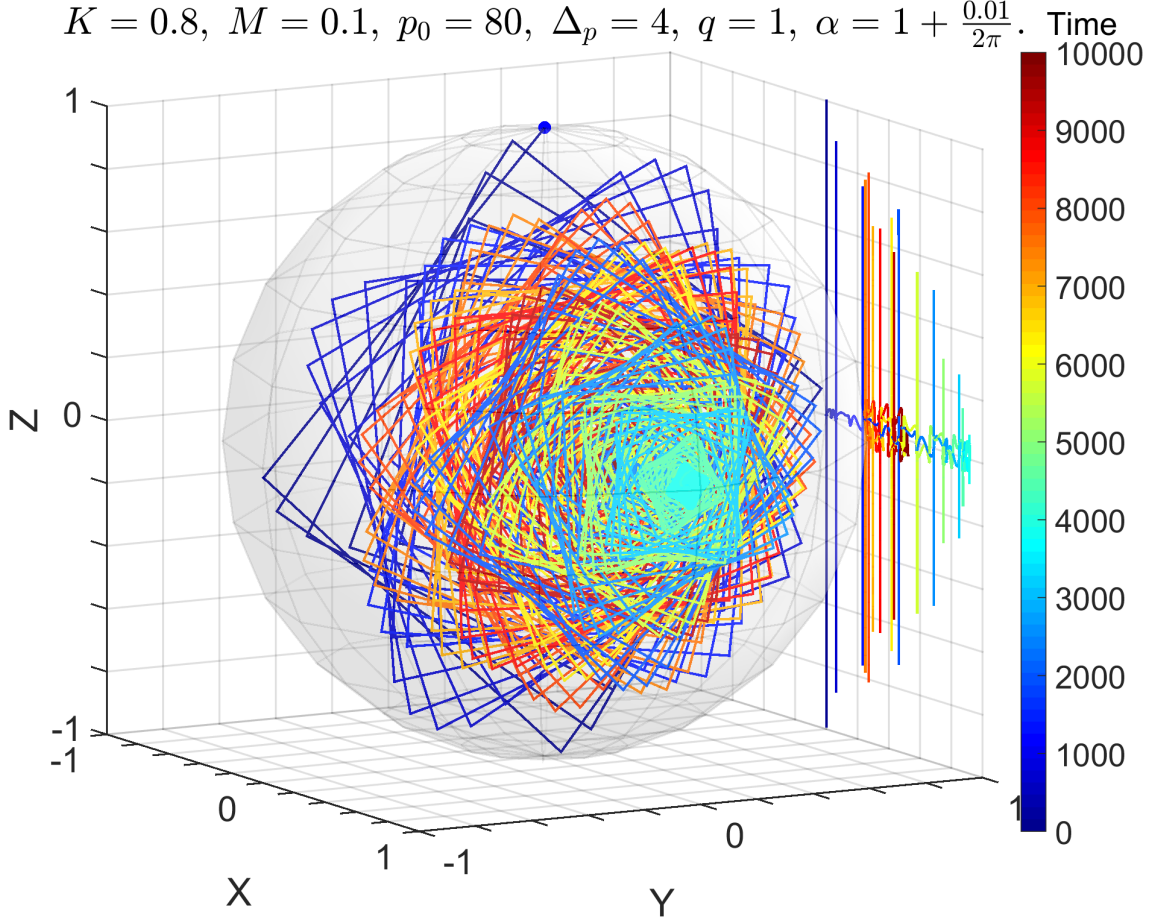
Figure 2.3: Spin dynamics with a small mass, high average initial momentum, and medium initial momentum-distribution width Δ_p (parameters are shown above the figure). The blue marker indicates the initial point, and the color indicates time. The projection of the spin trajectory is shown on the XZ coordinate plane.

this periodic pattern continues with the X-motion until the next disk is generated.

When the motion along the X axis brings the spin tip to the surface of the Bloch

sphere, the X-motion reflects off it and continues back to the center of the Bloch

sphere. During this motion, each time a nonvanishing part of the wave function

passes through $p = M/(2\pi\alpha)$, it gets modulated, split, and eventually becomes very

noisy in that region [see Figs. 2.4(b)–2.4(d)]. In Fig. 2.5, we show the entanglement

entropy as a function of time corresponding to this case. It is defined as
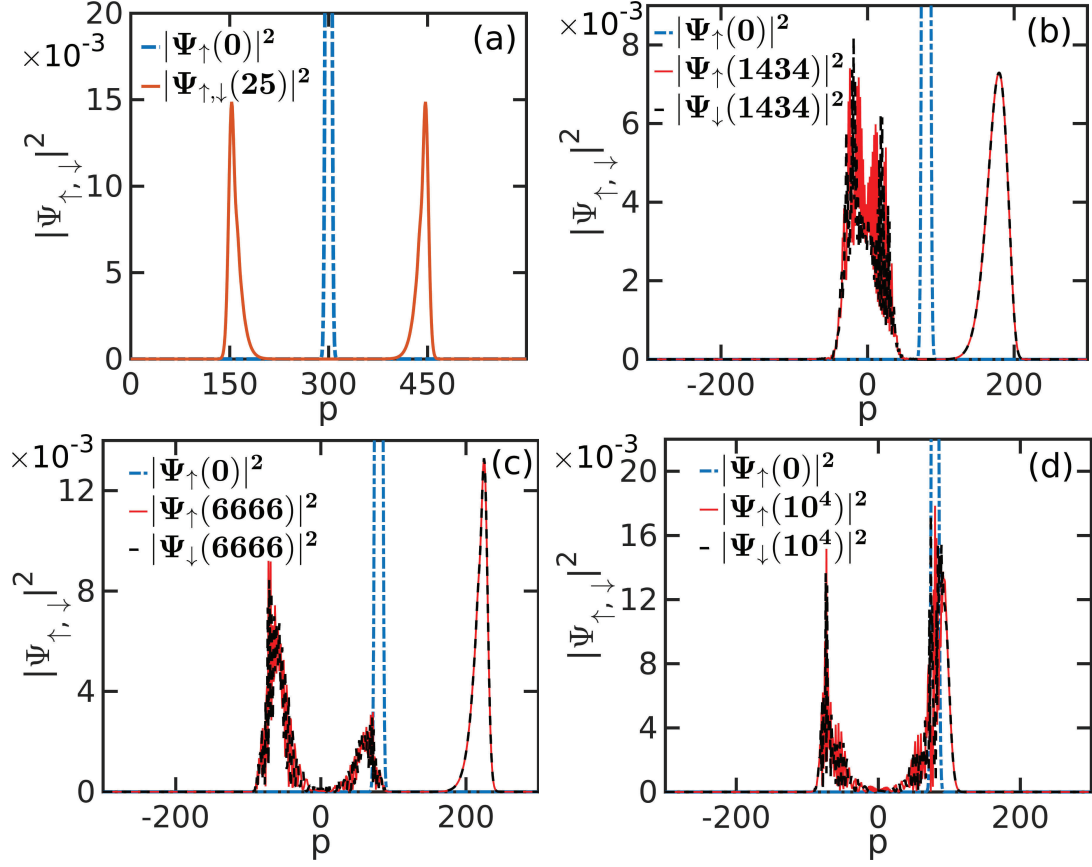
Figure 2.4: Wave function at different stages of evolution with the same parameters as in Fig. 2.3. Panel (a) shows the initial wave function (dot-dashed blue line) and that at $t = 25$ (solid red line) in case of starting at $p_0 = 300$—very far from $p = M/(2\pi\alpha)$. Panels (b)–(d) exactly correspond to Fig. 2.3 and show the initial wave function (dot-dashed blue lines) and the up and down spinor components (solid red and dashed black lines, respectively) at the times indicated in the parentheses. The initial down component is zero.
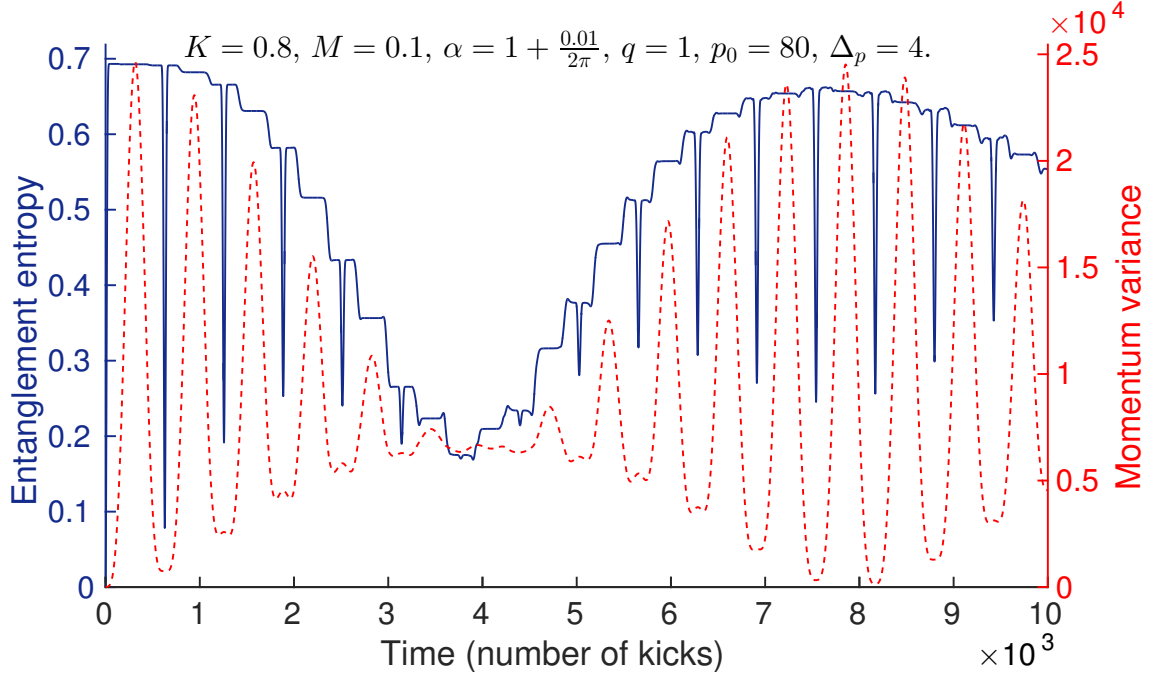
Figure 2.5: Entanglement entropy (solid blue line, left axis) and momentum variance ($\langle p^2\rangle - \langle p\rangle^2$) (dashed red line, right axis) in the process corresponding to Fig. 2.3. Parameters are shown above the figure.

$$S(t) = -\mathrm{tr}\left[\rho_s(t)\ln\rho_s(t)\right], \qquad (2.18)$$

where

$$\rho_s(t) = \sum_{p=-\infty}^{\infty} |\Psi(p,t)\rangle \langle\Psi(p,t)| . \qquad (2.19)$$

The sharply pronounced dips in the entanglement entropy correspond to the flat disk structures in the Bloch sphere with their edges coming close to the surface of the sphere. And the envelope of the entanglement entropy corresponds to the motion of the spin tip along the X axis. As the time goes, the wave function becomes more and more noisy, and no sharp disk structures are generated for some time. This corresponds to the region between 3000 and 5000 kicks in Figs. 2.3 and 2.5. However, at some point, the revival of the disks structure in the Bloch sphere occurs,

27

and the corresponding revival of the dips structure in the entanglement entropy can be seen. As the wave function goes through the point $p = M/(2\pi\alpha)$ many times, it splits again, and becomes randomized, so that eventually, the motion within the Bloch sphere becomes less regular. However, it retains the features described above for at least as long as 2×10^4 kicks.

Fig. 2.6 shows the spin dynamics in the case of resonant value of α, i.e., delocalization in the momentum space. In this regime, the motion of the spin tip is continuously slowing down. As time goes, more and more momentum components get populated, and the spin-tip trajectory tends to one limiting point inside the Bloch sphere.

2.3   Critical kicking strength in RKR

Before discussing coupled QRKRs, we need to address the difference between the classical models of RKR and nonrelativistic KR with respect to the notion of critical kicking strength. RKR is described by the dimensionless Hamiltonian:

$$H_{\mathrm{RKR}} = C^2\sqrt{1 + \frac{p^2}{C^2}} + K_{\mathrm{RKR}}\cos(qx)\Delta(t). \qquad (2.20)$$

According to Ref. [107], as opposed to KR, in RKR, different Kolmogorov-Arnold-Moser (KAM) tori in the phase space are destroyed at different critical values of the kicking strength $K_{\mathrm{RKR}}^{i,\mathrm{cr}}$, which depend on the parameter C. Most importantly, there are global limiting tori at high momentum that do not get destroyed at any finite value of K_{RKR} if $C/2\pi \equiv \alpha \notin \mathbb{Z}$ (the latter condition is always satisfied in the
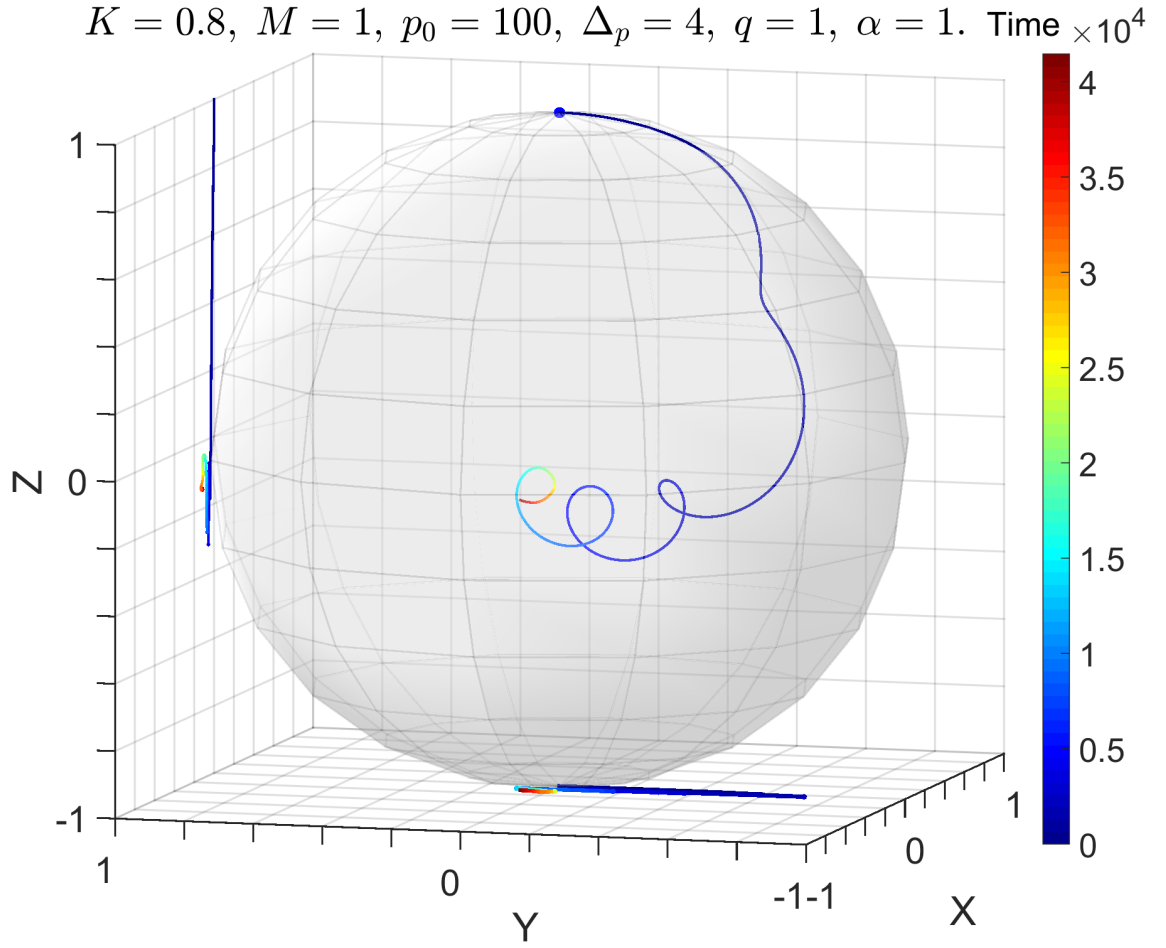
Figure 2.6: Spin dynamics in a resonant regime corresponding to delocalization (α is rational). Parameters are shown above the figure. The blue marker indicates the initial point, and the color indicates time. The projections of the spin trajectory are shown on the XY and XZ coordinate planes.
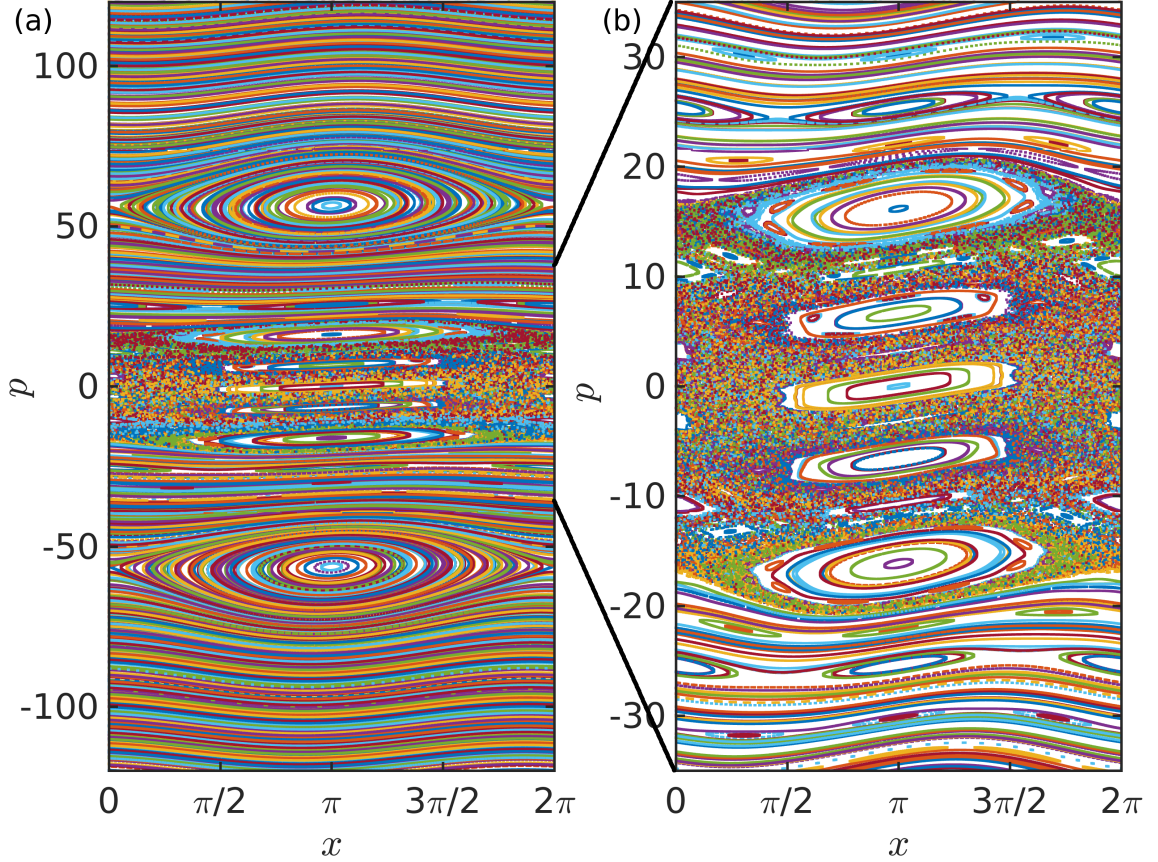
Figure 2.7: Phase map of RKR in a moderate kicking regime. Parameters: $C = 20$, $K_{\mathrm{RKR}} = 2$, $q = 1$. Panel (b) shows zoomed region of moderate angular momenta from panel (a). At low momenta, there are both chaotic and periodic trajectories. At high momenta, all trajectories are periodic.

quantum localized phase described in Sec. 2.2, i.e., when $\alpha \notin \mathbb{Q}$). This behavior is illustrated in Figs. 2.7 – 2.9. Variegated regions of moderate momentum filled with chaotic trajectories are always bounded from both sides by global regular trajectories that span the rest of the phase space.

However, although the existence of the limiting tori guarantees classically bounded trajectories, it is not the only source of localization exhibited by the QRKR, even when coupling is introduced. The QRKR shows localization within both classically regular and classically chaotic regions. Therefore, in general, localization
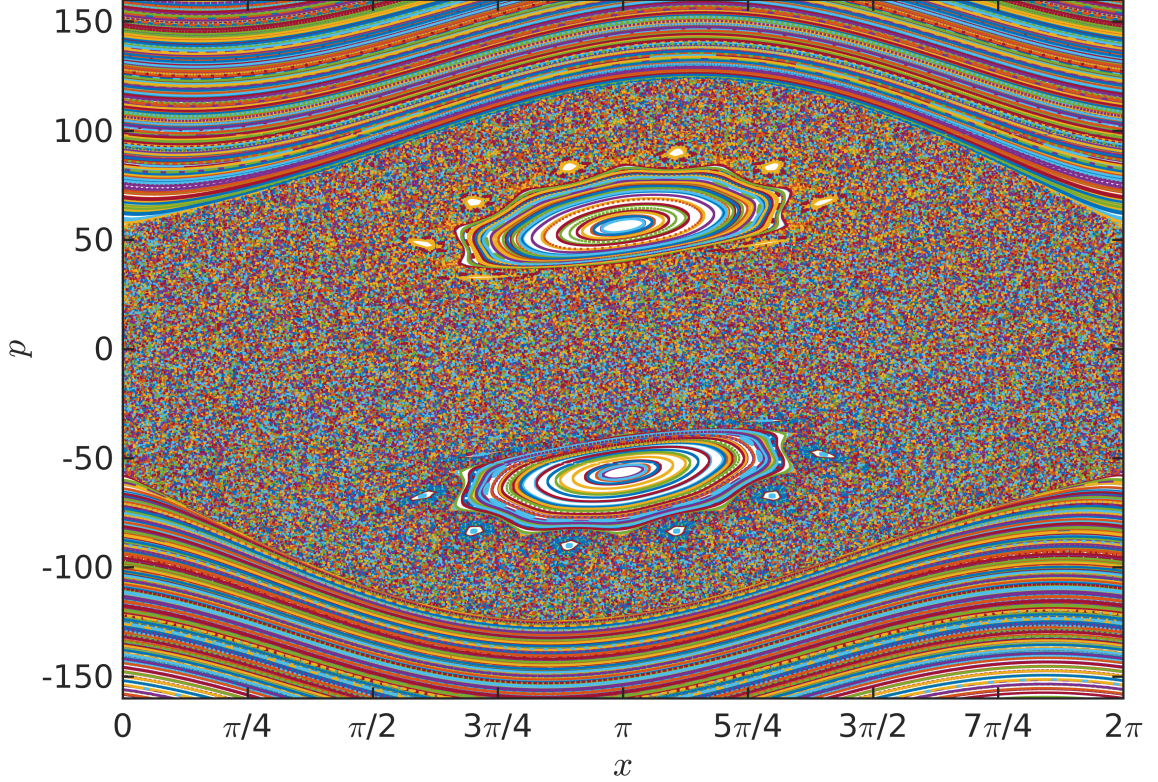
Figure 2.8: Phase map of RKR in a strong kicking regime. Parameters: $C = 20$, $K_{\mathrm{RKR}} = 20$, $q = 1$. At low momenta, chaotic trajectories span most of the phase space. At high momenta, all trajectories are periodic.

is caused by a combination of the classically bounded phase space and quantum Anderson-type localization. The same argument holds for coupled QRKRs. We illustrate it in Sec. 2.5.

2.4 Two and Three Coupled Quantum Relativistic Kicked Rotors

The many-body generalization of the LQKR model was considered in Ref. [104], and it was shown analytically that the many-body LQKR model may exhibit the DMBL phase. In other words, it was shown that localization may survive in the presence of interactions. This finding partially motivated the present study of the few-body generalization of the QRKR model, which is qualitatively distinct from
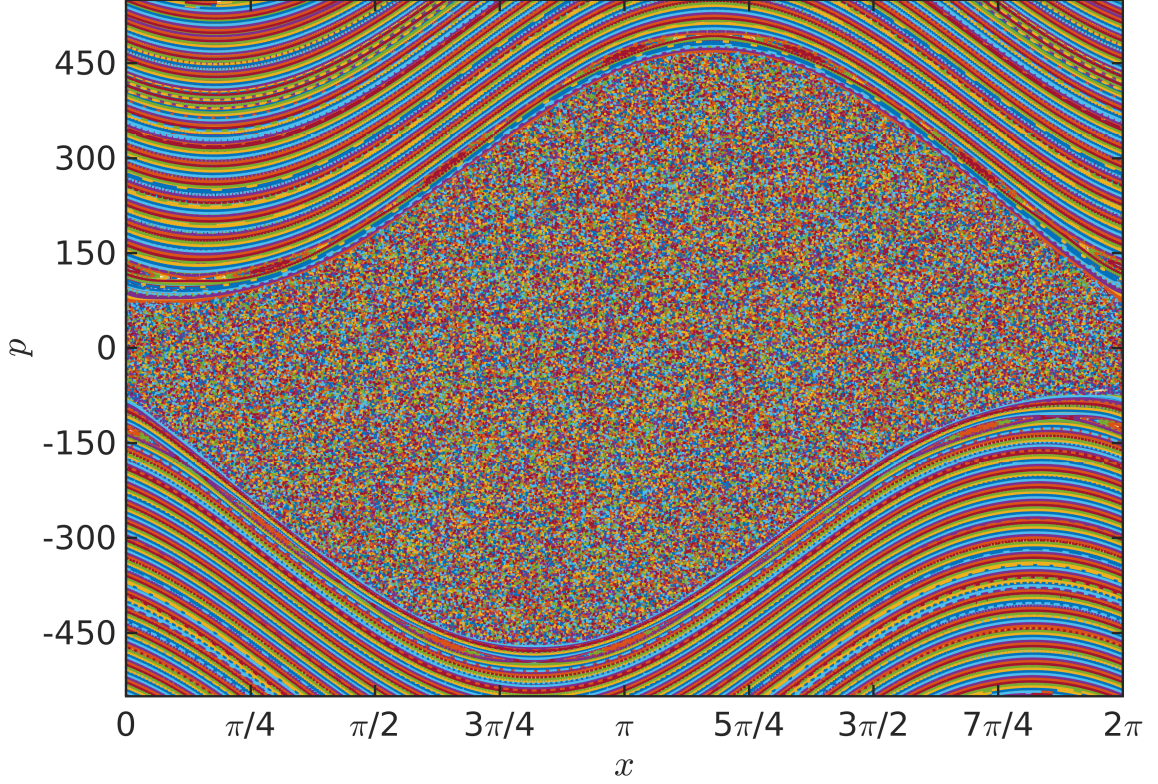
Figure 2.9:   Phase map of RKR in a very strong kicking regime. Parameters: $C = 20$, $K_{\mathrm{RKR}} = 200$, $q = 1$. At low momenta, all trajectories are chaotic. At high momenta, all trajectories are still periodic.

the LQKR model due to the nonintegrability.

In this section, we consider the simplest interacting cases: a two-body and a three-body coupled-QRKR models. Specifically, we consider the models with the Hamiltonian

$$\hat{H}(t) = \hat{H}_0 + (V + H_{\mathrm{int}})\Delta(t), \tag{2.21}$$

where $\hat{H}_0$ is chosen in two different ways. First, for the two-body case, we consider the sum of the Dirac Hamiltonians of the noninteracting QRKRs:

$$\hat{H}_0 = 2\pi\alpha_1 p_1 \hat{\sigma}_1^x + M_1 \hat{\sigma}_1^z + 2\pi\alpha_2 p_2 \hat{\sigma}_2^x + M_2 \hat{\sigma}_2^z. \tag{2.22}$$

Here $\hat{\sigma}_1^{x,z} = \hat{\sigma}^{x,z} \otimes \mathbb{I}$ and $\hat{\sigma}_2^{x,z} = \mathbb{I} \otimes \hat{\sigma}^{x,z}$ are 4×4 matrices, $C_\ell \equiv 2\pi\alpha_\ell$. Second, we use a spinless version of the QRKR to construct

$$\hat{H}_0 = \sum_{\ell=1}^{L} \sqrt{(2\pi\alpha_\ell p_\ell)^2 + M_\ell^2}, \quad L = 2, \ 3. \tag{2.23}$$

As mentioned in Sec. 2.2, it has been shown in Ref. [111] that the spinless model $H'_{\text{QRKR}} = \sqrt{(Cp)^2 + M^2} + K\cos(qx)\Delta(t)$ possesses the same localization properties as the spinful QRKR. For three coupled particles, we only use the spinless $\hat{H}_0$ [Eq. (2.23)] to reduce computational complexity. The kicking potential has a standard form:

$$V(x_1, \ldots, x_L) = \sum_{\ell=1}^{L} K_\ell \cos(qx_\ell), \quad L = 2, \ 3. \tag{2.24}$$

The interaction part is chosen in the same way as for coupled QKRs in Refs. [102, 103], which generalizes the potentials considered in Refs. [52, 95]:

$$H_{\text{int}} = \frac{1}{2} \sum_{j,\ell=1}^{L} K_{j\ell}^{\text{int}} \{\cos(qx_j)\cos(qx_\ell) \ + \cos[q(x_j - x_\ell)]\},$$
$$L = 2, \ 3. \tag{2.25}$$

We study these models numerically, and show that the localized phase is persistent with respect to the interaction in a certain range of parameters.

The Floquet operator

$$\hat{F} = \exp\left[-i\hat{H}_0\right] \exp\left[-i(V + H_{\text{int}})\right]. \tag{2.26}$$

For $\hat{H}_0$ in Eq. (2.22), Ψ is a four-component function. Its four components correspond to the four possible spin configurations of two particles: $\uparrow\uparrow$, $\uparrow\downarrow$, $\downarrow\uparrow$, and $\downarrow\downarrow$, respectively. The free part of the Floquet operator (2.26) in the spinful case is calculated using the properties of the Pauli matrices:

$$
\begin{aligned}
\exp\left[-i\hat{H}_0\right] = \bigotimes_{\ell=1}^{2} \Bigg[&\cos\left(\sqrt{C_\ell^2 p_\ell^2 + M_\ell^2}\right) \mathbb{1} \\
&- i\sin\left(\sqrt{C_\ell^2 p_\ell^2 + M_\ell^2}\right) \frac{C_\ell p_\ell \hat{\sigma}^x + M_\ell \hat{\sigma}^z}{\sqrt{C_\ell^2 p_\ell^2 + M_\ell^2}} \Bigg]
\end{aligned}
\tag{2.27}
$$

and can be efficiently applied numerically to a four-component wave function on a momentum-space grid at each step. Similarly, the kicking and interaction part of the evolution operator (2.26) can be efficiently applied numerically to a wave function on a coordinate-space grid.

We choose an initial wave function in the basis of momentum eigenstates:

$$
\Psi(t=0) = \sum_P a_P(0) \ket{P},
\tag{2.28}
$$

where $P = \{p_1, p_2\}$ or $\{p_1, p_2, p_3\}$ and, to make one step in time, we perform the discrete Fourier transform of $\{a_P\}$ to go to the coordinate representation, where the potential part of the Floquet operator (2.26) is diagonal, and we apply this part to the vector representing the coordinate-space wave function. After that, we perform the inverse Fourier transform to go back to the momentum representation and apply the free part [operator (2.27) for the spinful case] to it. Then this cycle starts over for the next step. This scheme allows us to achieve efficient numerical evolution

34

that only requires application of diagonal operators and a fast Fourier transform.

2.5   Numerical experiments with two and three coupled QRKRs

In Figs. 2.10 – 2.12, we present time dependence of the average mean-squared momentum per particle for two coupled spinful QRKR particles: $\langle p_1^2 + p_2^2 \rangle / 2$. In Ref. [104], this quantity was shown to be a reliable indicator of dynamical localization (as opposed to the average energy). Different values of the parameters determine various regimes that are exhibited by our model. We start in a Gaussian-shaped initial state in the momentum space centered around the point $\left(p_1^{(0)}, p_2^{(0)} \right) = (0,0)$ with both spins up:

$$\Psi(p_1, p_2, t = 0) \sim \exp\left[-\frac{p_1^2}{2\Delta_1^2} - \frac{p_2^2}{2\Delta_2^2} \right] |\uparrow\uparrow\rangle , \qquad (2.29)$$

and widths $\Delta_1 = \Delta_2 = 4$. Therefore, the initial value of the average mean-squared momentum per particle is $\langle p_1^2 + p_2^2 \rangle / 2 = 8$. Figures 2.10 and 2.11 represent the dynamically localized state. It is characterized by nonresonant values of the velocities $(\alpha_1 \neq \alpha_2 \notin \mathbb{Q})$. Saturation of the average mean-squared momentum per particle is verified by linear fits that have zero slope up to a fitting error; the corresponding equations are shown inside the plots. The insets in these figures show the probability density at the final time $|\Psi(p_1, p_2, t = N)|^2$ as a function of each of the momenta while integrated over the other one. As one can see from these insets, in the regime of localization, the wave functions decay exponentially with momenta and, in the vicinity of numerical boundaries, reach the values below 10^{-27}. This ensures that

35
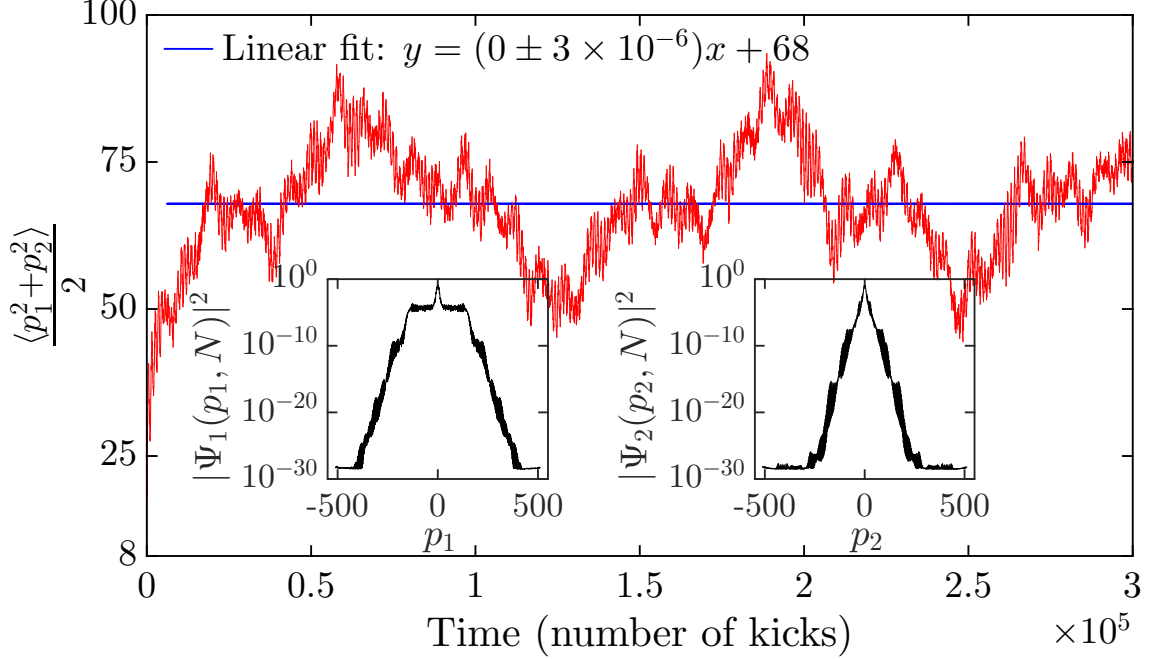
Figure 2.10: Average mean-squared momentum per particle in the localized regime. Oscillating red line shows the calculation result. Straight blue line is a linear fit that shows no slope up to a fitting error (equation is given inside the plot). Parameters: $\alpha_1 = 1/3 + 0.02/2\pi, \alpha_2 = 1/3 - 0.03/2\pi$, $q = 3$, $K_1 = K_2 = 0.8$, $K_{12}^{\text{int}} = 0.04$, $M_1 = M_2 = 12$ ($\hbar_{\text{eff}_1} \approx \hbar_{\text{eff}_2} \approx 0.37$). Insets: Probability density at the final time $t = N = 3 \times 10^5$ kicks as a function of each momentum while integrated over the other one.

during the evolution, the population does not come close to the numerical boundaries, and there is no unphysical reflection from them. Stable exponential decay of a wave function with a constant bound on its width indicates localization. In Fig. 2.10, we take parameters similar to those used in Ref. [111] for the single QRKR and add 5% of interaction, i.e., $K_{12}^{\text{int}} = 0.05K_{1,2}$. These parameters correspond to $\hbar_{\text{eff}_1} \approx \hbar_{\text{eff}_2} \approx 0.37$. In Fig. 2.11, we set $\hbar_{\text{eff}_1} = \hbar_{\text{eff}_2} = 1$ and periodicity parameter $q = 1$ and obtain more stable localization. Other parameters in this case are such that in the corresponding RKR model, many tori are destroyed giving way to a broad chaotic region. In particular, the kicking strength constant exceeds the first (and, in this case, the only) critical constant—$\hbar_{\text{eff}}K_{1,2} > K_{\text{RKR}}^{1,\text{cr}} \approx 2$—corresponding to

36
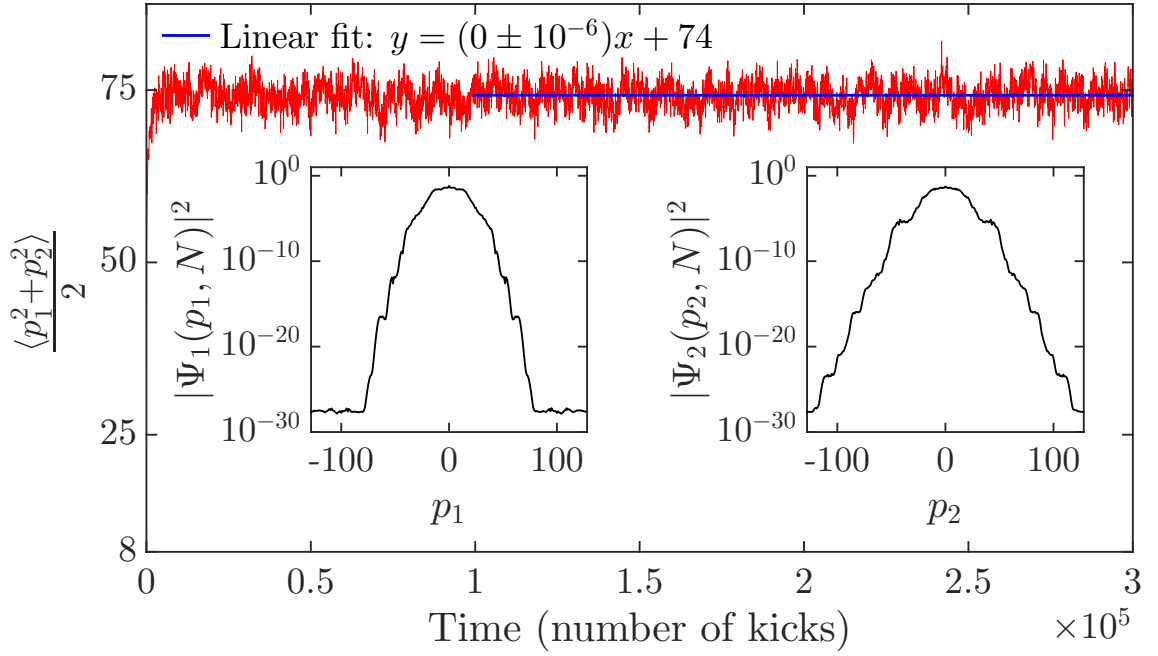
Figure 2.11: Average mean-squared momentum per particle in the localized regime. Oscillating red line shows the calculation result. Straight blue line is a linear fit that shows no slope up to a fitting error (equation is given inside the plot). Parameters: $\hbar_{\text{eff}} = 1, \alpha_1 = 1.6 + 0.1/2\pi,\ \alpha_2 = 1.6 - 0.15/2\pi,\ q = 1,\ K_{1,2} = 4/\hbar_{\text{eff}},\ K_{12}^{\text{int}} = 0.2/\hbar_{\text{eff}},$ $M_{1,2} = (2\pi\alpha_{1,2})^2 / \hbar_{\text{eff}}$. Insets: Probability density at the final time $t = N = 3 \times 10^5$ kicks as a function of each momentum while integrated over the other one.
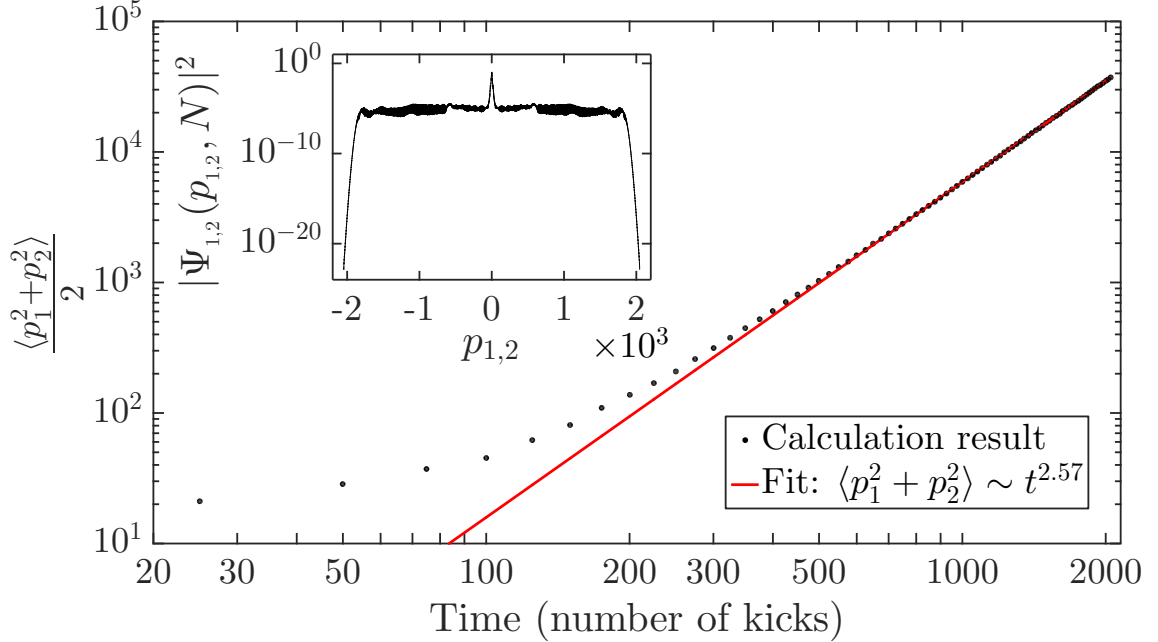
Figure 2.12: Average mean-squared momentum per particle in the superballistic regime. Black points show the calculation result. Red line is a power fit. Parameters: $\alpha_{1,2} = 1/3 - 0.03/2\pi$, $q = 3$, $K_{1,2} = 0.7$, $K_{12}^{\text{int}} = 0.2$, $M_{1,2} = 12$. Inset: Probability density at the final time $t = 2 \times 10^3$ kicks as a function of each momentum while integrated over the other one.

the single RKR. Figure 2.12 shows the delocalized phase described by the resonant values of the velocities: $\alpha_1 = \alpha_2$. Even though $\alpha_1, \alpha_2 \notin \mathbb{Q}$—so that for single QRKR, such α guarantees localization—according to Ref. [104], in the many-body LQKR model, equal values of the velocities correspond to additional resonances due to the interaction that lead to divergence of the emergent momenta-containing integrals of motion (IOMs) present in the many-body LQKR model [104]. In the many-body QRKR model at large momenta, these IOMs become approximate. Nevertheless, their divergence results in the divergence of the associated momenta, which is confirmed by our numerical results. In particular, in Fig. 2.12 we see a rapid transport in the momentum space that causes the fast growth of the probability density near the numerical boundaries of the momentum grid. Unfortunately, this complication

makes further numerical analysis at large time scales inefficient. However, we can clearly see the signs of superballistic transport in this plot. In particular, in this example, $\langle p_1^2 + p_2^2 \rangle \sim t^{2.57}$ until the wave function reaches the grid boundaries at the time beyond $t = 2000$ kicks, and we can not rely on the numerics after that point. The inset shows the probability density at final time $|\Psi(p_1, p_2, t = N)|^2$ as a function of each of the momenta while integrated over the other one (p_1 and p_2 dependencies are the same in this case due to symmetry).

In Fig. 2.13, we compare localization in two-particle and three-particle spinless QRKR models at the same respective parameters. The plots are given in the lin-log scale to show details of saturation. We should note that upon increasing the interaction strengths, there appear regimes of long-lasting logarithmic growth of the average mean-squared momentum per particle that may be generic for coupled nonintegrable dynamical systems but also satisfy the condition $\nu = 0$ in Eq. (2.4). As one can see, in Fig. 2.13, panel (a), the localization length and time it takes the mean-squared momentum to saturate increase with the number of particles, as expected given the increased contribution of interactions. However, this panel shows saturation well below the integrable region determined by $p_\ell^2 \gg (M_\ell / C_\ell)^2 = (C_\ell / h_{\text{eff}\ell})^2 \approx 100$. In contrast to it, in panel (b), the near-integrability threshold is $p_\ell^2 \gg 1$, and the saturated value satisfies this condition to some extent. Notice that in this case, the saturated values of mean-squared momentum per particle are in the same range for two and three particles.
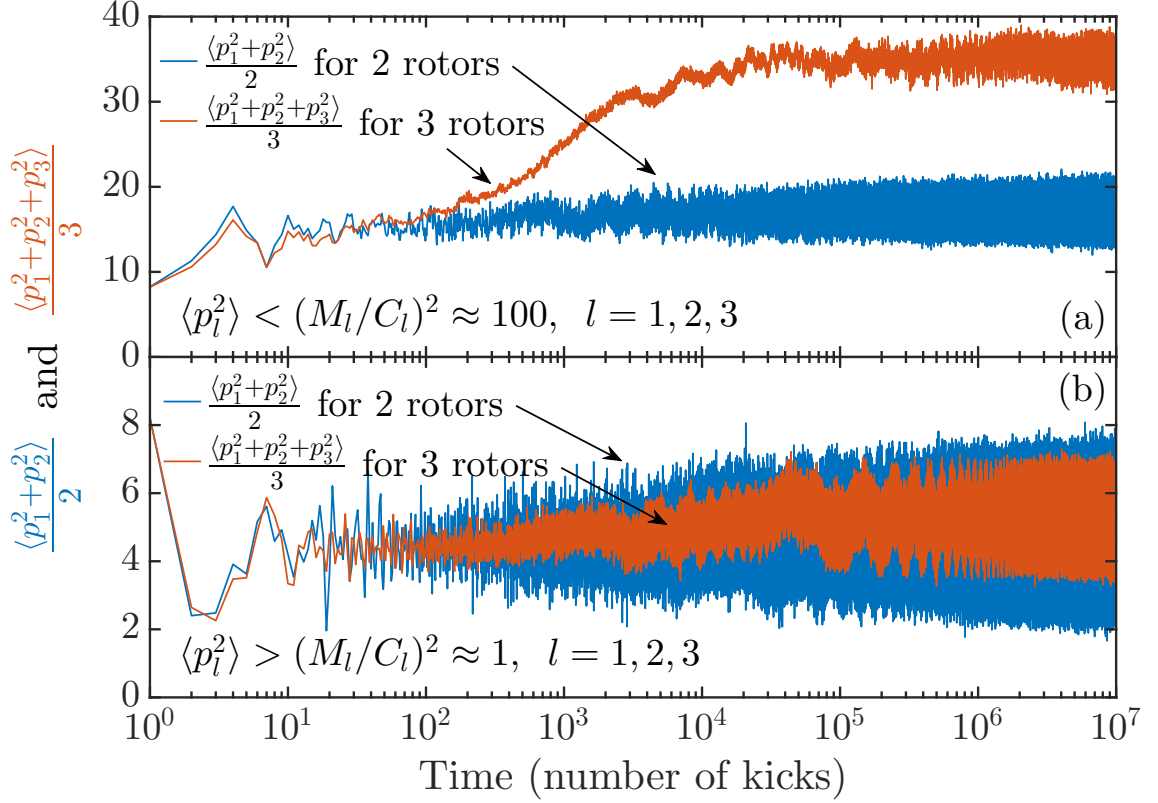
Figure 2.13: Average momentum variance per particle in the localized regime for two (blue lines) and three (red lines) coupled spinless QRKRs. Panel (a) shows localization far from integrable limit; parameters are $\hbar_{\text{eff}} = 1$, $\alpha_1 = 1.6 + 0.1/2\pi$, $\alpha_2 = 1.6 - 0.15/2\pi$, $(\alpha_3 = 1.6 + 0.225/2\pi)$, $q = 1$, $K_1 = 2/\hbar_{\text{eff}}$, $K_2 = 3/\hbar_{\text{eff}}$, $(K_3 = 1.5/\hbar_{\text{eff}})$, $K_{12}^{\text{int}} = 0.1/\hbar_{\text{eff}}$, $(K_{23}^{\text{int}} = 0.07/\hbar_{\text{eff}}$, $K_{31}^{\text{int}} = 0.13/\hbar_{\text{eff}})$, $M_{1,2,(3)} = \left(2\pi\alpha_{1,2,(3)}\right)^2/\hbar_{\text{eff}}$. Panel (b) shows localization close to the integrable limit. Parameters are the same as in panel (a) except for $\alpha_{1,2,(3)}$ being multiplied by a factor 0.1.

2.6 Experimental Proposal

Due to the structure of the Floquet operators (2.16) and (2.26) for single and coupled QRKRs respectively, as well as for any kicked Hamiltonian, quantum dynamics is almost invariant with respect to swapping the free and the kicked parts; i.e., the Hamiltonians

$$\mathcal{H} = H_0 + H_1\Delta(t) \tag{2.30}$$

and

$$\mathcal{H}_{\text{swap}} = H_0 \Delta(t) + H_1 \tag{2.31}$$

generate the same Floquet evolution. More precisely, in order to get completely the same dynamics, when swapping, one should also change from considering evolution between the moments of time right after the kicks to those just before the kicks and vice versa.

In particular, the single QRKR is equivalent to a model with the Hamiltonian

$$\hat{H}_{\text{swap}}^{\text{QRKR}} = \left(2\pi\alpha p\hat{\sigma}^x + M\hat{\sigma}^z\right)\Delta(t) + K\cos(qx). \tag{2.32}$$

Let us put $q = 1$. Recall that the angular coordinate $x \in [0, 2\pi)$ and the dimensionless angular momentum is quantized—$p \in \mathbb{Z}$. Then one can establish a correspondence between the QRKR and a spin-$\frac{1}{2}$ particle hopping on a 1D lattice subject to a pulsed magnetic field. This correspondence is summarized in the following table.

QRKR	x	p	$2\pi\alpha$	M	K
Spin-$\frac{1}{2}$	$ka + \pi$	j	$-\dfrac{\mu T}{2\hbar}B_x(1)$	$-\dfrac{\mu T}{2\hbar}B_z$	$T\dfrac{\mathcal{T}}{\hbar}$

Here k is a quasi-momentum in the first Brillouin zone for a lattice with real-space site numbers j and a lattice constant a. μ is a magnetic moment associated with a particle's spin, $B_x(1)$ is an x component of the magnetic field on the site $j = 1$ [so that in general, $B_x(j) = jB_x(1)$ is linear in real space], B_z is a uniform z component of the magnetic field, and $\mathcal{T}$ is a hopping energy. So, we get the following 1D single-band tight-binding Hamiltonian for a spin-$\frac{1}{2}$ particle that is being periodically kicked

via the external magnetic field:

$$H_{\text{magn}} = -\mu \left[B_x(j)s_x + B_z s_z \right] \Delta(t) - \mathcal{T} \cos(ka), \qquad (2.33)$$

where s_x and s_z are the particle's spin components.

If we keep the kicking function $\Delta(t)$ at the original place—as in Eq. (2.30)—we get a Hamiltonian for a spin-$\frac{1}{2}$ particle in a time-independent magnetic field and in a pulsed optical lattice:

$$H_{\text{pl}} = -\mu \left[B_x(j)s_x + B_z s_z \right] - \mathcal{T} \cos(ka)\Delta(t). \qquad (2.34)$$

In this case, however, it is important to keep the lattice on so as not to recover the quadratic kinetic energy term. It can be done by switching from the deep optical lattice to the shallow one back and forth instead of turning it on and off completely.

Another possible setup for implementing the QRKR model is a two-level atom in a laser field with detuning δ and nonuniform Rabi frequency $\Omega(j)$ at the jth site in the presence of a pulsed optical lattice. It is implemented via the following mapping.

QRKR	x	p	$2\pi\alpha$	M	K
Atom	$ka + \pi$	j	$T\Omega(1)$	$-T\dfrac{\delta}{2}$	$T\dfrac{\mathcal{T}}{\hbar}$

Then in the rotating wave approximation,

$$H_{\text{at}} = \hbar\Omega(j)\left(|g\rangle\langle e| + |e\rangle\langle g|\right) - \hbar\frac{\delta}{2}\left(|e\rangle\langle e| - |g\rangle\langle g|\right)$$
$$- \mathcal{T}\cos(ka)\Delta(t), \tag{2.35}$$

where $|g\rangle$ and $|e\rangle$ are the ground and excited states of the atom in the rotating frame. The same caveat regarding the quadratic kinetic term as in the previous setting applies here. As well as in the previous examples, one could kick the first part of this Hamiltonian instead of applying a pulsed lattice.

Similar models can be constructed on the basis of the QKR and LQKR models. In particular,

$$H_{\text{swap}}^{\text{QKR}} = \frac{\hbar_{\text{eff}}p^2}{2}\Delta(t) + K\cos(x) \tag{2.36}$$

and

$$H_{\text{swap}}^{\text{LQKR}} = 2\pi\alpha p\Delta(t) + K\cos(x) \tag{2.37}$$

correspond to a charged particle in a 1D lattice in the presence of a kicked electric field. This field is linear in space for $H_{\text{swap}}^{\text{QKR}}$ and uniform for $H_{\text{swap}}^{\text{LQKR}}$.

Extensions of the single-particle models (2.32) – (2.37) to the case of many interacting particles can be mapped to corresponding many-body QRKRs, QKRs, or LQKRs in the same way.

Hamiltonians (2.32) – (2.37) might be realized in cold atoms in optical lattices. Interestingly, according to the mapping $p \mapsto j$, for such systems, dynamical localization as well as other intriguing transport regimes such as superballistic trans-

port, take place in real space rather than in momentum space, which makes these phenomena especially demonstrative in experiment.

2.7   Conclusion

Starting with the single-particle QRKR model that possesses the rich variety of transport phases, we introduced its peculiar spin dynamics phenomenology and generalized it to the model of interacting QRKRs. For the models of two and three coupled QRKRs, we showed that the transport regimes—and, in particular, the localized phase—can survive interactions. We are not aware of any previous study of coupled QRKRs, but we point out that for the well-studied coupled QKRs and related static lattice models, most works predict delocalization at least for infinite-range interaction. Our calculations indicate the existence of the localized regimes for such a coupling of two and three QRKRs.

Unfortunately, exact numerical study of the many-body QRKR model is not feasible presently. However, at high momenta, it can be approximated by the integrable many-body LQKR model, and this approximation works only better as the system goes to higher momentum states. In Ref. [104], the many-body LQKR model was analytically shown to exhibit the DMBL phase. Besides that, as opposed to the case of QKR, the classical model behind QRKR is not chaotic at high momenta. As we have shown, in the cases of two and three coupled QRKRs, localization has a quantum origin and does not rely on the existence of KAM tori in the phase space of the corresponding classical problem. However, for a large number of interacting

rotors, if this localization happens to deteriorate completely, and the growth of the particles' momenta recovers, at high enough momenta the system will enter the integrable regime and get localized. This is our main argument in favor of DMBL in the nonintegrable system of the many-body QRKR model. In general, the observable dynamical localization can represent a nontrivial interplay of both effects that may be difficult to disentangle. In summary, our argument supplemented by few-body calculations provide a strong hint that the nonintegrable many-body QRKR model should exhibit dynamically localized many-body states.

In addition, we propose a class of kicked lattice models that map onto various kicked-rotor models and can be realized in the framework of cold atoms in optical lattices. This realization might allow one to study dynamical localization including DMBL, and other anomalous transport phenomena exhibited by the QRKR and its many-body versions in experiment.

Chapter 3: Many-Body Dynamical Localization in a Kicked Lieb-Liniger Gas

3.1 Introduction

Everyday experience tells us that injecting energy into a closed system causes it to heat up. It follows therefore that doing this repeatedly will cause the system to heat to infinite temperature. Remarkably this intuition does not necessarily carry over to quantum systems. Recently there has been a large amount of work concerning the prevention of runaway heating in periodically driven closed quantum systems with much of the focus centered on achieving this via the addition of disorder to the system [45, 123, 124, 125]. A far simpler and more intriguing example is provided by the quantum kicked rotor, as discussed in detail in Chapter 2. In this elementary quantum system a single particle is subjected to a periodic, instantaneous kicking potential, but otherwise propagates freely. After an initial period of increase the energy is seen to saturate, no more energy from the kick can be absorbed, and heating is stopped. This behavior stands in contrast to the corresponding classical system, in which the energy grows without bound, linearly in time. As Chapter 2 explains, it was first discovered numerically [5, 49, 50], and later the energy saturation was eluci-

dated by the construction of a mapping between the angular-momentum dynamics of the quantum kicked rotor and the dynamics in a lattice model with quasi-disordered potential similar to the Anderson model [11]. This mapping shows that the wavefunction becomes exponentially localized in angular-momentum space and leads to this phenomenon being dubbed dynamical localization [12, 15]. Subsequently, dynamical localization was observed in clouds of dilute ultra-cold atoms [51, 126, 127].

A natural question to ask is whether dynamical localization can survive in the presence of interactions. This has been investigated in several studies where interactions have been introduced through a more complicated kick which couples the particles (see Chapter 2 and Refs. [128, 129]) or by including interparticle interactions between the kicks [52, 53, 64, 65, 80, 81, 87, 99, 104, 130, 131]. These latter scenarios are of particular interest as interparticle interactions can be readily tuned in ultracold-atom experiments [132]. Using mean-field theory it was shown that after some long time, which is non-linear in the interaction strength, the kinetic energy of the system grows in a sub-diffusive manner, and localization is destroyed [80, 87]. Degradation of localization in the presence of interactions has also been shown experimentally in a system of two coupled rotors [94]. A lack or delay in heating is also witnessed in other driven interacting quantum systems [133, 134, 135, 136].

In one dimension perturbative techniques such as mean-field theory break down. Any would-be order, i.e a mean field is destroyed by the strong fluctuations caused by the reduced dimensionality. Systems are strongly correlated as a matter of course, excitations are collective and often cannot be adiabatically connected to the those of free models [137, 138]. The description of a kicked interacting Bose gas using

mean-field theory is no longer appropriate. Fortunately there exists an array of non-perturbative methods which can be applied to the problem in one dimension. Here we investigate many-body dynamical localization in an interacting one-dimensional system using a variety of non-perturbative techniques: Fermi-Bose mapping, linear and non-linear Luttinger-Liquid theory, and generalized hydrodynamics [139, 140]. We provide evidence that in the presence of interactions one-dimensional systems can dynamically localize at least for a very long time, which is many orders of magnitude longer than the time scales currently reachable in experiments. This dynamical localization occurs in the space of many-body eigenstates which results in a saturation of the energy and the width of the exponentially decaying quasi-particle occupation function after a finite number of kicks.

3.2   Model

The system we study consists of an interacting 1D Bose gas which is subjected to a periodic kicking potential. The Hamiltonian which describes this model is a natural extension of the standard single-particle system to the many-body case:

$$H = H_{\mathrm{LL}} + \sum_{j=-\infty}^{\infty} \delta(t - jT)H_{\mathrm{K}}. \tag{3.1}$$

The first term is the Lieb-Liniger Hamiltonian [141, 142] which provides an excellent description of a 1D cold-atom gas [143, 144],

$$H_{LL} = -\frac{1}{2m} \sum_{i=1}^{\mathcal{N}} \frac{\partial^2}{\partial x_i^2} + 2c \sum_{\langle i,j \rangle} \delta(x_i - x_j), \tag{3.2}$$

where $\mathcal{N}$ is the number of particles, $\sum_{\langle i,j \rangle}$ denotes summation over pairs, m is the mass of the particles, c is the interaction strength, and we have set $\hbar = 1$. In the second-quantized form,

$$H_{\mathrm{LL}} = \int \mathrm{d}x\, b^{\dagger}(x) \left[-\frac{\partial_x^2}{2m} \right] b(x) + c\, b^{\dagger}(x)b(x)b^{\dagger}(x)b(x). \tag{3.3}$$

Here $b^{\dagger}(x)$ and $b(x)$ are creation and annihilation operators, $[b(x), b^{\dagger}(y)] = \delta(x - y)$, describing bosons of mass m which interact with point-like density-density interaction of strength $c \geq 0$. The model is integrable and its equilibrium and out-of-equilibrium properties have been extensively studied [145, 146, 147, 148, 149]. The eigenstates can be constructed exactly using Bethe Ansatz and are characterized by a set of single-particle momenta, k_j, $j = 1, \ldots \mathcal{N}$. The same states are also the eigenstates of an infinite set of non-trivial conserved operators Q_n ($Q_2 \propto H_{\mathrm{LL}}$) such that $Q_n |\{k_j\}\rangle = \sum_{j=1}^{\mathcal{N}} k_j^n |\{k_j\}\rangle$. This constrains the dynamics of the system. The second term in Eq. (3.1) describes the kick which couples to the boson density:

$$H_{\mathrm{K}} = \int \mathrm{d}x\, V \cos{(qx)} b^{\dagger}(x)b(x), \tag{3.4}$$

where V is the kicking strength, T is the kicking period, and q is the wave-vector of the kicking potential. A potential of this form is achieved experimentally by means of a Bragg pulse. Note that while the unperturbed H_{LL} in Eq. (3.3) is integrable, the kicking breaks the integrability, and H in Eq. (3.1) is not integrable.

The kicked system follows a two-step time evolution which separates into evolution between the kicks via $e^{-iH_{\mathrm{LL}}T}$ and over the kicks via $e^{-iH_{\mathrm{K}}}$. This can be expressed in terms of a single operator H_{F} known as the Floquet Hamiltonian, governing evolution over one period: $e^{-iH_{\mathrm{F}}} = e^{-iH_{\mathrm{LL}}T}e^{-iH_{\mathrm{K}}}$. Our goal is to determine the energy of the system after N kicks,

$$E(t) = \langle \Psi_0 | \, e^{iH_{\mathrm{F}}N} H_{\mathrm{LL}} e^{-iH_{\mathrm{F}}N} \, |\Psi_0\rangle \,, \tag{3.5}$$

where $t = NT$, for some initial state $|\Psi_0\rangle$. Throughout the chapter, we assume that the system is initialized in its ground state.

3.3 Tonks-Girardeau limit

Aside from the trivial $c = 0$ limit which recovers the single-particle model, one can examine the opposite case of $c \to \infty$ known as the the Tonks-Girardeau (TG) gas [150, 151]. Through Fermi-Bose mapping the wave-functions of the TG gas take the form of a Slater determinant. This mapping remains valid even in the presence of time-dependent one-body potentials [152, 153]. As a result, we may write the

solution of the time-dependent Schrödinger equation as

$$|\Psi_0(t)\rangle = \int \mathrm{d}^{\mathcal{N}}x \, \mathcal{A} \det\left[\phi_n(x_i, t)\right] \prod_{j=1}^{\mathcal{N}} b^\dagger(x_j) |0\rangle, \tag{3.6}$$

where $\mathcal{A} = \prod_{1 \leq i < j \leq \mathcal{N}} \mathrm{sgn}(x_i - x_j)$ is an anti-symmetriser which makes sure the wave-function remains symmetric, and $\phi_n(x_i, t)$ are a set of orthogonal solutions of the single-particle Schrödinger equation:

$$i\partial_t \phi_n(x, t) = \left[-\frac{\partial_x^2}{2m} + \sum_{j=-\infty}^{\infty} \delta(t - jT) V \cos(qx) \right] \phi_n(x, t). \tag{3.7}$$

The energy of this state is given by the sum of the single-particle energies:

$$E(t) = \sum_{n=1}^{\mathcal{N}} \int \phi_n^*(x, NT) \left[-\frac{\partial_x^2}{2m} \right] \phi_n(x, NT). \tag{3.8}$$

Since each of the single-particle wave-functions exhibits dynamical localization with the energy remaining bounded, the total energy of the TG gas will be bounded as well. This proves dynamical localization in the limiting case of an infinitely strongly repulsive Bose gas.

If the system is initially in the ground state all single-particle momentum states are filled between the Fermi points $|k_j| \leq k_F$, and kicking causes particles to change their momenta by multiples of q. Therefore if $q \geq k_F$, particles cannot avoid changing their momenta as a result of the kick. On the other hand if $q = 2\pi/L$ then Pauli blocking will come into play and inhibit the hopping of particles in momentum space. Thus by changing between small and large values of q we can tune between

many-body and single-particle physics. Moreover, for any $c \neq 0$, eigenstates of H_{LL} obey the Pauli exclusion principle, i.e. $k_i \neq k_j, \forall i \neq j$ [154], so we expect small q to be the most interesting from the perspective of many-body physics.

3.4   General case

Having established localization at both ends of the range of values for the coupling constant, we turn to a discussion of the system under general conditions, for arbitrary c.

The low-energy behavior of many one-dimensional systems, including the Lieb-Liniger model, is described by the Luttinger-liquid theory [155]. A purely analytic approach to the kicked Lieb-Liniger model in this framework is given in Ref. [156]. One more step further is made there, as well, and the non-linear Luttinger liquid analysis is applied to capture the dominant contribution of the band curvature. The result in both cases is that as long as the system stays at low energy – within the validity of the approximation – the energy is going to be bounded, just as in the single-particle case. This statement is self-consistent as long as the kicking is not too strong, so that the energy oscillations do not take the system outside of the low-energy regime.

In order to study the behavior of the system beyond the region of applicability of the analytics, we investigate the kicked Lieb-Liniger gas numerically, doing so by making use of the integrability of H_{LL}. The spectrum of the Lieb-Liniger model, as in many other integrable models, consists of long-lived quasi-particles. In the

thermodynamic limit and if the variation of the particle density is slow, the system is completely described by the local occupation function of these quasi-particles, $n(x, \lambda, t)$. Here x is the position in space and λ is the quasi-particle momentum. Generalized hydrodynamics (GHD) is a recently developed theory which describes the evolution of $n(x, \lambda, t)$ at large length scales [139, 140]. Between the kicks the evolution of the gas is determined by the GHD equation:

$$\{\partial_t + v_{\text{eff}}\,[n]\,\partial_x\}\,n(x, \lambda, t) = 0, \tag{3.9}$$

where $v_{\text{eff}}[n](x, \lambda, t)$ is the effective velocity of the quasi-particle excitations of the model which depends upon n itself. We will use the following definition of a dressed function. The dressed function $f^{\text{dr}}(\lambda)$ is defined with respect to a bare function $f(\lambda)$ as a solution of the equation:

$$f^{\text{dr}}(\lambda) = f(\lambda) + \int \frac{d\mu}{2\pi}\varphi(\lambda - \mu)n(x, \mu, t)f^{\text{dr}}(\mu), \tag{3.10}$$

where $\varphi(x) = 2c/(c^2 + x^2)$. In these notations the effective velocity is given by:

$$v_{\text{eff}}(\lambda) = \frac{[\varepsilon'(\lambda)]^{\text{dr}}}{[p'(\lambda)]^{\text{dr}}}, \tag{3.11}$$

where $\varepsilon(\lambda) = \lambda^2/2m$ and $p(\lambda) = \lambda$ are the bare energy and momentum of the quasi-particles, and the prime indicates the derivative with respect to λ. In both the TG and non-interacting limits, this equation becomes exact [157], and $n(x, \lambda, t)$ reduces to the Wigner function [158].

To determine the full evolution, we need to compute the effect of the kicks on $n(x, \lambda, t)$. In full generality this is a difficult task which requires the explicit knowledge of the matrix elements of e^{-iH_K} with arbitrary eigenstates of the Lieb-Liniger model. For slowly varying potential, however, which is an applicability condition of GHD, the situation simplifies. In this case the kicking term couples to the quasi-particles in the same way as to the bare particles described by $b^\dagger(x), b(x)$ [159]. Hence, as explained in detail in Sec. 3.5.1, over a kick at time t we have:

$$\tilde{n}(x, z, t^+) = e^{2iV\sin(\frac{qz}{2})\sin(qx)}\tilde{n}(x, z, t^-), \tag{3.12}$$

where $\tilde{n}(x, z, t)$ is the Fourier transform of $n(x, \lambda, t)$ with respect to λ.

Using Eqs. (3.9) and (3.12), we can determine the total quasi-particle occupation function,

$$n(\lambda, t) = \int dx\, n(x, \lambda, t) , \tag{3.13}$$

and the total energy of the gas:

$$E(t) = \int \frac{d\lambda}{2\pi}\, \varepsilon^{dr}(\lambda)n(\lambda, t) . \tag{3.14}$$

We also introduce the common measure of localization, the variance of the occupation function, $\text{var}[n(\lambda, t)]$ (see, e.g., Refs. [13, 14, 108, 109, 160, 161]), where for convenience, we include additional factors into the conventional definition:

$$\text{var}[f(\zeta, t)] = \int \frac{d\zeta}{2\pi} \frac{\zeta^2}{2m} f(\zeta, t) . \tag{3.15}$$

Saturation of the variance indicates exponential localization in the λ space. All the quantities in our calculations are dimensionless and sometimes implicitly expressed in units of m, $L/2\pi$, and T. The evolution between the kicks can be evaluated via a finite-difference scheme [162]:

$$n(x, \lambda, t + \delta t) = n(x - v_{\text{eff}}[n(x, \lambda, t)]\delta t, \lambda, t) , \tag{3.16}$$

where we choose $T/\delta t = 1000$. At each time step v_{eff} is reevaluated via Eq. (3.11), and the shift is performed in the Fourier space by explicitly calculating the integral:

$$n(x, \lambda, t + \delta t) = \int dp e^{ip\{x - v_{\text{eff}}[n(x,\lambda,t)]\delta t\}} \bar{n}(p, \lambda, t) , \tag{3.17}$$

where $\bar{n}(p, \lambda, t)$ is the Fourier transform of $n(x, \lambda, t)$ with respect to x. This scheme works well at short times, but due to its very high numerical complexity, for practical purposes we employ a different approach – a linearized approximation to Eq. (3.9) [163]. In this approximation we calculate $v_{\text{eff}}[\langle n \rangle]$ after a kick using a spatially averaged $\langle n(\lambda, t) \rangle = \int dx n(x, \lambda, t)/L$ which then allows to propagate the solution over the entire duration of the free evolution at once. This is easily carried out in Fourier space via:

$$\bar{n}(p, \lambda, t + T) = e^{-ip v_{\text{eff}}[\langle n \rangle]T} \bar{n}(p, \lambda, t) . \tag{3.18}$$

The next kick is then applied via Eq. (3.12), $v_{\text{eff}}[\langle n \rangle]$ is determined anew, and the process is repeated. This approximation becomes exact in the TG case and agrees

well with the finite difference scheme at short times. We demonstrate the validity of this approximation in Sec. 3.5.3.

We choose a small value of the kicking-potential wave-vector $q = 4\pi/L$ and take $V = 0.5$. In this case, the corresponding single-particle classical system is in the regime of global chaos, although the phase-space is mixed with island of stability present. The critical value of the kicking strength where the regular-to-chaotic transition occurs is $(qL/2\pi)^2 V_{\text{cr}} = 4V_{\text{cr}} \approx 0.97$ with the remaining KAM islands vanishing to the naked eye towards $(qL/2\pi)^2 V = 4V = 5$ [8] (See Sec. 3.5.2 for details). As shown in Ref. [156], interactions cause the effective kicking strength to be larger and the analogous critical value to be, in fact, even lower than the single-particle one.

Fig. 3.1 shows the momentum variance of the Lieb-Liniger gas under kicking for $\gamma = \mathcal{N}/(mcL) = 10$. At short times, the energy grows quickly, but later, it saturates and becomes bounded due to dynamical localization. At the same time, $n(\lambda, t)$, which is initially the Fermi-Dirac Π-shaped function with the Fermi momentum $\lambda_F = 100$ – with our choice of $\mathcal{N} = 200$, – acquires exponential tails (see Fig. 3.2) and stops spreading any further after the saturation of energy is reached. Fig. 3.2 also shows the Fourier transform of the spatial density $\bar{n}(p, t = 1.5 \times 10^5) = \int \frac{d\lambda}{2\pi} \bar{n}(p, \lambda, t = 1.5 \times 10^5)$ that decays exponentially, as well, but its variance (width) keeps growing with time, as opposed to that of $n(\lambda, t)$ – see Fig. 3.1. We were unable to reach its saturation at these parameters, so its continued growth eventually leads to a breakdown of the numerical method and the applicability of GHD. Prior to this, however, no delocalization is seen for a very long time. At low enough kicking
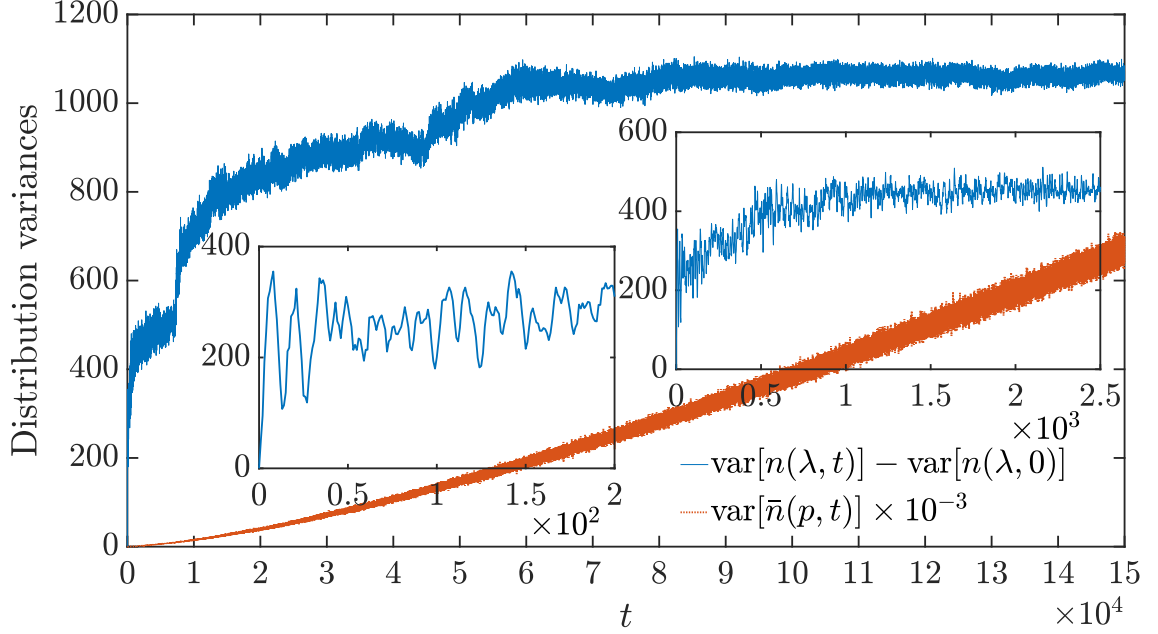
Figure 3.1: Main plot. Upper solid blue curve: variance of the momentum density $n(\lambda, t)$ in the kicked Lieb-Liniger gas as a function of time relative to the initial variance: $\mathrm{var}[n(\lambda, t)] - \mathrm{var}[n(\lambda, 0)]$ [see Eq. (3.15)]. It saturates with time, signaling at least transient dynamical localization in sharp contrast to the classical diffusion (heating) under kicking. Lower dotted red curve: scaled variance of $\bar{n}(p, t)$. We were unable to reach its saturation at these parameters, so its continued growth eventually leads to the breakdown of GHD and our scheme and might also signal the potential for eventual delocalization, which we, however, do not observe for a very long time. Insets: the same data for $\mathrm{var}[n(\lambda, t)] - \mathrm{var}[n(\lambda, 0)]$ as a function of time at shorter time scales, which are more relevant to experiments. Parameters: $V = 0.5$, $q = 4\pi/L$, $\gamma = 10$, $\mathcal{N} = 200$. At low enough kicking strength, both variances are well saturated, as we demonstrate in Sec. 3.5.3 and Fig. 3.4.

strength, however, both variances are well saturated. We show that behavior at the kicking strength $V = 0.15$ in Sec. 3.5.3.

We wish to emphasize that our results show that a kicked interacting 1D bose gas can exhibit dynamical localisation over certain timescales and provided the system is initiated close to its ground state. Such conditions can be met within cold atom gas systems. This however does not rule out the possibility of delocalization at longer time scales or beyond the applicability of our methods e.g. at high
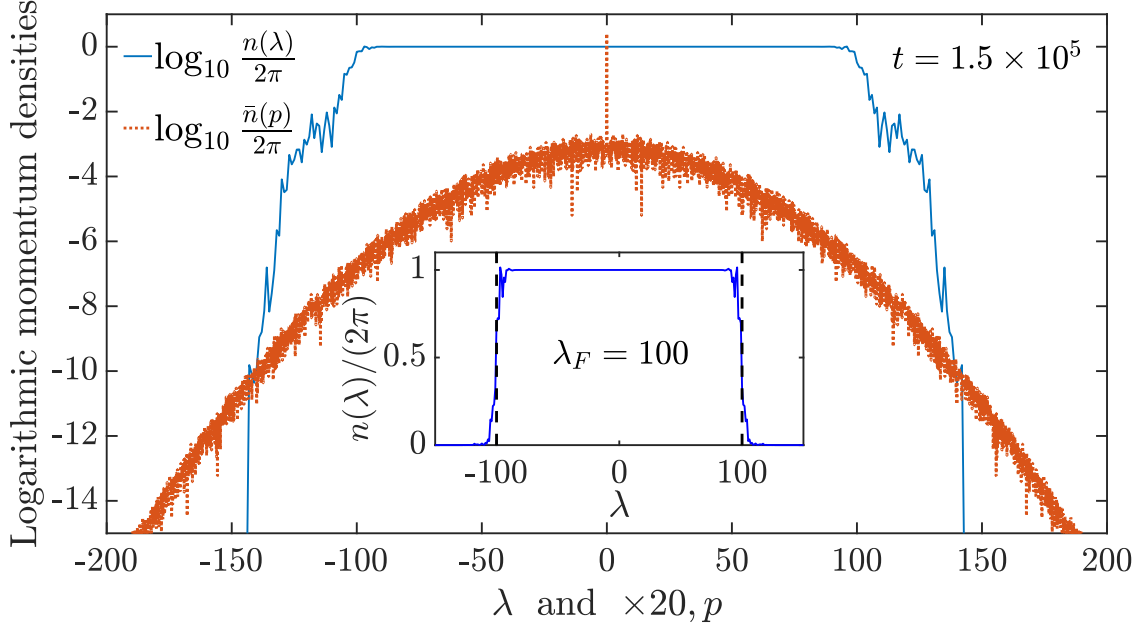
Figure 3.2: Main plot: decimal logarithms of the momentum densities at the end of the evolution. For $\bar{n}(p)$, all odd momentum components are zero, because we start with the uniform-density initial state and $q = 2$ (in units of $2\pi/L$). Only even components of $\bar{n}(p)$ are plotted therefore. Parameters: $V = 0.5$, $q = 4\pi/L$, $\gamma = 10$, $\mathcal{N} = 200$. Inset: normalized momentum density $n(\lambda)/(2\pi)$ in the linear scale. The Fermi momentum at our parameter choice is $\lambda_F = 100$.

temperature or larger kicking strength.

3.5   Additional Materials

3.5.1   Tonks-Girardeau Gas and Wigner Function

In the main text we provided a simple argument for the dynamical localization of the TG gas based on the exact wavefunction of the model. One can also examine it from a different perspective which can be more readily generalised to other cases. Through Fermi-Bose mapping we can write the TG Hamiltonian and the kicking

Hamiltonian as [150, 151]:

$$H_{\mathrm{TG}} = \int \mathrm{d}x \Psi^\dagger(x) \left[-\frac{\partial_x^2}{2m} \right] \Psi(x), \quad H_{\mathrm{K}} = \int \mathrm{d}x \, V \cos{(qx)} \Psi^\dagger(x) \Psi(x). \quad (3.19)$$

We then study the time evolution of the Wigner function [158]:

$$n(x, \lambda) = \int \mathrm{d}y \, e^{i\lambda y} \left\langle \Psi^\dagger(x + y/2) \Psi(x - y/2) \right\rangle, \quad (3.20)$$

which follows a two step pattern. Between the kicks, using the Heisenberg equations of motion this function evolves according to:

$$[\partial_t + v_{\mathrm{eff}}(\lambda)\partial_x] \, n(x, \lambda, t) = 0, \quad (3.21)$$

where $v_{\mathrm{eff}}(\lambda) = \lambda/m$. The solution of this equation is

$$n(x, \lambda, t + T^-) = n(x - \lambda T/m, \lambda, t). \quad (3.22)$$

Meanwhile, when considering the evolution over the kicks, we can use the fact that

$$e^{iH_{\mathrm{K}}} \Psi^\dagger(x) e^{-iH_{\mathrm{K}}} = e^{-iV \cos qx} \Psi^\dagger(x), \quad (3.23)$$

from which we get that

$$\tilde{n}(x, z, t + T^+) = e^{2iV \sin{(qz/2)} \sin{(qx)}} \tilde{n}(x, z, t + T^-) \quad (3.24)$$

where $\tilde{n}(x, z, t)$ is the Fourier transform of $n(x, \lambda, t)$ with respect to λ. Repeated application of this two-step evolution provides the full evolution of the TG Wigner function. This can be better achieved numerically by working in the Fourier space with respect to x, denoting the corresponding Fourier transform of $n(x, \lambda, t)$ as $\bar{n}(p, \lambda, t)$. Then, the free evolution is given by:

$$\bar{n}(p, \lambda, t + T^-) = e^{-ipv_{\mathrm{eff}}T}\bar{n}(p, \lambda, t). \tag{3.25}$$

Having determined $n(x, \lambda, t)$ at any time, we can then use it to find the density and momentum distribution function via integration over x or λ, respectively:

$$n(\lambda, t) = \int \mathrm{d}x\, n(x, \lambda, t), \tag{3.26}$$

$$\rho(x, t) = \int \frac{\mathrm{d}\lambda}{2\pi}\, n(x, \lambda, t). \tag{3.27}$$

The energy of the system is therefore given by:

$$E(t) = \int \frac{\mathrm{d}\lambda}{2\pi} \left[\frac{\lambda^2}{2m}\right] n(\lambda, t). \tag{3.28}$$

This method allows one to investigate the implications of different initial conditions. An initial trapping potential or finite temperature state could also be considered. Moreover, this approach can be generalized away from the TG limit to give the GHD approach presented in Sec. 3.4 [157].

The same analysis can be carried out in the free boson case with the exact

same evolution. The difference between the cases only arising in the choice of initial condition, for the TG gas a natural choice is the Fermi-Dirac distribution $n(x, \lambda, 0) = \Theta(\lambda_F - \lambda) - \Theta(-\lambda_F - \lambda)$, where λ_F is the Fermi momentum and $\Theta(x)$ the Heaviside function.

We conclude this section by noting an interesting relation to the classical kicked rotor system. Using the Heisenberg equations of motion for $n(x, \lambda, t)$, the effect of the kick can be determined via the solution of:

$$\partial_t n(x, \lambda, t) = \sum_{j=0}^{\infty} \delta(t - jT)V \sin(qx) \left[n(x, \lambda + q/2, t) - n(x, \lambda - q/2, t) \right]. \quad (3.29)$$

For a sufficiently smooth $n(x, \lambda, t)$ and small q the right-hand side can be expanded in a Taylor series. Retaining only the leading term in this sequence we have that the effect of the kick becomes

$$n(x, \lambda, t + T^+) = n(x, \lambda + Vq\sin(qx), t + T^-) . \quad (3.30)$$

Combining it with (3.22), we recover exactly the Chirikov standard map [8]. Such an approximation breaks down at zero temperature when the initial state is a Fermi function but may be appropriate at higher temperature.
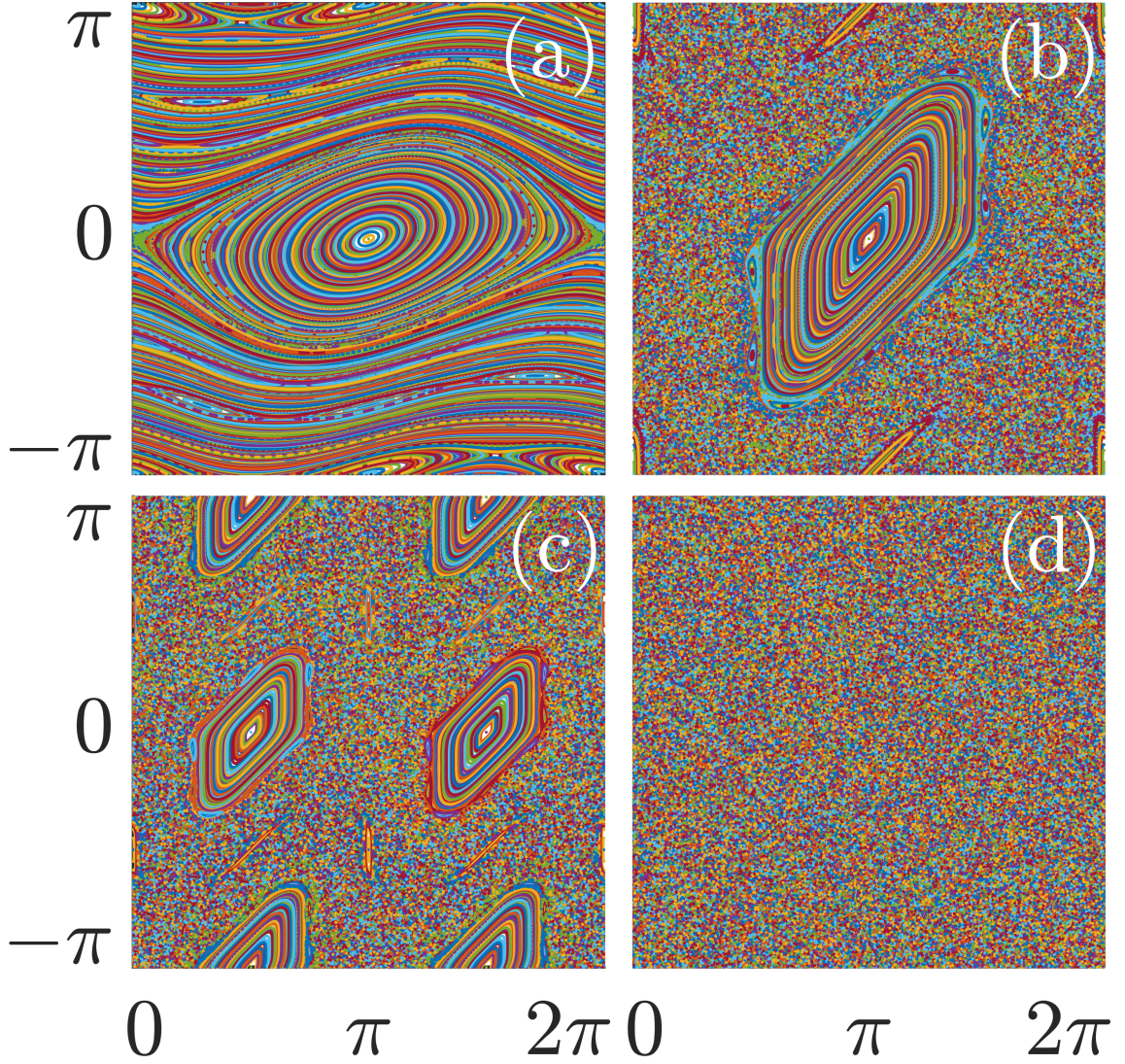
Figure 3.3: The phase portrait of Chirikov's standard map. (a) $V = 0.5$, $q = 1$; (b) $V = 2$, $q = 1$; (c) $V = 0.5$, $q = 2$; (d) $V = 2$, $q = 2$. The parameters as in panel (c) are used in the main text for the kicked Lieb-Liniger model.

3.5.2 Classical Kicked Rotor under a non-2π-periodic kicking potential

In this section, we show that the effective kicking strength in the classical single-particle analog of our model – the Chirikov's standard map – is modified. In particular, the Hamilton's equations of motion read:

$$\begin{cases} p_{n+1} = p_n + qV\sin(qx_n), & \mod 2\pi \\ \\ x_{n+1} = x_n + p_{n+1}, & \mod 2\pi \end{cases}, \tag{3.31}$$

where we adopt the units in which $x_n \in [0, 2\pi)$, $q \in \mathbb{Z}$, and, as one can check, both x_n and p_n are $2\pi/q$-periodic. Conventionally, $q = 1$. In case of general q, though, one can make a coordinate change: $\tilde{p}_n = qp_n$, $\tilde{x}_n = qx_n$ with the new coordinates $\tilde{x}_n \in [0, 2\pi q)$, which are 2π-periodic. In these coordinates, the equations read:

$$\begin{cases} \tilde{p}_{n+1} = \tilde{p}_n + q^2 V\sin(\tilde{x}_n), & \mod 2\pi q \\ \\ \tilde{x}_{n+1} = \tilde{x}_n + \tilde{p}_{n+1}, & \mod 2\pi q \end{cases}, \tag{3.32}$$

and it is customary to reduce the consideration to region of periodicity $\tilde{x}_n, \tilde{p}_n \in [0, 2\pi)$. In these coordinates, the conventional standard map at $q = 1$ is restored with the kicking strength parameter $\tilde{V} = q^2 V$. For example, at $q = 2$, kicking at $V = 0.5$ is equivalent to kicking the conventional map at $q = 1$ with $\tilde{V} = 4V = 2$ – well above the regular-to-chaotic transition at $V_{\text{cr}} \approx 0.97$. Fig. 3.3 demonstrates this correspondence.
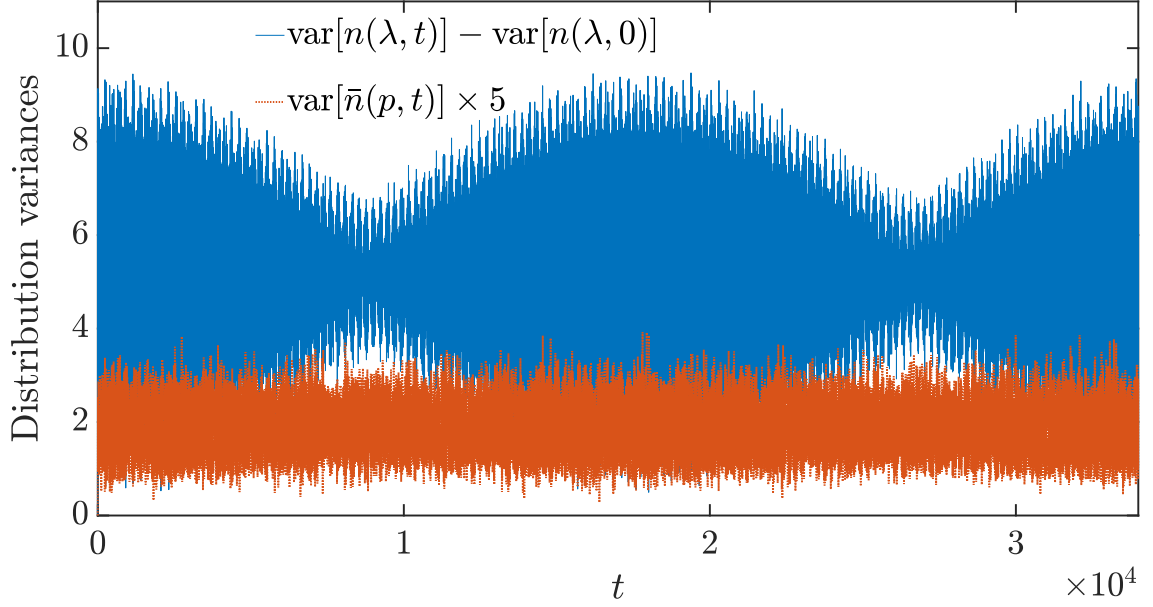
Figure 3.4: Upper solid blue curve: variance of the momentum density $n(\lambda, t)$ in the kicked Lieb-Liniger gas as a function of time relative to the initial variance: $\mathrm{var}[n(\lambda, t)] - \mathrm{var}[n(\lambda, 0)]$. It has oscillatory character that hints on certain underlying invariance in the system (possibly approximate) and hence at least transient dynamical localization. Lower dotted red curve: scaled variance of $\bar{n}(p, t)$. In this parameter regime, we reach its saturation, and GHD and our scheme may be applicable for long times without eventual delocalization. Parameters: $V = 0.15$, $q = 4\pi/L$, $\gamma = 10$, $\mathcal{N} = 200$.

3.5.3 Additional data and approximation justification

In this section, we have two goals. First, in Fig. 3.4, we demonstrate the regime, in which the variance of the Fourier transform of the spatial density is saturated, which is achieved at weaker kicking. Second, we show that our approximate scheme is justified. For that purpose, we employ the exact scheme described in the main text in order to compute the spatial density and effective velocity at short times and demonstrate the they are close to being constants with respect to the corresponding scales. In particular, in Fig. 3.5(a), the spatial density is shown to vary across the system by less than 0.4% of its average value.
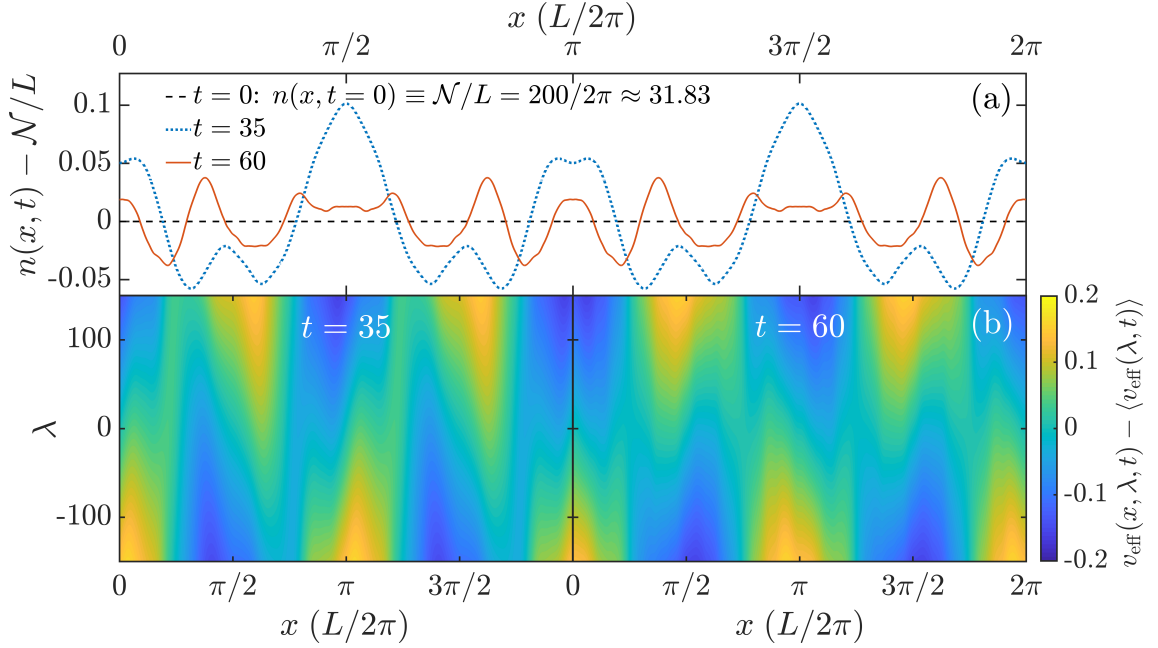
Figure 3.5: (a) Spatial density profile, $n(x,t) = \int \frac{d\lambda}{2\pi} n(x,\lambda,t)$, calculated at two different times using the exact scheme from the main text. Both cases demonstrate less than 0.4% deviation from the constant average density of $\mathcal{N}/L = 200/2\pi \approx 31.83$. (b) The deviation of the effective velocity from its mean value, $v_{\text{eff}}(x,\lambda,t) - \langle v_{\text{eff}}(\lambda,t)\rangle$, where $\langle \ldots \rangle$ represents averaging over the position x. Obtained via the exact method discussed in the main text. Left and right panels show examples at the same times as in panel (a). Parameters are the same as in the main text: $V = 0.5$, $q = 4\pi/L$, $\gamma = 10$.

Chapter 4: Transport and Localization in Rippled Channels and Localization Landscape

4.1 Introduction

In this chapter, we briefly consider a geometric analog of Anderson localization in rippled channels and show how a recently developed powerful concept of localization landscape manifests in some of the most intuitive scenarios.

Transport in rippled channels (or waveguides) has been studied theoretically in both classical and quantum regimes. In Refs. [164, 165, 166, 167], classical polygonal channels were considered, Refs. [168, 169] studied junctions, and Refs. [170, 171] are on sinusoidal channels. Quantum transport in sinusoidal channels is considered in Refs. [172, 173]. Experimental realization was demonstrated in Refs. [174, 175]. In all of these works (except those on the junctions), only periodic walls are studied. The dynamical properties of elementary cells of these channels, which can be regarded as billiards, are connected with the transport properties, such as diffusion and resistance, in the channels.

We study quantum transport in a different kind of rippled channels by examining their finite segment in two different regimes: (i) the segment is composed

of periodic structures and (ii) the segment is disordered. We show that, following the natural expectation, in the former case, the segment eigenstates are extended, while in the latter case, they are well localized to individual cells of the segment. We further show how this expected result can be inferred from the novel concept of localization landscape.

4.2   Localization landscape

Recently, there has been a wave of new mathematical developments in a very old field studying elliptic differential operators, their eigenfunctions, and density of states. In Ref. [17], the concept of localization landscape was suggested to predict universally the spatial structure of localized eigenstates and the gradual percolation that occurs as one moves up the energy spectrum[1]. The problem formulation is very general. Consider a static Schrödinger equation – an eigenvalue problem – for a Hamiltonian $H = -\dfrac{\hbar^2}{2m}\nabla^2 + V$, which is an elliptic differential operator as long as V is an everywhere non-negative potential:

$$\left(-\frac{\hbar^2}{2m}\nabla^2 + V\right)\psi = E\psi \quad \text{in} \quad \Omega, \qquad \psi|_{\partial\Omega} = 0, \tag{4.1}$$

where Ω is a certain domain. This eigenvalue problem can be very difficult to solve depending on the complexity of the potential and the domain geometry. Instead of solving it directly, however, consider the Dirichlet problem with uniform right-hand

---

[1]It was supplemented further with a dual landscape in Ref. [176].

side and Dirichlet boundary conditions:

$$\left(-\frac{\hbar^2}{2m}\nabla^2 + V\right)u = 1 \quad \text{in} \quad \Omega, \qquad u|_{\partial\Omega} = 0. \tag{4.2}$$

The solution u of this equation is everywhere positive and is called the localization landscape. Its valleys and ridges determine the locations of low-energy localized eigenfunctions of Eq. (4.1), as well as the percolation patterns that develop as we consider eigenstates of higher energies. The reason for this accurate correspondence is the following bound:

$$\forall \vec{r} \in \Omega : \ |\psi(\vec{r})| \leq Eu(\vec{r}), \tag{4.3}$$

which is formulated and proven in Ref. [17]. The notations here assume a specific normalization of the eigenfunction ψ, such that $\sup_{\Omega} |\psi| = 1$. The eigenvalue E in the right-hand side corresponds to the eigenfunction ψ. Note that the function u, defined in Eq. (4.2), is universal for the Hamiltonian H and does not depend on the eigenvalue E or eigenfunction ψ in Eq. (4.3). Therefore, the lines of local minima of u define the borders between the regions hosting separate localized states at low energies. As the energy grows, however, the bound in Eq. (4.3) becomes less tight, and percolation occurs. The lower the line of minima of u is, the higher up in spectrum one has to go in order to see percolation through that line. The localization landscape was soon shown to be observable and was directly measured experimentally [177].

Later, a directly related effective confining potential, which reflects the prop-

68

erties of the eigenfunctions, was found in Ref. [178]. It turned out to be simply the inverse of the localization landscape: $W = 1/u$, and appeared to govern the exponential decay of localized eigenstates. In order to show that, in Ref. [178], the auxiliary function φ, such that $\psi \equiv u\varphi$ is introduced. For this function, Eq. (4.1) translates into:

$$-\frac{\hbar^2}{2m}\nabla^2\varphi - 2\frac{\hbar^2}{2m}\left(\frac{\vec{\nabla}u}{u} \cdot \vec{\nabla}\varphi\right) + \frac{1}{u}\varphi = E\varphi \quad \text{in} \quad \Omega, \qquad \varphi|_{\partial\Omega} = 0. \qquad (4.4)$$

Then it was suggested to insert an additional term proportional to $\vec{\nabla}\varphi$ to arrive at a compact form:

$$-\frac{\hbar^2}{2m}\left[\frac{1}{u^2}\left(\vec{\nabla} \cdot u^2\vec{\nabla}\varphi\right)\right] + W\varphi = E\varphi. \qquad (4.5)$$

Note that this Schrödinger-type equation for the function φ does not include the original potential V, but instead only features the effective confining potential W, which is, just as the localization landscape u, uniform throughout the spectrum. This approach was further thoroughly tested numerically in Ref. [179] and proven rigorously in Ref. [180]. Very recently, an even deeper insight was extracted from localization landscape. It turned out that it allows to build a uniformly accurate estimate for density of states throughout the whole spectrum [181] – a strong generalization of the Weyl's asymptotic law [182].
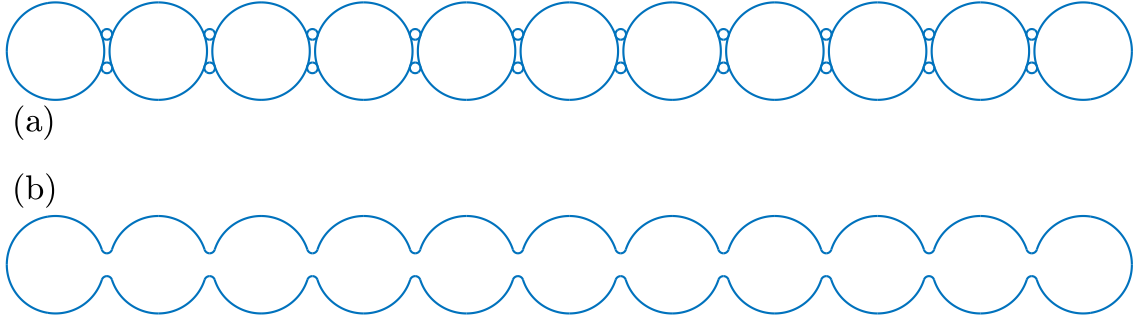
Figure 4.1: Channel segment in the regular regime. (a) The circles whose arcs constitute the boundary. (b) The resulting boundary that encloses the domain Ω. It is obtained by connecting the arcs of large and small circles at the points of their contact, so that the boundary is C^1-smooth.
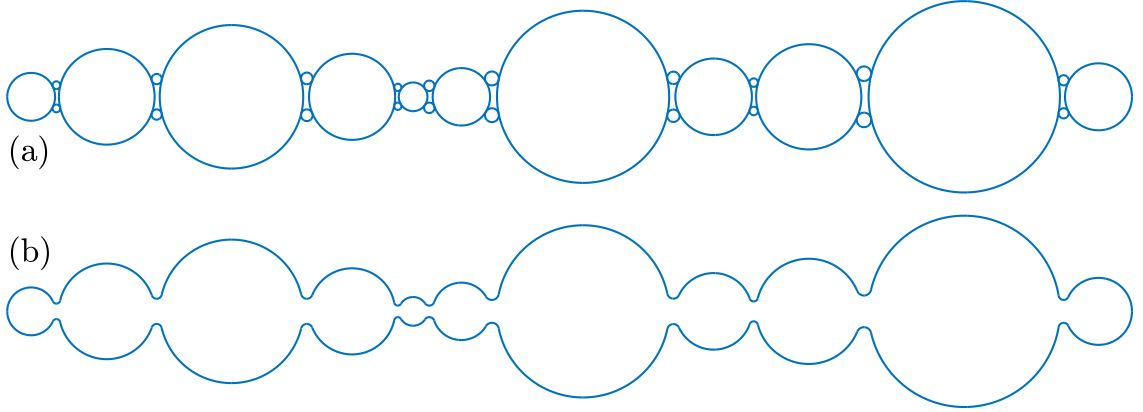
Figure 4.2: Channel segment in the disordered regime. (a) The circles whose arcs constitute the boundary. (b) The resulting boundary that encloses the domain Ω. It is obtained by connecting the arcs of large and small circles at the points of their contact, so that the boundary is C^1-smooth.

4.3   Model

We consider a two-dimensional billiard that represents a long segment of a rippled channel in two regimes – regular and disordered. Its walls consist of arcs of circles that touch externally [see Figs. 4.1(a) and 4.2(a)], so that the boundary is C^1-smooth, as shown in Figs. 4.1(b) and 4.2(b) [183].   The eigenvalue problem we

solve reads:

$$-\frac{1}{2}\nabla^2\psi = E\psi \quad \text{in} \quad \Omega, \qquad \psi|_{\partial\Omega} = 0, \tag{4.6}$$

where Ω is the billiard (channel segment) under consideration. We consider two cases. First, the arc radii of the circles repeat periodically, so that the spectra of individual circular sites are in resonance, allowing for hybridization of the individual eigenstates, similar to what happens when atomic eigenstates combine into those of a solid crystal. In the second scenario, we make the arc radii uniformly random. As a result, the spectra of individual circular sites are off-resonant with respect to each other, and, consequently, the eigenstates of the channel feature strong localization, similar to that in the foundational Anderson model [11].

4.4 Eigenstates of Rippled Channel and Localization Landscape

We use finite-element method to compute eigenstates of a domain. Our numerical scheme for this kind of problems is described in detail in Chapters 6 and 7. Ultimately, we associate localized eigenstates with low conductivity and lack of transport (or poor transport), while we regard extended eigenstates as "conducting" – in the same way as it is done in Anderson localization. However, a more rigorous and direct study of geometric transport in rippled channels would be an interesting direction for future work.

In Fig. 4.3, we demonstrate a number of low-energy eigenstates in the disordered regime on top of the effective confining potential $W = 1/u$ calculated from

the localization landscape u found as:

$$-\frac{1}{2}\nabla^2 u = 1 \quad \text{in} \quad \Omega, \qquad u|_{\partial\Omega} = 0. \tag{4.7}$$

As one can see, apart from the lack of resonant hybridization, the effective potential demonstrates high barriers between the channel sites, and the larger the difference between the adjacent site radii is, the higher the barrier is. Naturally, it should also depend on junction widths – or site-to-site coupling – which we have not explored. In Fig. 4.4, we demonstrate the eigenfunctions and the effective confining potential in the periodic regime. One can see the striking distinction – all the eigenstates are clearly delocalized in this case. In general, this model is intuitive and demonstrates all the properties that we naturally expected to see there. But the purpose is to demonstrate how the effective potential calculated from the localization landscape can be used to predict transport properties of a channel by examining its barrier structure. The approach can be applied to less obvious cases to determine conductive properties of rippled channels.
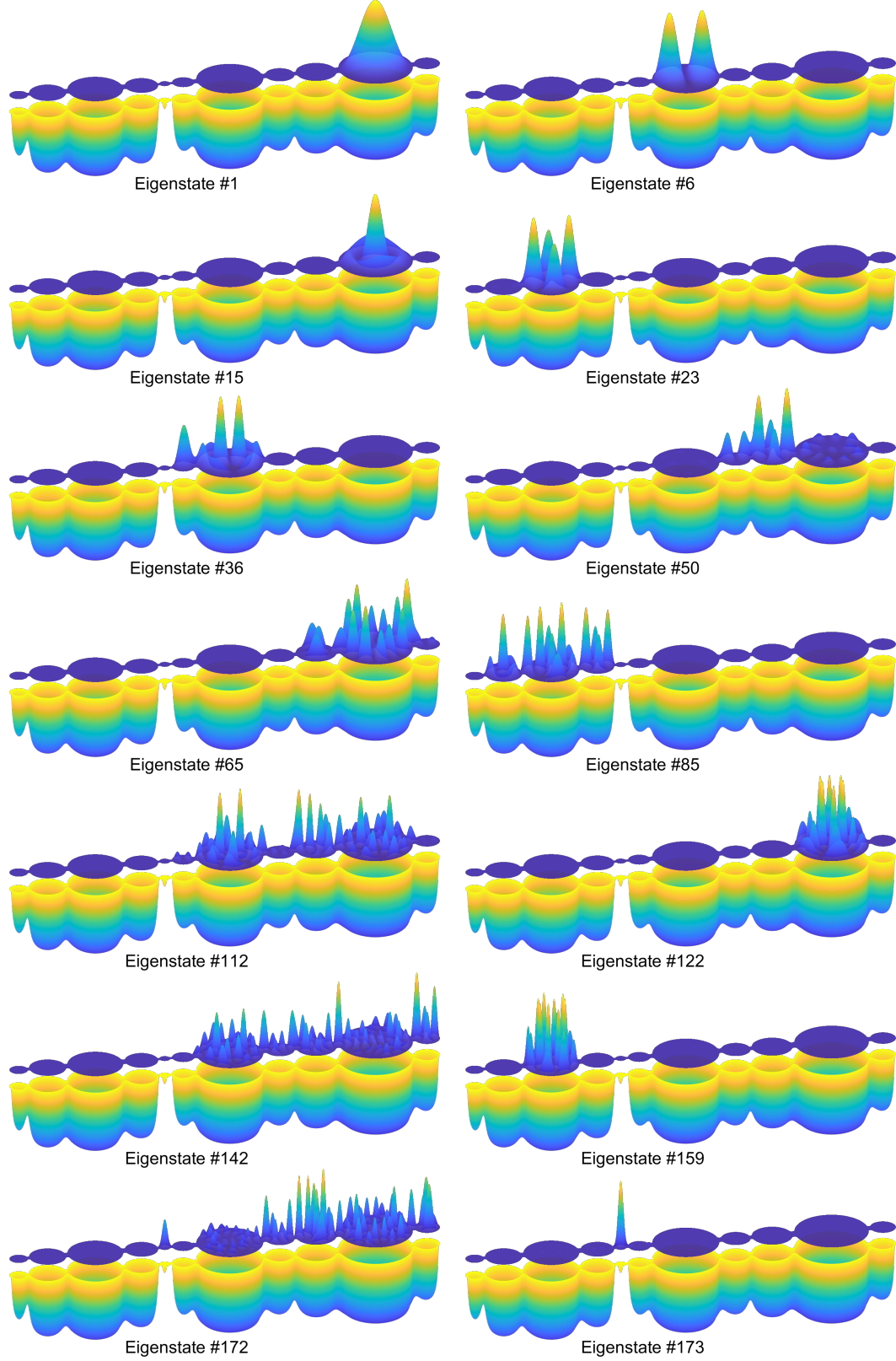
Figure 4.3: 14 examples of eigenfunctions of the channel segment on top of the effective confining potential W in the *disordered* regime. Upper surfaces demonstrate $|\psi|^2$. Lower surfaces depict the effective potential W.

73
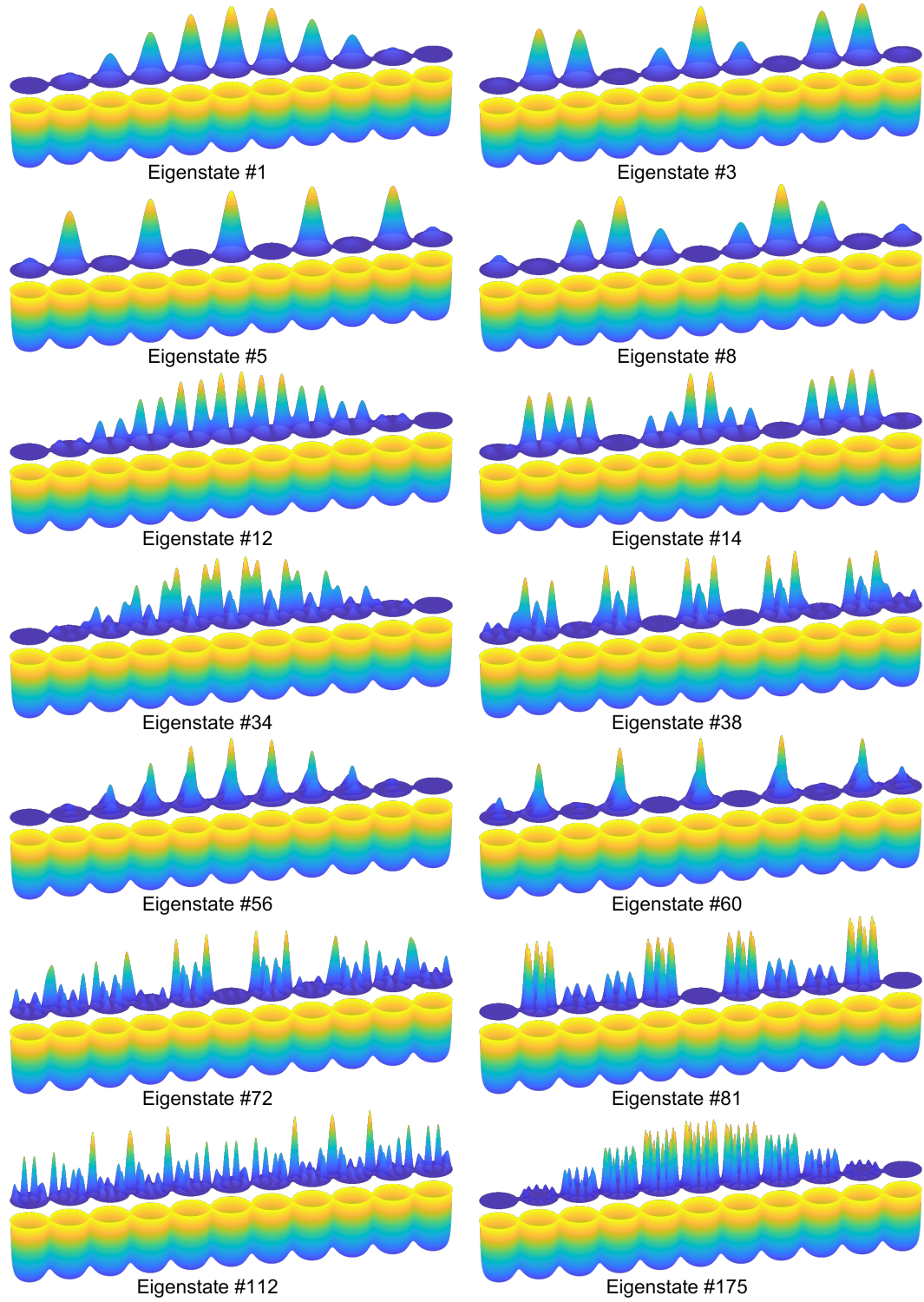
Figure 4.4: 14 examples of eigenfunctions of the channel segment on top of the effective confining potential W in the *periodic* regime. Upper surfaces demonstrate $|\psi|^2$. Lower surfaces depict the effective potential W.

Chapter 5: Lyapunov Exponent and Out-of-Time-Ordered Correlator's Growth Rate in a Chaotic System

5.1   Introduction

One of the central goals in the study of quantum chaos is to establish a correspondence principle between classical and quantum dynamics of classically chaotic systems [4, 5, 6, 50, 67, 76, 184, 185, 186, 187, 188]. Several previous works [6, 12, 13, 108, 189, 190, 191] have attempted to recover fingerprints of classical chaos in quantum dynamics. In particular, Aleiner and Larkin [192, 193, 194] showed the existence of a semiclassical "quantum chaotic" regime attributed to the delay in the onset of quantum effects (due to weak localization) revealing the key measure of classical chaos – the Lyapunov exponent (LE). Recently, the subject of quantum chaos has been revived by the discovery of an unexpected conjecture that puts a bound on the growth rate of an out-of-time-ordered four-point correlator (OTOC) [27, 28]. OTOC was first introduced by Larkin and Ovchinnikov to quantify the regime of validity of quasi-classical methods in the theory of superconductivity [26]. The growth rate of OTOC appears to be closely related to LE. Recent works have proposed experimental protocols to probe OTOC in cold atom

and cavity QED setups [195, 196]. Several recent preprints have employed OTOC as a probe to characterize many-body-localized systems [197, 198, 199, 200].

In Sec. 5.3, we calculate the Lyapunov exponent, OTOC and the two-point correlator for the quantum kicked rotor (QKR), which is a canonical driven model of quantum chaos [5, 49, 50, 201] (see Sec. 5.2 for details). The classical version of this model manifests regular-to-chaotic transition (as a function of driving strength K) which enables us to benchmark the behavior of OTOC against the presence and absence of classical chaos. We show that in the limit of small dimensionless effective Planck's constant, $\hbar_{\text{eff}} \to 0$, there exists a "quantum chaotic" regime [26, 192, 193, 194] at early times where OTOC, $C(t) = -\left\langle [\hat{p}(t), \hat{p}(0)]^2 \right\rangle$, grows exponentially. This correlator's growth rate, $\tilde{\lambda}$, that we abbreviate for brevity as CGR, is found to be independent of the dimensionless Planck's constant, $\hbar_{\text{eff}}$, and is purely classical at early times for the kicked rotor. Most importantly, the CGR and the standard definition of LE in classical systems are shown to be different at all non-zero kicking strengths. In particular, for the classically regular regime, $K < K_{\text{cr}}$, CGR significantly exceeds LE due to much higher sensitivity to the presence of small chaotic islands. For the classically deeply chaotic regime, $K \gg K_{\text{cr}}$, CGR exceeds LE by nearly a constant. We attribute these distinctions to different averaging procedures carried out to extract these exponents and posit that this statement may be more general than the specific QKR model studied here.

We also show that deviations from the essentially classical behavior of OTOC, $C(t) \sim e^{2\tilde{\lambda}t}$, occur sharply at a time of the order of the Ehrenfest time, t_E, where OTOC exhibits a clear cusp. This corresponds to the minimal time it takes classical

trajectories to self-intersect indicating the onset of quantum interference effects [192, 193, 194]. This is in analogy to the weak dynamical localization discussed by Tian et al. [202]. At longer times, $t > t_E$, the quantum disordering effects subdue the exponential growth dictated by the CGR to a power-law growth.

Next, we calculate the two-point correlation function and show that CGR, $\tilde{\lambda}$, is not revealed in this quantity (nor in the single-point average – e.g., the kinetic energy as has been well known [6]). However, in Sec. 5.4, we find that the two-point correlator does contain fingerprints of classical transition from regular dynamics to chaos even deep in the quantum regime at long times, which has been a subject of long-standing theoretical and experimental interest [203, 204, 205, 206].

Finally, in Sec. 5.5 we go beyond the Ehrenfest time and introduce a scaling law for OTOC at all times and sufficiently strong chaoticity ($K \gtrsim 10$) that allows to unify the quantum Lyapunov exponent, which is no longer a constant, but a function of time at $t > t_E$ across dimensions of the parameters K and $\hbar_{\text{eff}}$ and time.

5.2 Quantum Kicked Rotor

The dimensionless Hamiltonian of QKR [5, 49, 50, 201] can be written as

$$\hat{H} = \frac{\hat{p}^2}{2} + K \cos(\hat{x})\Delta(t), \tag{5.1}$$

where $\Delta(t) = \sum_{j=-\infty}^{\infty} \delta(t-j)$ is the sum of $\delta-$pulses, $\hat{p}$ is the dimensionless angular-momentum operator, $\hat{x}$ is the angular coordinate operator, and t is the dimensionless time. The QKR is characterized by two parameters. One of them, the kicking

strength K, comes from the classical kicked rotor (KR, also called Chirikov standard map) [8]. Another parameter is the dimensionless effective Planck constant $\hbar_{\text{eff}}$, which enters the dimensionless angular momentum operator ($\hat{p} = -i\hbar_{\text{eff}}\frac{\partial}{\partial x}$) and the dimensionless Schrödinger equation: $i\hbar_{\text{eff}}\frac{\partial}{\partial t}\left|\Psi\right\rangle = \hat{H}\left|\Psi\right\rangle$. The eigenvalues of $\hat{p}$ are quantized in units of $\hbar_{\text{eff}}$ due to the periodic boundary conditions. Note that in the classical KR, the parameter $\hbar_{\text{eff}}$ is absent. In order to understand how classical chaos emerges from quantum dynamics, we compute OTOC and the two-point correlator in the regime of $\hbar_{\text{eff}} \to 0$ at short time scales.

5.3 Lyapunov Exponent and OTOC's growth rate (CGR)

To specify our quantum diagnostics for chaotic behavior in the QKR, we choose OTOC, $C(t)$ [26, 28], and two-point correlator, $B(t)$, as:

$$C(t) = -\left\langle [\hat{p}(t), \hat{p}(0)]^2 \right\rangle, \quad B(t) = \text{Re}\left\langle \hat{p}(t)\hat{p}(0) \right\rangle. \tag{5.2}$$

We point out that $C(t)$ is closely related to the Loschmidt echo (also known as fidelity). In the previous works, fidelity has been used as a theoretical and experimental diagnostic of quantum chaos [195, 207, 208, 209, 210, 211, 212, 213, 214].

Before carrying out quantum calculations, we consider the classical correspondence of $C(t)$ [26, 28]. At short times $t < t_E$ [1]:

$$C(t) = \hbar_{\text{eff}}^2 \left\langle \left(\frac{\partial \hat{p}(t)}{\partial x(0)} \right)^2 \right\rangle \approx \hbar_{\text{eff}}^2 \left\langle\!\!\left\langle \left(\frac{\Delta p(t)}{\Delta x(0)} \right)^2 \right\rangle\!\!\right\rangle = C_{\text{cl}}(t), \tag{5.3}$$

---

[1]See Fig. 5.11 in Sec. 5.6.5 for comparison between $C(t)$ and $C_{\text{cl}}(t)$.

where we changed the expectation value of the operator derivative to the finite differences of the classical variables averaged over the phase space ($\langle\!\langle \ldots \rangle\!\rangle$ denotes classical phase-space average). Note that the averaging allows for direct comparison of the classical $C_{\text{cl}}(t)$ to the quantum $C(t)$. Such a comparison would not always be possible for local quantities because of quantum wave-packet spreading. Due to the presence of chaotic regions in the phase space, $C_{\text{cl}}(t) \sim e^{2\tilde{\lambda}t}$ grows exponentially. Now we compare this classical CGR, $\tilde{\lambda} = \lim\limits_{t\to\infty} \lim\limits_{\Delta x(0)\to 0} \frac{1}{2t} \ln \frac{C_{\text{cl}}(t+1)}{C_{\text{cl}}(1)}$, to the standard definition of the LE: $\lambda = \left\langle\!\!\!\left\langle \lim\limits_{t\to\infty} \lim\limits_{d(0)\to 0} \frac{1}{t} \ln \frac{d(t)}{d(0)} \right\rangle\!\!\!\right\rangle$ [2] (where $d(t) = \sqrt{[\Delta x(t)]^2 + [\Delta p(t)]^2}$). Notice that there are key differences between definitions of λ and $\tilde{\lambda}$ coming from the different orders of squaring, averaging, taking ratio and applying logarithm.

Next, we proceed to check if the classical correspondence follows through in a quantum calculation of $C(t)$ and compare the rate of exponential growth of $C(t)$ to $\tilde{\lambda}$ extracted from $C_{\text{cl}}(t)$ and to LE λ. For the quantum case, the averaging in Eq. (5.2) is performed in the Schrödinger picture over some initial state $|\Psi(0)\rangle$. We use individual angular-momentum eigenstates $|\Psi(0)\rangle = |n\rangle : \hat{p}|n\rangle = \hbar_{\text{eff}} n |n\rangle$ and Gaussian wave-packets:

$$|\Psi(0)\rangle = \sum_{n=-\infty}^{\infty} a_n^{(0)} |n\rangle, \quad a_n^{(0)} \sim \exp\left[-\frac{\hbar_{\text{eff}}^2 (n - n_0)^2}{2\sigma^2}\right], \tag{5.4}$$

where $n_0 = p_0/\hbar_{\text{eff}}$. In this calculation, we use wave-packet (5.4) with $p_0 = 0$ and $\sigma = 4$. Numerically, $|\Psi\rangle$ is represented in a finite basis of eigenstates $|n\rangle$, $n \in [-N; N-1]$. All functions of only $\hat{p}$ are applied in this basis, and all functions

---

[2]See Sec. 5.6 for details on definition and calculation of the classical Lyapunov exponent.

of only $\hat{x}$ are applied in the Fourier-transformed representation. We use adaptive grid with $2\hbar_{\text{eff}}N \in [2^7; 2^{16}]$, so that all physical observables are well converged. The wave-function is evolved by switching between representations back and forth and applying the Floquet operator $\hat{F} = e^{-i\hat{p}^2/2\hbar_{\text{eff}}}e^{-iK\cos(\hat{x})/\hbar_{\text{eff}}}$ in parts. Then the correlators are calculated in the Schrödinger picture.

The exponential growth of $C(t)$ lasts between the time t_d and the Ehrenfest time t_E [4, 28, 185]. To achieve a hierarchical separation between t_d and t_E ($\frac{t_E}{t_d} \gg 1$) for the QKR, we have to tune both K and $\hbar_{\text{eff}}$. The estimates of $t_d \sim [\ln(K/2)]^{-1}$ and $t_E \sim \frac{|\ln \hbar_{\text{eff}}|}{\ln(K/2)}$ at $K > 4$ guide our choice of parameters to achieve this separation. The smallest $\hbar_{\text{eff}}$ within the scope of our numerics is $\hbar_{\text{eff}} = 2^{-14}$. For this value of $\hbar_{\text{eff}}$, the Ehrenfest time is in the range $7 \lesssim t_E \lesssim 17$ kicks for the range of kicking strength $0.5 \leq K \leq 10$. By $K = 1000$, t_E shrinks down to 3 kicks, but at these values of K, it appears to be enough to extract a well averaged exponent. For the above mentioned parameter regimes, we numerically observe the exponential growth of $C(t)$ at early times ($t < t_E$) as shown in the Fig. 5.1, upper panel. Fig. 5.1 also shows that t_E decreases upon increasing the kicking strength K for fixed $\hbar_{\text{eff}}$. In contrast to $C(t)$, the two-point correlator $B(t)$ saturates at time $t \sim 2$ kicks (Fig. 5.1, lower panel).

Equipped with the early time behavior of $C(t)$, we are in a position to extract the rate of its exponential growth, i.e obtain CGR from the quantum calculation. We carry out a four-pronged comparison between CGR from the quantum calculation of $C(t)$, CGR from the classical calculation of $C_{\text{cl}}(t)$, numerically obtained LE for KR and analytical estimates (5.5) of LE from Chirikov's standard map analysis [8].
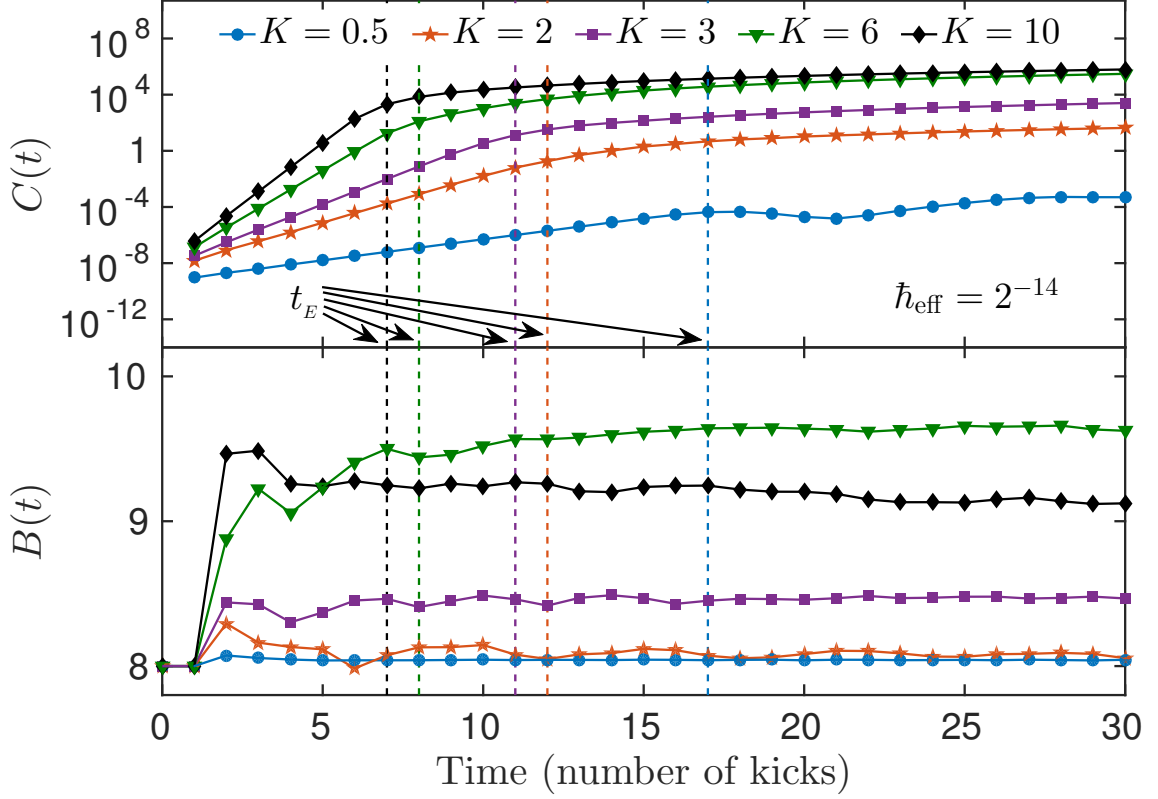
Figure 5.1: The upper panel shows OTOC, $C(t)$, vs t in the semi-log scale for various values of the kicking strength ($K = 0.5, 2, 3, 6, 10$) and $\hbar_{\text{eff}} = 2^{-14}$. The lower panel is a plot of the two-point function, $B(t)$, vs t at the corresponding parameters (in the linear scale). Averaging is performed over the Gaussian wave packet defined in Eq. (5.4) with $p_0 = 0$ and $\sigma = 4$.

The Chirikov's analytical formula reads:

$$\lambda \approx \frac{1}{2\pi} \int_{-\pi}^{\pi} dx \ \ln L(x), \tag{5.5}$$

where

$$L(x) = \left| 1 + \frac{k(x)}{2} + \mathrm{sgn}[k(x)] \sqrt{k(x) \left(1 + \frac{k(x)}{4}\right)} \right| \tag{5.6}$$

and $k(x) = K \cos x$. The simplified expression $\lambda \approx \ln(K/2)$ valid at large K is obtained by substituting $L(x) \approx |k(x)|$ into Eq. (5.5) [8] [3].

In Fig. 5.2, we compare the exponents obtained in four ways listed above. In order to extract the exponents from $C(t)$, we determine the times, after which the exponential growth starts slowing down, and fit $C(t)$ from $t = 1$ up to these times to the function $ae^{2\lambda_{\mathrm{fit}}(t-1)}$ to find the parameter λ_{fit} ($C(0) = 0$, so we omit $t = 0$).

Numerical calculations of the classical LE and of the classical CGR [i.e. the growth rate of $C_{\mathrm{cl}}(t)$] are performed using the map tangent to the standard map – this standard procedure is outlined in Sec. 5.6. Notice that the exponents extracted from $C(t)$ (quantum CGR) and from $C_{\mathrm{cl}}(t)$ (classical CGR) are in an excellent agreement for all values of K. Both classical and quantum CGRs significantly exceed LE at $K < K_{\mathrm{cr}}$. This indicates that CGR may not be a reliable tool for discriminating between classically regular and chaotic dynamics in a global sense, but it can be employed to detect the existence of local disconnected chaotic islands more efficiently than LE. As expected, numerically calculated values and analytical estimates of the classical LE agree with each other for $K \gtrsim 3$. At large K, the

---

[3]See Sec. 5.6 for details.
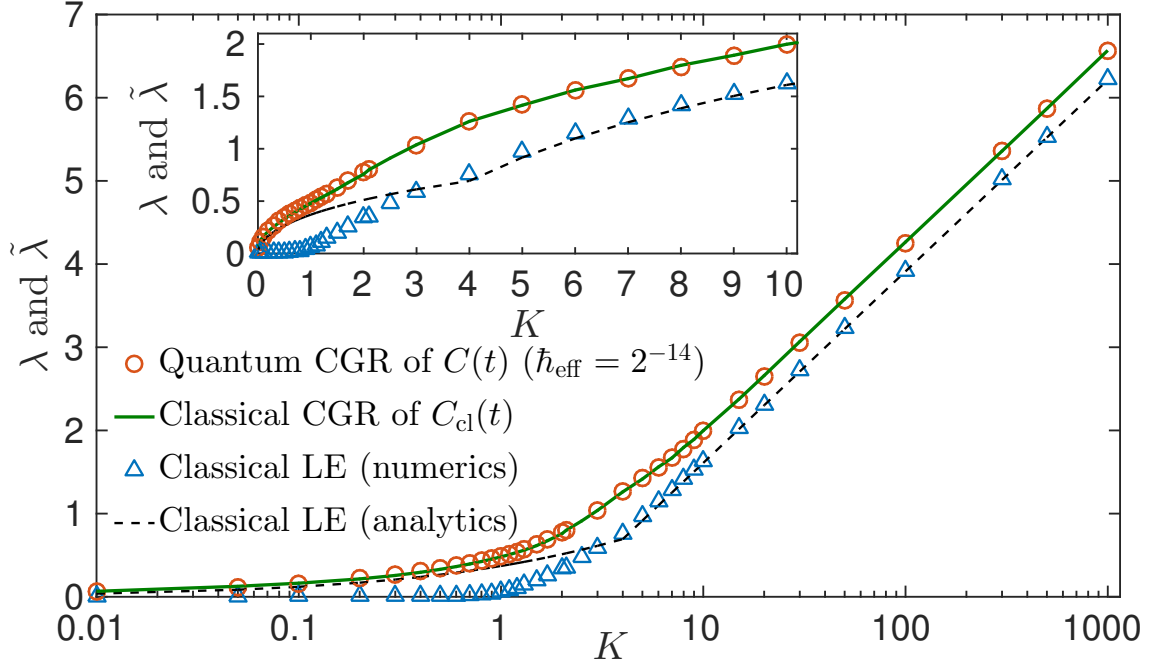
Figure 5.2: Red circles: early-time growth rate of $C(t)$ at $\hbar_{\text{eff}} = 2^{-14}$ (quantum CGR). The rest of the data is classical. Green solid line: growth rate of $C_{\text{cl}}(t)$ (classical CGR). Blue triangles: LE calculated numerically. Black dashed line: LE according to the Chirikov's analytical formula (5.5). The main plot and the inset show the same data in lin-log and linear scales, respectively (and in different ranges). At $K \gtrsim 8$, the difference between CGR and LE is constant $\approx \ln\sqrt{2}$. The initial state in $C(t)$ is the Gaussian (5.4) with $p_0 = 0$ and $\sigma = 4$. Fitting details for extracting CGR from $C(t)$ and $C_{\text{cl}}(t)$ are given in the main text.

difference between CGR and LE becomes nearly constant $\approx \ln\sqrt{2}$. We attribute this distinction primarily to the difference in the order of averaging in CGR and LE.

Now we proceed to consider the deviation of $C(t)$ from its classical counterpart $C_{\mathrm{cl}}(t)$ that manifests sharply at a time close to t_E. The onset of this deviation in OTOC is closely related to the weak dynamical localization effects [202]. In Fig. 5.3, we plot $\ln[C(t)]/2t$ as a function of time t in the log-log scale. This plot is constant [corresponding to the exponential rise of $C(t)$] at early times. Beyond t_E, the exponential growth slows down to a power-law growth (nearly quadratic growth around $t \sim 100$ kicks). At long times, the growth of $C(t)$ slows down further, but numerics quantifying this slowdown is out of the scope of the present manuscript. However, we can unambiguously extract the exponent associated with the exponential growth prior to t_E. Note that in the range of K and $\hbar_{\mathrm{eff}}$ where the region of the exponential growth of $C(t)$ is present ($t_E \geq 3$), $\tilde{\lambda}$ does not depend on $\hbar_{\mathrm{eff}}$ (see Fig. 5.3, inset).

5.4 Regular-to-chaotic transition in long-time quantum dynamics

Classical KR is famous for its transition from regular motion to chaotic behavior that occurs as K is increased above $K = K_{\mathrm{cr}} \approx 0.97$. The chaotic phase is characterized by the quasi-random walk in the angular-momentum space that leads to diffusion in angular momentum, so that the rotor's energy averaged over the phase space grows linearly with time (number of kicks). On the other hand, at long times QKR undergoes dynamical localization (which is closely connected to
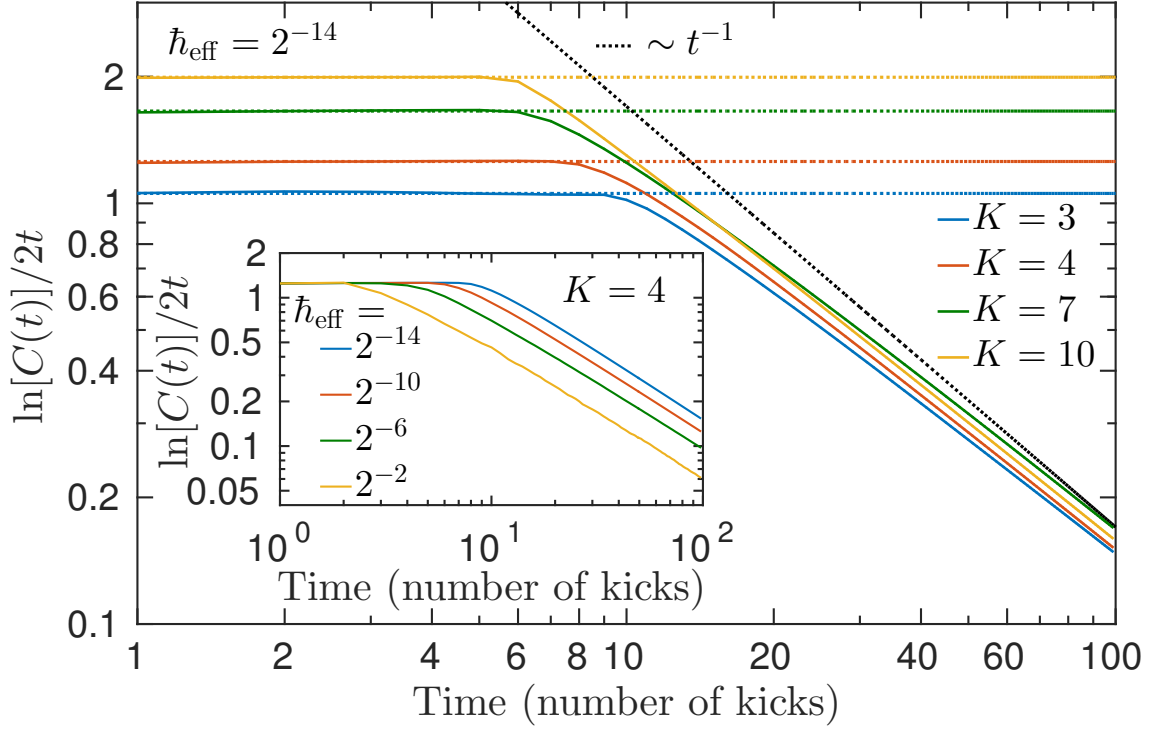
Figure 5.3: Main plot: $\ln[C(t)]/2t$ vs t in the log-log scale for $K = 3, 4, 7, 10$ (from bottom to top line, respectively) and $\hbar_{\text{eff}} = 2^{-14}$. The flat region at early times quantifies the exponential growth rate of $C(t)$. This flat region persists up to the time t_E, at which the exponential growth slows down to a power-law growth with a slowly decreasing power. Dotted lines are the eye guides: horizontal lines extend the flat regions, sloped line is shown for power comparison. Inset: $\ln[C(t)]/2t$ vs t in the log-log scale for $K = 4$ and $\hbar_{\text{eff}} = 2^{-14}, 2^{-10}, 2^{-6}, 2^{-2}$ (from top to bottom line, respectively). The rate of exponential growth is the same for different values of $\hbar_{\text{eff}}$, but t_E shrinks when $\hbar_{\text{eff}}$ increases.

Anderson localization in disordered solids [12]) and around $\hbar_{\mathrm{eff}} \sim 1$, the standard diagnostic – the average energy, i.e. the one-point correlator – seems insensitive to the presence or absence of classical chaos [5, 50]. Thus a question arises: is there a quantum diagnostic that manifests a robust signature of regular-to-chaotic classical transition in the purely quantum dynamics even in the dynamically localized regime ($\hbar_{\mathrm{eff}} = 1$, $t_d \gg t_E$)? Remarkably, the two-point correlator [$B(t)$ in Eq. (5.2)] contains a sharp signature of the classical transition [4]. In particular, we consider $B(t)$ averaged over time within various windows τ:

$$\overline{B}_\tau = \frac{1}{\tau} \sum_{t=0}^{\tau} \mathrm{Re} \langle p(t)p(0) \rangle. \tag{5.7}$$

As shown in Fig. 5.4, this averaged correlator maintains a sharp step-like structure as a function of K for several orders of magnitude in τ (we reached as large window as $\tau = 3 \times 10^9$, which is many orders of magnitude longer than any characteristic time scale in the system). This implies that at very long times, the quantum system does not lose the information about the classical transition. The plot supports the following very intuitive statement. The larger the chaotic fraction of the classical phase space is, the shorter the correlation-decay time window becomes (for explicit demonstration of this behavior, the dependence of $\overline{B}_\tau$ on the averaging window size τ is given in Sec. 5.6.6, Fig. 5.12). Therefore, we can relate $\overline{B}_\tau$ to the regular part of the phase space weighted by the initial Wigner distribution $P(x, p)$ of QKR (see Fig. 5.5 for illustration). However, $\overline{B}_\tau$ keeps decaying with time, while the regular

---

[4]In addition, time-dependence of $B(t)$ in the interval $t \in [0, t_{\max}]$ is much more accessible than that of OTOC $C(t)$, as their computation complexities scale as $O(t_{\max})$ and $O(t_{\max}^2)$, respectively.
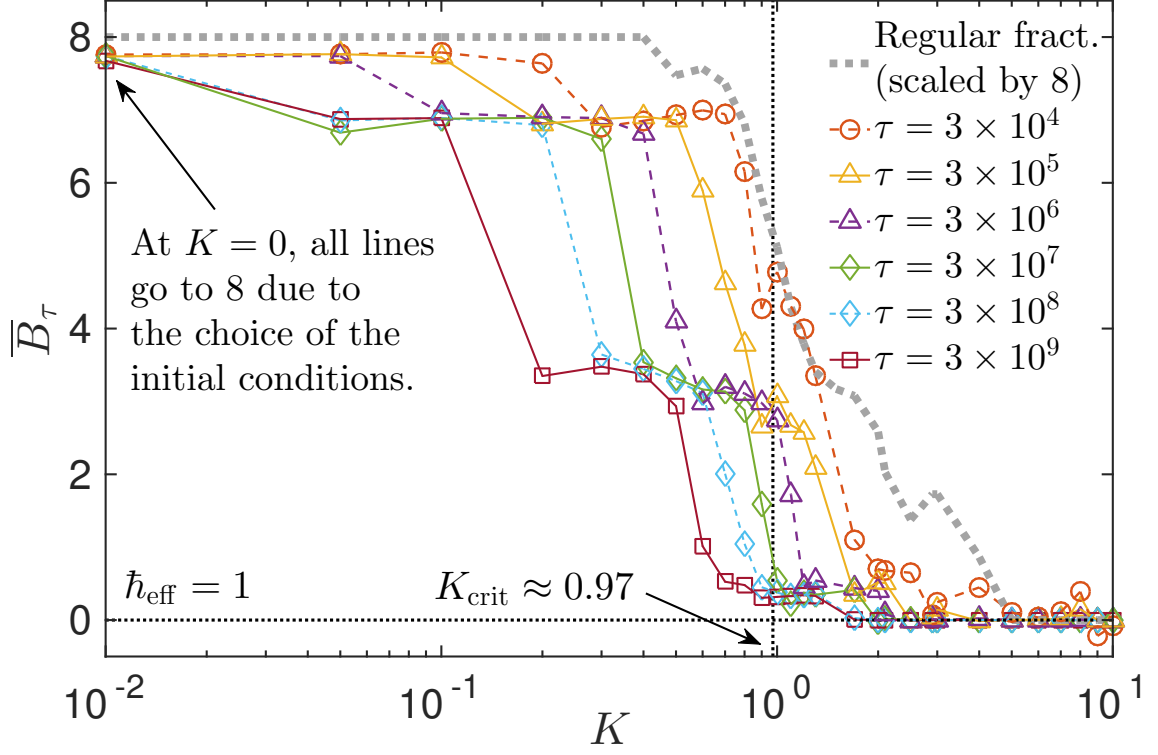
Figure 5.4: Long-time average $\overline{B}_\tau$ (5.7) (over various windows τ) of the two-point correlator $B(t)$ as a function of K compared to the regular fraction of the phase space weighted with the initial Wigner distribution $P(x,p)$ (scaled). The trend with increasing τ shows that at all $K \neq 0$, the correlations decay in time, but the rate of this decay has a step-like dependence on K. At $K > K_{cr}$, the decay is quite fast, while at $K < K_{cr}$, it takes $\overline{B}_\tau$ at least exponentially large window to vanish. It is not clear from the data whether at small $K \neq 0$, averaged correlator eventually goes to zero at $\tau \to \infty$ or is bounded from below. Initial state corresponding to $P(x,p)$ is the Gaussian (5.4) with $p_0 = 0$ and $\sigma = 4$.

phase-space fraction is a constant determined by the initial conditions and K, so a fixed window should be chosen for comparison. As the ratio of regular to chaotic areas of the phase space decreases, so does the average value of the correlator over a this window, until it reaches zero at large K, where almost no regular regions are present.
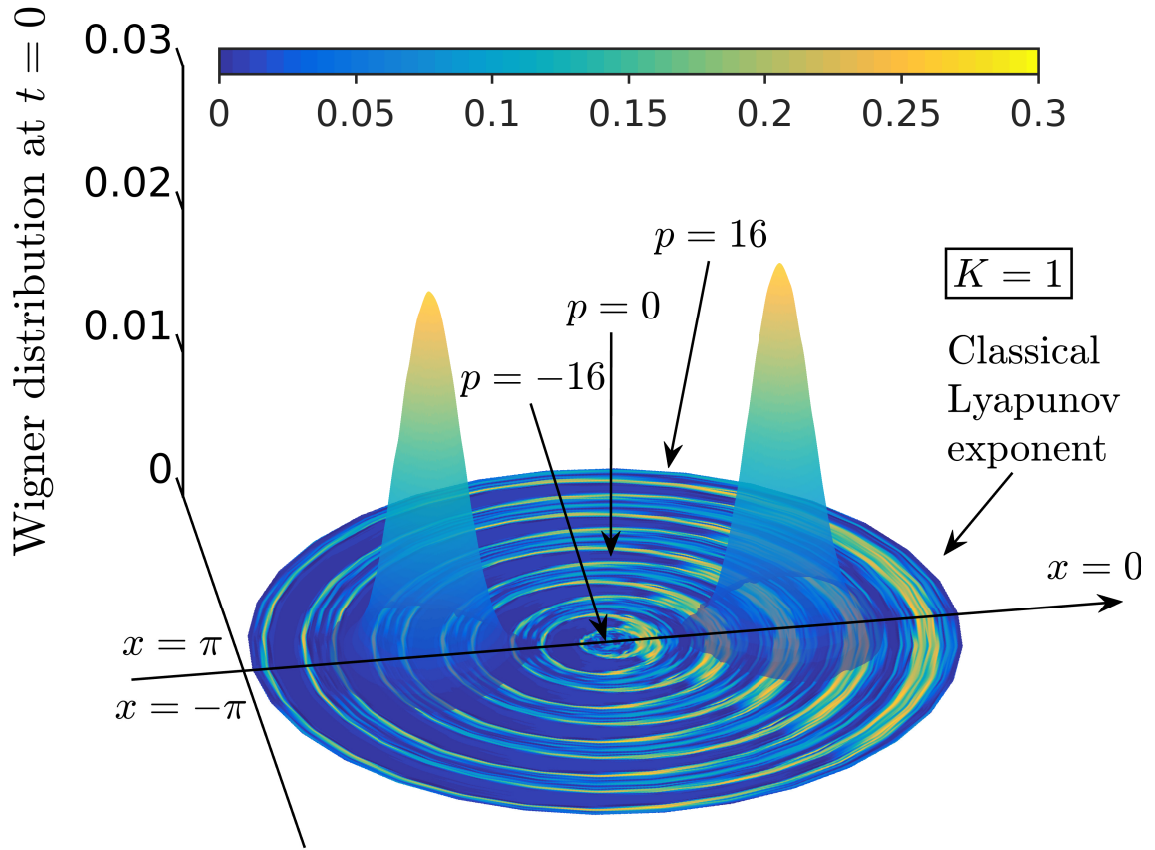
Figure 5.5: Initial Wigner distribution $P(x, p)$ (3D plot) on the top of the classical Lyapunov exponent (shown in color in the horizontal plane, see colorbar for numerical values). Initial state corresponding to $P(x, p)$ is the Gaussian (5.4) with $p_0 = 0$ and $\sigma = 4$. Lyapunov exponent is shown for $K = 1$.

5.5 Universal Scaling of OTOC beyond the Ehrenfest Time

Consider the out-of-time-ordered correlator (OTOC) given in Eq. (5.2):

$$C(t) = -\left\langle [\hat{p}(t), \hat{p}(0)]^2 \right\rangle. \tag{5.8}$$

Clearly, $C(0) = 0$, but $\forall t > 0 : C(t) > 0$. Therefore, without loss of generality, we can represent $C(t)$ as an exponential of another function $\tilde{\lambda}(t)$ at all positive times. Moreover, the functions $C(t)$ and $\tilde{\lambda}(t)$ can in general be functions of at most three variables: $C(t) = C(K, \hbar_{\text{eff}}, t)$ and $\tilde{\lambda} = \tilde{\lambda}(K, \hbar_{\text{eff}}, t)$, because K and $\hbar_{\text{eff}}$ are the only parameters of the model. So, we use the following general ansatz:

$$C(K, \hbar_{\text{eff}}, t) = C(K, \hbar_{\text{eff}}, 1) \exp\left[\tilde{\lambda}(K, \hbar_{\text{eff}}, t) \times (t - 1) \right]. \tag{5.9}$$

As we mentioned above, the corresponding classical model (the standard map) has only one parameter, K, and has a mixed regular-chaotic phase space. This system is described by the classical Hamilton's equations of motion at discrete times denoted as n for the kicked rotor Hamiltonian given in Eq. (5.1):

$$\begin{cases} p_{n+1} = p_n + K \sin x_n \\ \\ x_{n+1} \underset{\text{mod } 2\pi}{=} x_n + p_{n+1} \end{cases}. \tag{5.10}$$

Its global average Lyapunov exponent, $\lambda_{\text{cl}}(K)$, depends only on K (as the only parameter of the model), and at large $K \gtrsim 10$ behaves as $\lambda_{\text{cl}}(K) \approx \ln \dfrac{K}{2}$. The

same behavior as a function of K is expected from $\tilde{\lambda}(K, \hbar_{\mathrm{eff}}, t)$ in Eq. (5.9) at early times, $t < t_E$, where the Ehrenfest (or scrambling) time $t_E \approx \frac{1}{\lambda_{\mathrm{cl}}(K)} \ln \frac{K}{\hbar_{\mathrm{eff}}}$ [202]. And although quantitatively, there are differences between the conventionally defined classical Lyapunov exponent $\lambda_{\mathrm{cl}}(K)$ and the growth rate of the OTOC – CGR $\tilde{\lambda}(K, \hbar_{\mathrm{eff}}, t)$ [5], there is indeed no dependence of $\tilde{\lambda}$ on $\hbar_{\mathrm{eff}}$ and t as long as we restrict the consideration to $t < t_E$: $\tilde{\lambda}(K, \hbar_{\mathrm{eff}}, t) = \tilde{\lambda}(K)$. Upon plugging this into Eq. (5.9), we see that it means that the OTOC is characterized by pure exponential growth at early times with the exponent independent of $\hbar_{\mathrm{eff}}$.

Next, we lift the restriction of $t < t_E$ and consider the behavior of the OTOC at general times t. In this case, $\tilde{\lambda}$ picks up both the $\hbar_{\mathrm{eff}}$- and time-dependence. However, we make a conjecture that $\tilde{\lambda}(K, \hbar_{\mathrm{eff}}, t)$ depends on t and $\hbar_{\mathrm{eff}}$ only in a scaling combination $t/t_E(K, \hbar_{\mathrm{eff}})$, where we slightly adjust the definition of t_E by allowing a K-dependent constant in it to be fitted to the data. Specifically, we postulate that generally:

$$t_E(K, \hbar_{\mathrm{eff}}) = \frac{1}{\lambda_{\mathrm{cl}}(K)} \left[\ln \left(\hbar_{\mathrm{eff}}^{-1} \right) + c(K) \right], \qquad (5.11)$$

where $c(K)$ is a linear function of $\ln K$. [6] This conjecture, suggested first by Shmuel Fishman in 2019 [215], follows from the weak-localization-inspired intuition [202, 215] that the quantum interference that ceases the period of exponential growth

---

[5] As shown in Sec. 5.3 (Fig. 5.2), at $t < t_E$ we rather have $\tilde{\lambda}(K, \hbar_{\mathrm{eff}}, t) = \tilde{\lambda}(K) \approx \ln \frac{K}{\sqrt{2}}$.

[6] We also use a notation $t_E^0(K, \hbar_{\mathrm{eff}}) = \frac{\ln \left(\hbar_{\mathrm{eff}}^{-1} \right)}{\lambda_{\mathrm{cl}}(K)}$, which is the Ehrenfest time at $c(K) \equiv 0$.

should depend only on the number of times that the Planck-sized phase-space cells have "overlapped" with one another. At least for strongly chaotic systems, the latter should scale as t/t_E. As a result, $\tilde{\lambda} = \tilde{\lambda}\left(K, \dfrac{t}{t_E(K, \hbar_{\text{eff}})}\right)$ turns out to be only a function of two variables, not three. This leads to a universal scaling of the OTOC and, among other advantages, potentially allows one to uncover the practically inaccessible semi-classical limit by extending the simulations done in the intermediate-$\hbar_{\text{eff}}$ regime via the scaling law toward the $\hbar_{\text{eff}} \to 0$ limit.

The scaling can be written down in the following way:

$$\tilde{\lambda}(K, \hbar_{\text{eff}}, t) = \tilde{\lambda}\left(K, \ \frac{\tilde{t}}{\ln \hbar_{\text{eff}}^{-1} + c(K)}\right), \tag{5.12}$$

where time is measured in the units of the Lyapunov time $t_\lambda(K) = 1/\lambda_{\text{cl}}(K)$, i.e. $\tilde{t}(K) = t/t_\lambda(K) = \lambda_{\text{cl}}(K)\, t$. At $K \gtrsim 10$, we find $c(K) \approx 1.07 \ln K + 1.55$ (see Fig. 5.6). As mentioned above, the reason why it works is that the correlations are determined by how many times the phase space has been scrambled from the scale of the initial partitioning to the scale of the whole system. And the number of times it happened is determined by t/t_E.

In Figs. 5.7 – 5.10, we give four different examples of the data collapse that originates from the scaling in Eq. (5.12) for various values of K – both below and above the regular-to-chaotic transition in the standard map ($K_{\text{cr}} \approx 0.97$), that corresponds to the transition between the local and global chaos in the phase space. All the cases with $K > 10$ look exactly the same and follow the behavior shown in Fig. 5.7. The scaling data from multiple values of $K \geq 10$ is aggregated in Fig. 5.6.
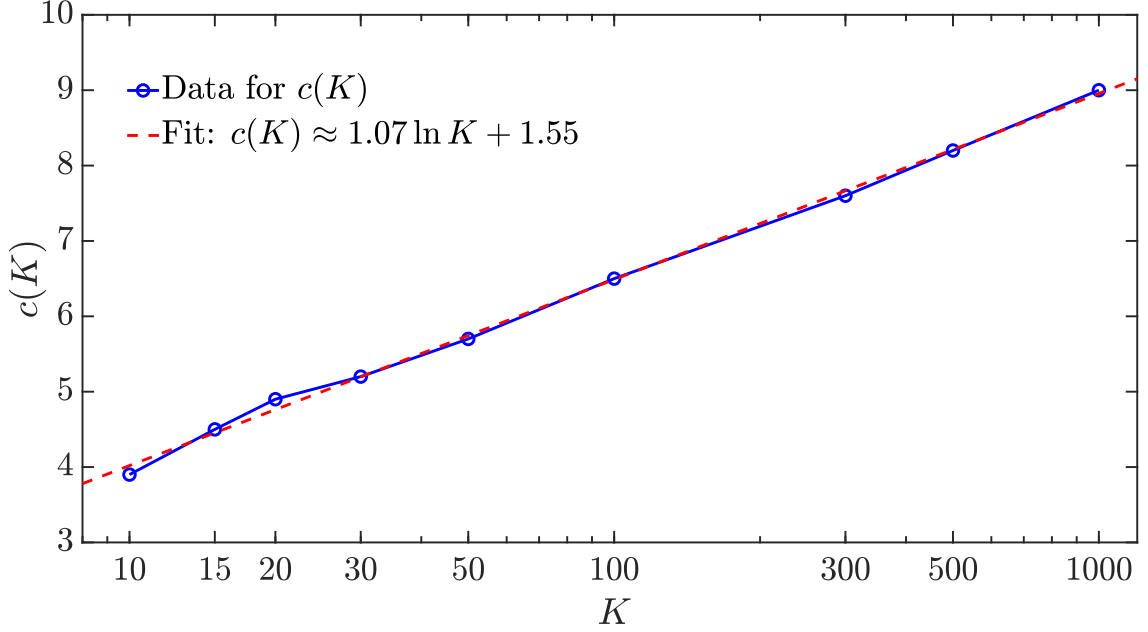
Figure 5.6: The dependence of the K-dependent term in the Ehrenfest time, $c(K)$, on the kicking strength K at $K \geq 10$ in the linear-logarithmic scale.

Below the transition, $K < K_{\mathrm{cr}}$, additional generalizations need to be made in order to establish the scaling.

Note that the data in Figs. 5.6 – 5.10 is generated for quantum kicked rotor (QKR), but the concept and conclusions may apply very generally to a wide variety of "quantum chaotic" systems.

Unfortunately, we do not know how universal this scaling function remains at longer times and weaker kicking strength. In the latter regime, it might require a more sophisticated ansatz for t_E. We also do not know how robust the scaling remains as $t/t_E \to \infty$ and whether the collapsed straight lines at $t > t_E$ in Figs. 5.7 – 5.10 are going to remain straight, parallel and collapsed at much longer times. It is likely that the scaling becomes exact for arbitrarily long times only in the strongly chaotic limit $K \to \infty$.
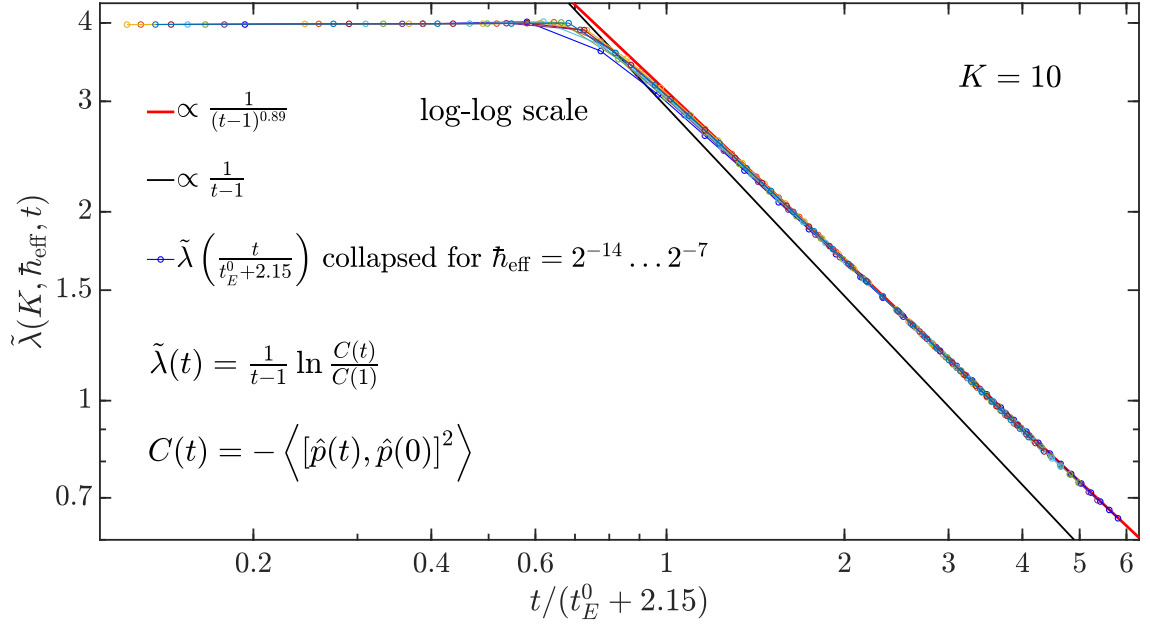
Figure 5.7: The function $\tilde{\lambda}$ from Eqs. (5.9) and (5.12) as a function of scaled time at $K = 10$ and $\hbar_{\text{eff}} = 2^{-14}$, 2^{-13}, 2^{-12}, 2^{-11}, 2^{-10}, 2^{-9}, 2^{-8}, and 2^{-7} in the double logarithmic scale. Relevant power-law functions are shown as eye guides.
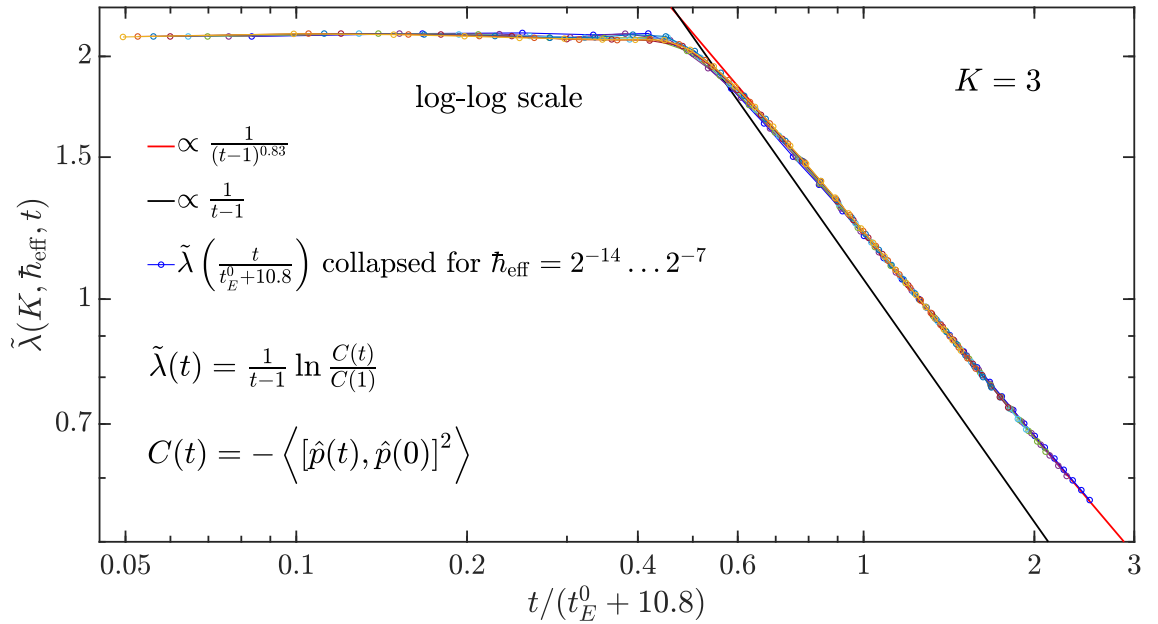
Figure 5.8: The function $\tilde{\lambda}$ from Eqs. (5.9) and (5.12) as a function of scaled time at $K = 3$ and $\hbar_{\text{eff}} = 2^{-14}$, 2^{-13}, 2^{-12}, 2^{-11}, 2^{-10}, 2^{-9}, 2^{-8}, and 2^{-7} in the double logarithmic scale. Relevant power-law functions are shown as eye guides.
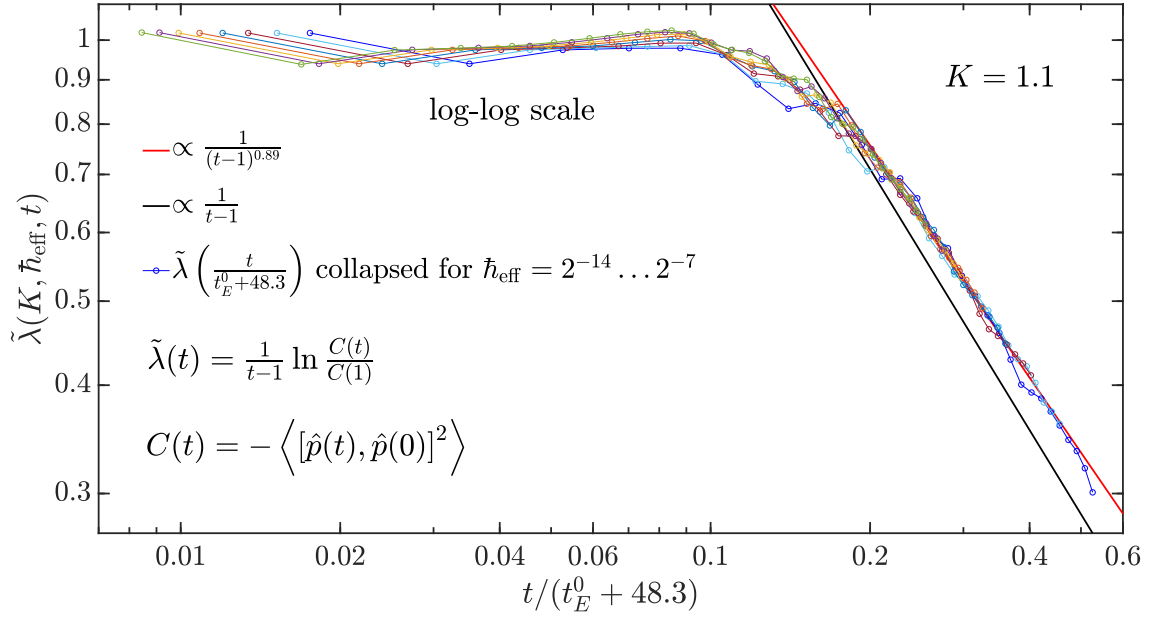
Figure 5.9: The function $\tilde{\lambda}$ from Eqs. (5.9) and (5.12) as a function of scaled time at $K = 1.1$ and $\hbar_{\text{eff}} = 2^{-14}$, 2^{-13}, 2^{-12}, 2^{-11}, 2^{-10}, 2^{-9}, 2^{-8}, and 2^{-7} in the double logarithmic scale. Relevant power-law functions are shown as eye guides.
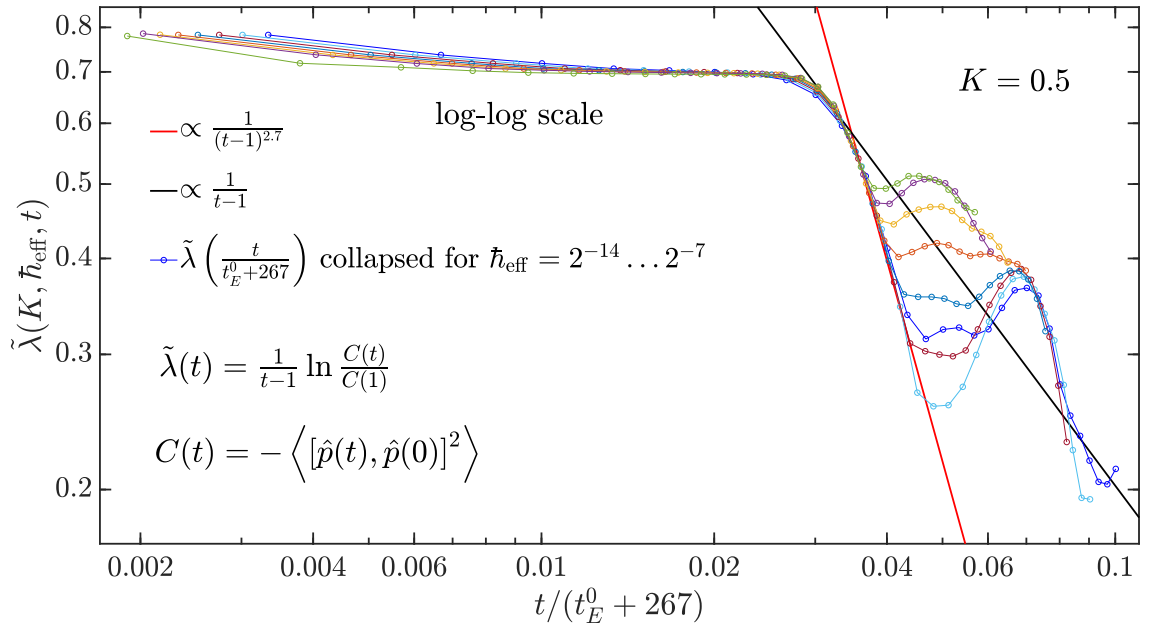
Figure 5.10: The function $\tilde{\lambda}$ from Eqs. (5.9) and (5.12) as a function of scaled time at $K = 0.5$ and $\hbar_{\text{eff}} = 2^{-14}$, 2^{-13}, 2^{-12}, 2^{-11}, 2^{-10}, 2^{-9}, 2^{-8}, and 2^{-7} in the double logarithmic scale. Relevant power-law functions are shown as eye guides.

5.6 Additional Materials

5.6.1 Classical Lyapunov exponent

Classical chaotic systems, such as KR, are characterized by Lyapunov exponents that determine the rate of exponential separation of initially close trajectories in the phase space. In one-dimensional systems, there is only one positive Lyapunov exponent, λ, given by the phase-space average of $\lambda(x, p)$:

$$d(t) \approx d(0)e^{\lambda(x,p)t}, \tag{5.13}$$

where $d(t) = \sqrt{[x'(t) - x(t)]^2 + [p'(t) - p(t)]^2}$ is the distance at time t between two initially close trajectories in the phase space. This can be used to extract λ as:

$$\lambda = \langle\!\langle \lambda(x, p) \rangle\!\rangle = \left\langle\!\!\!\left\langle \lim_{t \to \infty} \lim_{d(0) \to 0} \frac{1}{t} \ln \frac{d(t)}{d(0)} \right\rangle\!\!\!\right\rangle . \tag{5.14}$$

5.6.2 Chirikov's analytical derivation of formula (5.5) for Lyapunov exponent

Consider two trajectories that obey the standard map:

$$\begin{cases} p_{n+1} = p_n + K \sin x_n \\ \\ x_{n+1} \underset{\mathrm{mod}\ 2\pi}{=} x_n + p_{n+1} \end{cases}, \qquad (5.15)$$

$$\begin{cases} p'_{n+1} = p'_n + K \sin x'_n \\ \\ x'_{n+1} \underset{\mathrm{mod}\ 2\pi}{=} x'_n + p'_{n+1} \end{cases}. \qquad (5.16)$$

Let us introduce relative coordinates: $\xi_n = x'_n - x_n$ and $\eta_n = p'_n - p_n$, so that $\boldsymbol{d}(n) = \begin{pmatrix} \eta_n \\ \xi_n \end{pmatrix}$. Standard map results for them in:

$$\begin{cases} \eta_{n+1} = \eta_n + K(\sin x'_n - \sin x_n) \\ \\ \xi_{n+1} = \xi_n + \eta_{n+1} \end{cases}, \qquad (5.17)$$

where x_n and x'_n cannot be eliminated exactly. Using a trigonometric identity, we can rewrite:

$$\sin x'_n - \sin x_n = \sin(x_n + \xi_n) - \sin x_n$$

$$= \sin x_n(\cos \xi_n - 1) + \sin \xi_n \cos x_n. \qquad (5.18)$$

Consider a mapping tangent to that in Eq. (5.17). For that, assume ξ_n is small. Then, to the linear order in ξ_n, the expression in Eq. (5.18) is equal to $\xi_n \cos x_n$, so that the tangent mapping is:

$$
\begin{cases}
\eta_{n+1} = \eta_n + (K \cos x_n)\xi_n \\
\\
\xi_{n+1} = \xi_n + \eta_{n+1}
\end{cases}
. \tag{5.19}
$$

It still contains x_n determined by the standard map and thus non-linearly dependent on time, but there is a class of trajectories for which this mapping is linear: periodic trajectories with $x_n \equiv 0$ or π and $p_n \in 2\pi\mathbb{Z}$. For them, the standard mapping is trivial: $p_{n+1} = p_n$, $x_{n+1} = x_n$, and $k \equiv K \cos x_n \equiv \pm K$ (for $x_n \equiv 0$ or π, respectively). Consider the mapping (5.19) for trajectories near these special ones and rewrite it in the matrix form:

$$
\begin{pmatrix} \eta_{n+1} \\ \xi_{n+1} \end{pmatrix} = \begin{pmatrix} 1 & k \\ 1 & k+1 \end{pmatrix} \begin{pmatrix} \eta_n \\ \xi_n \end{pmatrix}. \tag{5.20}
$$

The length of $\boldsymbol{d}_n = \begin{pmatrix} \eta_n \\ \xi_n \end{pmatrix}$ is the distance between two trajectories in the phase space at step n. Denote eigenvalues of the matrix in Eq. (5.20) as $\ell_\pm$ and the corresponding eigenvectors as $\boldsymbol{e}_\pm$. Let us expand $\boldsymbol{d}_n = u_n \boldsymbol{e}_+ + v_n \boldsymbol{e}_-$. Then for the coefficients, we have: $u_{n+1} = \ell_+ u_n$, $v_{n+1} = \ell_- v_n$, so that $u_n = \ell_+^n u_0$, $v_n = \ell_-^n v_0$. Eigenvalues $\ell_\pm$ are:

$$
\ell_\pm = 1 + \frac{k}{2} \pm \sqrt{k\left(1 + \frac{k}{4}\right)}, \tag{5.21}
$$

so if $k \in [-4, 0]$, then $|\ell_+| = |\ell_-| = 1$, and the distance between the trajectories oscillates within some bounds. In the opposite case, when $k \notin [-4, 0]$, for positive k, $|\ell_+| > 1$ and $|\ell_-| < 1$, so we get $|u_n| \xrightarrow[n \to +\infty]{} \infty$, $|v_n| \xrightarrow[n \to +\infty]{} 0$ (and vice versa for negative $k < -4$ or $n \to -\infty$). In general, the eigenvalue $\ell_> : |\ell_>| > 1$ is given by:

$$\ell_> = 1 + \frac{k}{2} + \text{sgn}(k) \sqrt{k \left(1 + \frac{k}{4} \right)}. \tag{5.22}$$

For $k > 0$, the distance between trajectories:

$$d_n = |\boldsymbol{d}_n| \underset{n \to +\infty}{\approx} u_0 |\ell_+|^n = u_0 e^{n \ln |\ell_+|} = u_0 e^{\lambda(0,0)n}, \tag{5.23}$$

where $\lambda(0,0) = \ln |\ell_+|$ is the positive Lyapunov exponent at $x, p \underset{\text{mod } 2\pi}{=} 0$ (for $k < -4$, the positive Lyapunov exponent is $\lambda(\pi, 0) = \ln |\ell_-|$ and in general, it is given by $\ln |\ell_>|$).

Recall that map (5.20) only applies to the vicinities of the special points where $k = \pm K$. Let us now average this expression over the whole phase space substituting the general expression $k(x) = K \cos x$ and using $L(x) = |\ell_>[k(x)]|$. Then we arrive to:

$$\lambda \approx \left\langle\!\!\left\langle \lim_{t_c \to \infty} \frac{1}{2t_c} \sum_{n=1}^{t_c} \ln \frac{u_0^2 \ell_+^{2n} + v_0^2 \ell_-^{2n}}{u_0^2 \ell_+^{2n-2} + v_0^2 \ell_-^{2n-2}} \right\rangle\!\!\right\rangle, \tag{5.24}$$

which upon neglecting the vanishing negative-exponent terms turns into

$$\lambda \approx \left\langle\!\!\left\langle \ln |\ell_>[k(x)]| \right\rangle\!\!\right\rangle = \left\langle\!\!\left\langle \ln L(x) \right\rangle\!\!\right\rangle, \tag{5.25}$$

that is given explicitly in Eqs. (5, 6). At large K, everywhere except the vicinities of $\cos x = 0$, one has: $L(x) \approx |k(x)| = |K \cos x|$, which results in $\lambda \approx \ln(K/2)$.

We point out that the Chirikov's analytical derivation does not yield consistent results for the classical CGR.

5.6.3 Numerical calculation of Lyapunov exponent

The definition can be used directly to calculate LE. However, once chaotic islands become small, the finite initial separation between trajectories (due to numerical limitations) prevents from correct account for the contribution of chaotic trajectories. The tangent map introduced above allows to overcome this difficulty, because it is the derivative of the standard map. The calculation consists in propagating both standard map (5.15) and tangent map (5.19) using the values of x_n from standard map as inputs for tangent map. Starting at each initial point within some grid, we compute the expression:

$$\lambda(x_0, p_0) = \frac{1}{N} \sum_{t=1}^{N} \ln \frac{d(t)}{d(t-1)} \qquad (5.26)$$

for a sufficiently large N and then average it over the phase space. Each time when $\boldsymbol{d}(t)$ becomes large due to exponential stretching, we normalize it to unit length preserving its direction.

5.6.4 Classical CGR

This rate is extracted from the classical analogue of the quantum OTOC:

$$C_{\mathrm{cl}}(t) = \hbar_{\mathrm{eff}}^2 \left\langle\!\!\left\langle \left(\frac{\Delta p(t)}{\Delta x(0)} \right)^2 \right\rangle\!\!\right\rangle \sim e^{2\tilde{\lambda} t}. \tag{5.27}$$

Then

$$\tilde{\lambda} = \frac{1}{2} \ln \frac{C_{\mathrm{cl}}(t)}{C_{\mathrm{cl}}(t-1)} \tag{5.28}$$

Let us average it over some interval in time to improve our fitting accuracy (this step is not necessary though):

$$\tilde{\lambda} = \frac{1}{2(t_c - 1)} \sum_{t=2}^{t_c} \ln \frac{C_{\mathrm{cl}}(t)}{C_{\mathrm{cl}}(t-1)}. \tag{5.29}$$

Substituting here $C_{\mathrm{cl}}(t)$ from Eq. (5.27) and taking into account that $\Delta x(0)$ is constant throughout the phase space, we obtain:

$$\tilde{\lambda} = \frac{1}{2(t_c - 1)} \sum_{t=2}^{t_c} \ln \left[\frac{\langle\!\langle [\Delta p(t)]^2 \rangle\!\rangle}{\langle\!\langle [\Delta p(t-1)]^2 \rangle\!\rangle} \right], \tag{5.30}$$

which is calculated in the same way as the expression (5.26) using the tangent map. The limitation $t \le t_c$ comes from the fact that, as opposed to the case for LE – Eq. (5.26) – rescaling of $\boldsymbol{d}(t) = \begin{pmatrix} \Delta p(t) \\ \Delta x(t) \end{pmatrix}$ alters the expressions for CGR – Eq. (5.30) – and thus is not applicable.
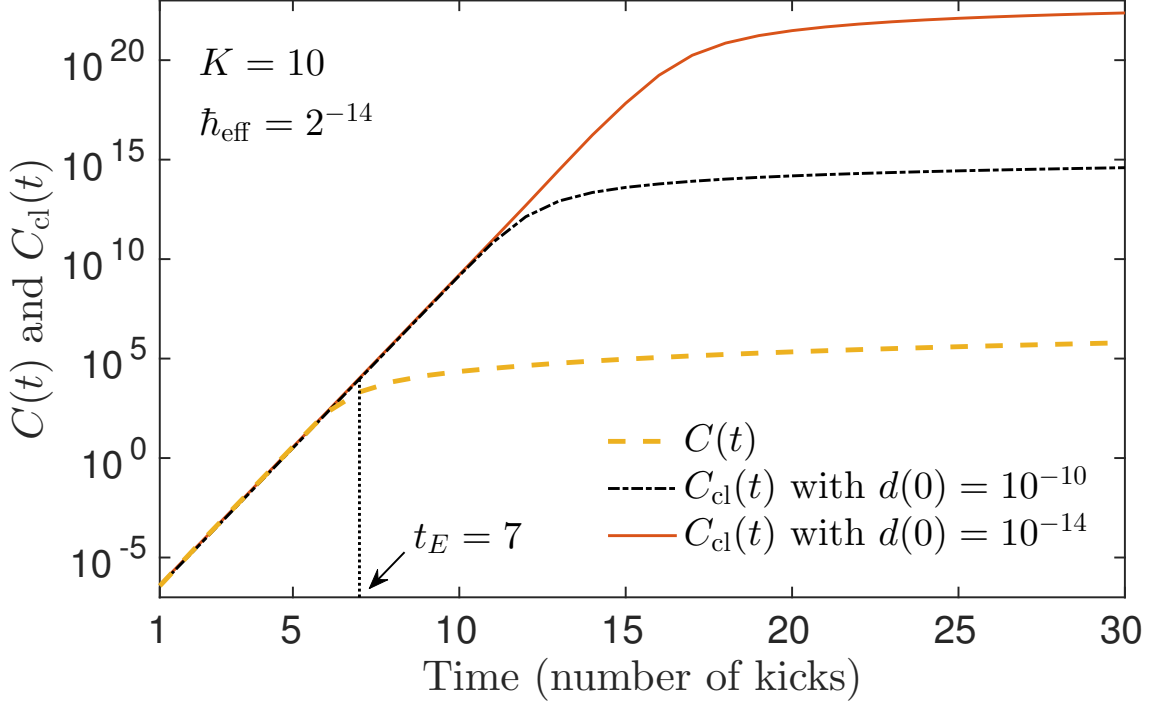
Figure 5.11: $C(t)$ and $C_{\mathrm{cl}}(t)$ in the semilog scale. The exponential growth of $C_{\mathrm{cl}}(t)$ saturates due to finite initial distance between trajectories as is shown by comparing $C_{\mathrm{cl}}(t)$ at $d(0) = 10^{-10}$ and $d(0) = 10^{-14}$. The exponential growth of $C(t)$, however, saturates due to the quantum interference effects that kick in at $t_E = 7$.

5.6.5 Classical $C_{\mathrm{cl}}(t)$ vs quantum $C(t)$

In this section, we demonstrate how these corresponding functions compare at large K. Fig. 5.11 shows the comparison at $K = 10$ (in logarithmic scale). Both $C(t)$ and $C_{\mathrm{cl}}(t)$ grow exponentially at early times and both slow down after some time. However, in case of $C_{\mathrm{cl}}(t)$ the reason is purely numerical – it is calculated by definition here, and the initial distance between the trial trajectories is finite. When the initial separation goes to zero, the exponential growth of $C_{\mathrm{cl}}(t)$ becomes infinite. On the contrary, the termination of the exponential growth of $C(t)$ is physical and occurs at $t_E = 7$, when quantum interference effects kick in.
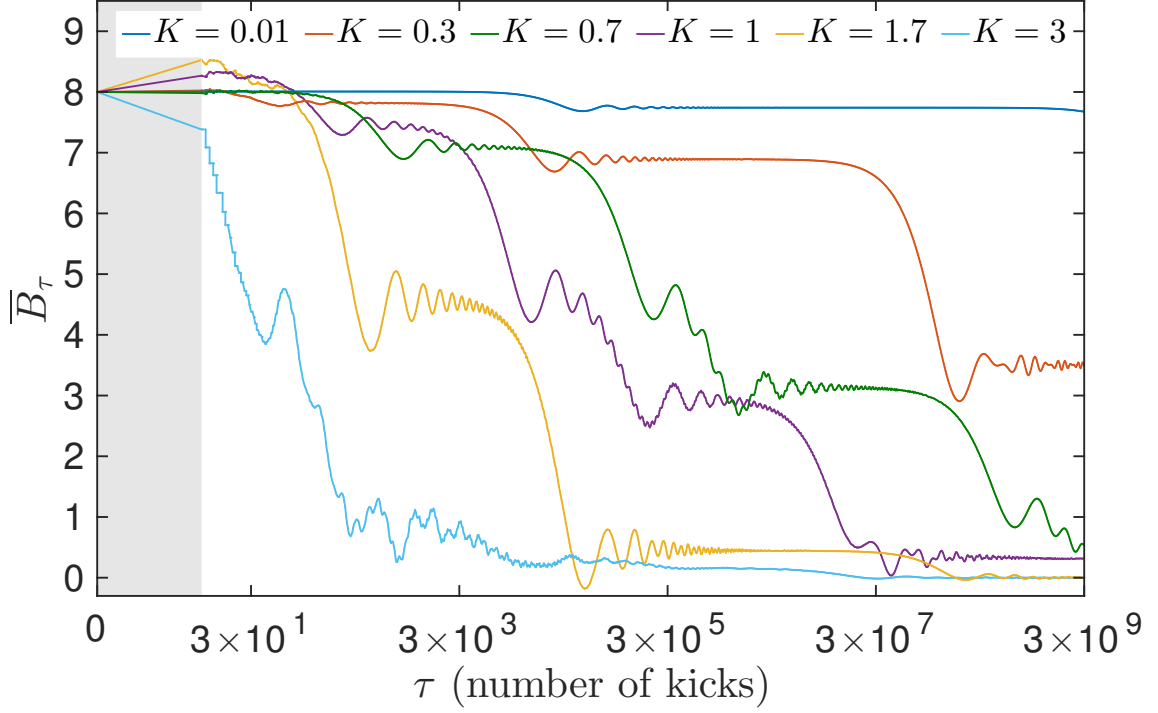
Figure 5.12: $\overline{B}_\tau$ as a function of τ in the lin-log scale at $K = 0.01$, 0.3, 0.7, 1, 1.7, and 3 (from the top to the bottom curve, respectively). The point $\tau = 0$ and the shaded interval $\tau \in (0; 10)$ are added manually to show the initial value corresponding to the wave-packet (4) with $p_0 = 0$ and $\sigma = 4$. At $K = 1.7$ and 3, one can see the complete relaxation to zero within the range of this plot.

5.6.6 Time-averaged two-point correlator as a function of averaging window size

Here, we show the dependence of the time-averaged two-point correlator $\overline{B}_\tau$ on the size τ of the averaging window at various K. In Fig. 5.12, one can see that the average correlations decay with time in steps, and the larger the kicking strength K is, the faster the correlations decay. Notice that the lin-log scale of the plot implies that the speed-up of this decay with K is exponential.

Chapter 6: Universal Level Statistics of the Out-of-Time-Ordered Operator

6.1 Introduction

There exist a number of approaches to define the concept of "quantum chaos." The basic approach is to quantize a classically chaotic model and declare the corresponding quantum model as "quantum chaotic." Another prevailing method identifies quantum chaos with level repulsion between energy levels, described by the universal Wigner-Dyson statistics. The connection between the two is established via the so-called Bohigas-Giannoni-Schmit (BGS) conjecture [29] (first formulated in Ref. [30]), which postulates that the spectra of time-reversal-invariant classically chaotic systems show the same fluctuation properties as predicted for Gaussian Orthogonal Ensemble (GOE) of random matrices. Semiclassical approaches in the form of periodic orbit theory [216] by Berry [217] and non-linear sigma models by Andreev *et al.* [218, 219, 220] have been employed to prove BGS conjecture with partial success. There are alternative approaches to quantum chaos: those based on wavefunction behavior, such as quantum ergodicity [221, 222, 223], Berry's random-wave conjecture [224], and nodal statistics [225]; criteria based on transport or scattering

properties [226, 227]; and definitions connecting to exponential behavior reminiscent of the classical instability, that is observed in quantum fidelity [207, 228], Loschmidt echo [211, 229], and out-of-time-ordered correlator (OTOC) [230] (see Chapter 5 for details on the latter one). More recently, the "definition" of quantum chaos based on OTOC became the focus of much research owing to its applicability to many-body quantum systems (see e.g. Refs. [27, 28, 195, 196, 197, 198, 199, 200, 231]). The quasiclassical limit of OTOC reproduces the sensitivity of quasiclassical trajectories to initial conditions. Exponential growth of OTOC at early times is identified as a fingerprint of quantum chaos, connecting the quantum dynamics to the hallmark of classical chaos – the Lyapunov divergence of classical trajectories, colloquially known as the "butterfly effect."

In many cases (e.g., disordered metals [192, 193, 232] and certain chaotic billiards) these approaches do appear equivalent, but there is no universal equivalence. For example, not all quantum models with Wigner-Dyson level statistics are required to have an "obvious" classical counterpart (e.g., Sachdev-Ye-Kitaev model [27, 31]) and not all classically chaotic dynamical systems acquire Wigner-Dyson level statistics upon quantization, such as systems that show localization. Moreover, quantum systems with merely mixing (non-chaotic) classical counterparts can obey Wigner-Dyson distribution even without classical exponential instabilities (see, e.g., Ref. [32]). Such cases are considered outside of the BGS characterization. This ambiguity makes the notion of quantum chaos somewhat poorly defined. It is highly desirable therefore to obtain a more straightforward way of connecting the different intuitive ideas and approaches to "quantum chaos," and we attempt to do

so in this work by introducing an operator, we dub the *Lyapunovian* [see Eq. (6.1) below], which, as we show, contains information about both the development of the universal level statistics resulting from quantum interference and classical Lyapunov exponents in a (semi)classical phase space. Our study is motivated by recent work on OTOCs [27, 28, 195, 196, 197, 198, 199, 200, 231], the concept originally introduced by Larkin and Ovchinnikov [26] in the context of disordered metals. It involves a quantum expectation value of the following positive-definite operator:

$$\hat{C}(t) \equiv \exp\left[2\,t\,\hat{\Lambda}(t)\right] = -\left[\hat{x}(t),\,\hat{p}_x(0)\right]^2, \tag{6.1}$$

where we chose a pair of operators $\hat{x}(t)$ and $\hat{p}_x(t)$ – the Heisenberg operators of a particle's $x-$coordinate and the corresponding component of its momentum. Both in the case of a dirty metal and a billiard, one can argue in the semiclassical limit that since $\hat{p}_x(0) = -i\hbar\frac{\partial}{\partial x(0)}$, the OTOC – the quantum expectation value of the operator $\hat{C}(t)$ in Eq. (6.1) – probes the sensitivity of quasiclassical trajectories to initial conditions: $C(t) = \langle\hat{C}(t)\rangle = \hbar^2\left\langle\left(\frac{\partial x(t)}{\partial x(0)}\right)^2\right\rangle$. Thus the classical Lyapunov-like growth is anticipated at early times, $C(t) \propto \exp(2\tilde{\lambda}t)$, where $\tilde{\lambda}$ is related to the classical Lyapunov exponent (see Sec. 6.6 for details).

However, whether the OTOC actually exponentially grows or not depends on the choice of a quantum state over which the expectation value is calculated. It also depends on the existence of a long enough time window within the Ehrenfest time scale $t < t_E$ (see Sec. 6.6), before the quantum interference washes out the classical growth, if any. In some sense, the search for exponential growth of OTOC

becomes the search for a quasiclassical description. In some cases, such as billiards or diffusive metals, the quasiclassical limit is obvious. In some others, such as the Sachdev-Ye-Kitaev model, the classical variables are "hidden" in the large-N limit [233, 234]. The dependence of the OTOC on the choice of a quantum state is a non-universal feature, and instead, motivated by Ref. [235], we focus on the random-matrix structure of the Lyapunovian – the Hermitian operator $\hat{\Lambda}(t)$ in Eq. (6.1). The Lyapunovian possesses a semiclassical interpretation which enables us to connect the spectral statistics with that of the matrix of classical finite-time Lyapunov exponents in different cells of the partitioned phase space [1].

The rest of the paper is organized as follows. In Sec. 6.2, we introduce the specific model we used in the calculations. In Sec. 6.3, we demonstrate the main results on the universal level statistics of the Lyapunov operators. Next, Sec. 6.4 elaborates on the dynamics of the time-dependent level statistics and the ways it can be observed. Sec. 6.5 gives a heuristic picture that helps in developing the intuition behind our findings. Finally, in Sec. 6.6, we show the early-time exponential growth of OTOC in our model and explain why it is not always readily visible.

6.2 Model

For explicit calculations, we choose the quantum stadium billiard – a canonical model to explore quantum signatures of chaos, – but the main construction naturally transplants to a wide class of models. The classical Bunimovich stadium

---

[1]Note the qualitative difference between the finite-time spectrum of the single-particle Lyapunovian and the spectrum of infinite-time Lyapunov exponents in multidimensional classical models [236, 237].
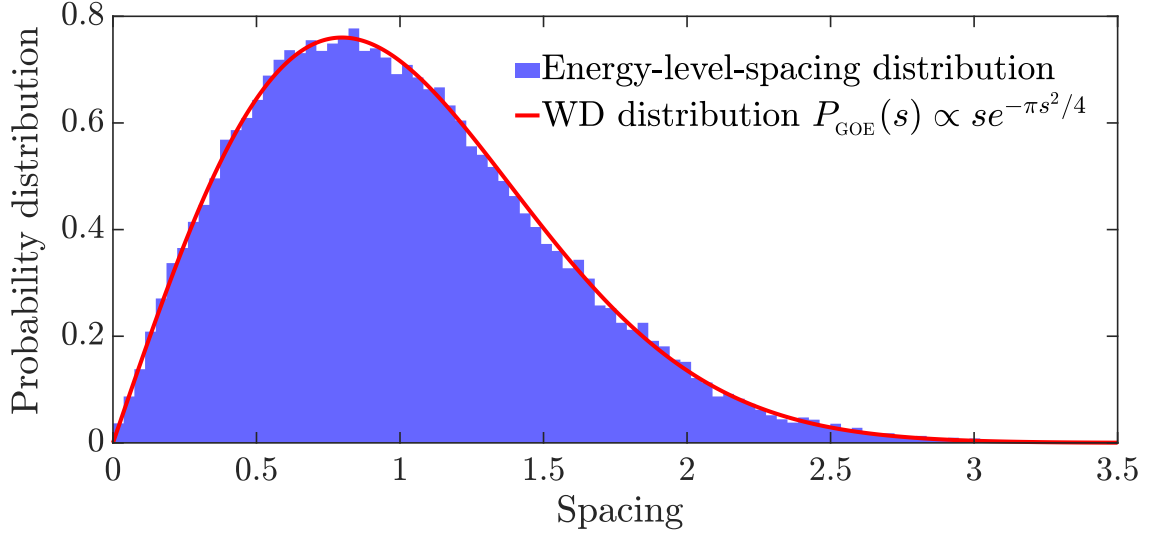
Figure 6.1: Energy-level statistics for quantum stadium billiard (separate for each eigenstate parity, combined). Contribution from the bouncing-ball modes [241, 242, 243] is removed within the spectrum unfolding. Solid line shows GOE Wigner-Dyson distribution.

billiard [33, 34, 35, 36, 37, 38, 39] is a seminal model of classical chaos, and its quantum counterpart has been known to obey the Wigner-Dyson energy-level statistics of GOE [29, 30, 238, 239, 240, 241] reproduced in Fig. 6.1 [2]. The oscillatory contribution of the bouncing-ball orbits [241, 242, 243] to the density of states – a non-generic feature of the stadium – is subtracted in order to obtain the near-perfect agreement between the level-spacing distribution and the Wigner surmise. Throughout the paper, we consider the billiard with unit aspect ratio $a/R = 1$, where $2a$ is the length of the straight segments of the walls and R is the radius of the circular ones. We use the units where both the area of the billiard $A = (\pi + 4)R^2$ and the particle mass m are set to 1. We also choose a certain momentum p_0 as the third unit. Later, it will play the role of the quantum-particle's average momentum. In the semiclassical

[2]Due to the reflection symmetries, the Hamiltonian can be written as a 4×4 block-diagonal matrix in a basis of functions with definite parities. As a result, there is no correlation (and thus no repulsion) between the eigenvalues of different blocks. More details are given after Eq. (6.2).

limit, p_0 translates into the momentum of the classical particle inside the billiard. In these units, the Schrödinger equation and the boundary condition read:

$$-\frac{\hbar_{\text{eff}}^2}{2}\nabla^2\Psi(x,y) = E\Psi(x,y), \quad \Psi(\mathbf{r})\Big|_{\mathbf{r}\in\text{billard walls}} \equiv 0, \tag{6.2}$$

where $\hbar_{\text{eff}} = \hbar/(p_0\sqrt{A})$. The stadium billiard has two reflection symmetries: $x \leftrightarrow -x$ and $y \leftrightarrow -y$. Correspondingly, its eigenstates have one of four possible parities [238]. E.g., the odd-odd-parity functions $\Psi_{\text{oo}}(-x,y) \equiv \Psi_{\text{oo}}(x,-y) \equiv -\Psi_{\text{oo}}(x,y)$. As it is usually done, in order to enforce these parities and speed up the calculations, we use a quarter of the billiard imposing Dirichlet and/or Neumann boundary conditions on the cuts to obtain solutions of all four parities separately. We solve these boundary-value problems for the Laplace operator numerically using the finite-element method. It is known that the accuracy of the numerical solution deteriorates with the number of found eigenstates [244]. We use the Weyl's formula for the number of modes [182] to control it. According to the Weyl's law, the average number of eigenstates below energy E asymptotes to:

$$\mathcal{N}(E) \simeq \frac{A}{4\pi}\frac{2}{\hbar_{\text{eff}}^2}E - \frac{P}{4\pi}\sqrt{\frac{2}{\hbar_{\text{eff}}^2}E}, \quad E \to \infty, \tag{6.3}$$

where P is the billiard's perimeter. We do all calculations in several ranges. The smallest range is limited to about $N = 5000$ eigenstates and preserves almost exact agreement with the Weyl's formula, and the largest one is over $N = 10^5$ states. We verify that our results do not depend on the truncation size N. In addition, we

benchmark our solutions against those we obtain independently via the boundary-integral method, and reach the same level of accuracy with both approaches. We should note that the absolute error in the number of the found energy levels (as compared to the Weyl's formula) grows quadratically with energy for the levels E_n, $n \gtrsim 2000$ with a very small prefactor. However, while the overall magnitude of the energy starts to overestimate the Weyl's expression – the inverse of Eq. (6.3) – after this point, the structure of the spectrum is preserved. This is verified by varying the algorithm's accuracy, comparing the results to those obtained via the boundary-integral method, and subtracting the smooth quadratic function that brings the spectra obtained by all methods on top of each other. In the tests we performed, our results for the distributions did not show any influence of this deviation as it is completely canceled by the spectrum unfolding anyway.

6.3   Universal statistics of the Lyapunovian

Let us turn to the central subject of the work – the level statistics of the out-of-time-ordered operators. Apart from the Lyapunovian [Eq. (6.1)], we also define the Hermitian operators:

$$\hat{C}^{(k)}(t) = (-i)^k \left[\hat{x}(t), \hat{p}_x(0)\right]^k \overset{+}{=} \exp\left[k\, t\, \hat{\Lambda}_k(t)\right], \tag{6.4}$$

with $k \in \mathbb{N}$, such that $\hat{C}^{(2)}(t) \equiv \hat{C}(t)$. For even $k = 2n$, $\hat{\Lambda}_{2n}(t) \equiv \hat{\Lambda}(t)$, while for odd $k = 2n - 1$, we only define $\hat{\Lambda}_{2n-1}(t)$ within the positive-eigenvalue subspaces of $\hat{C}_{2n-1}(t)$, which is indicated by the "$\overset{+}{=}$" sign. In addition, we consider a closely

109

related Hermitian operator that defines a 4-point-correlator part of OTOC:

$$\hat{F}(t) = \hat{x}(t)\hat{p}_x(0)\hat{x}(t)\hat{p}_x(0) + \text{H. c.} \overset{+}{=} \exp\left[\hat{\Gamma}(t)\right]. \qquad (6.5)$$

We use the energy eigenstates $|E_n\rangle$ to construct matrices $C_{nm}^{(k)}(t) = \langle E_n|\hat{C}^{(k)}(t)|E_m\rangle$ and $F_{nm}(t) = \langle E_n|\hat{F}(t)|E_m\rangle$. For numerical calculations, we truncate the operators to finite $N \times N$ matrices according to the number of the eigenstates in use. Then the finite matrices are numerically diagonalized and the statistics of the spacings between the logarithms of eigenvalues as well as between the eigenvalues themselves are studied. Due to the definite parities of the energy eigenfunctions, the matrices $C_{nm}^{(k)}(t)$ and $F_{nm}(t)$ are 4×4 block-diagonal, and each block corresponds to one parity. Level spacings are thus only calculated within each block separately (because eigenvalues in different blocks are not correlated with each other), and then these four sets of the spacings are combined for statistical analysis. The operators $\hat{C}^{(k)}$ and $\hat{F}$ have the same bulk level statistics as their respective logarithms, $\hat{\Lambda}_k$ and $\hat{\Gamma}$ [3]. Therefore, we only show the results for the logarithmic operators. We observe different ensembles for different operators.

Note that at $t = 0$, $\hat{C}^{(k)}(0) = \hbar_{\text{eff}}^k$ are c-numbers, so they do not have level-spacing distributions. However, the operator $\hat{F}(0) = \hat{x}(0)\hat{p}_x(0)\hat{x}(0)\hat{p}_x(0) + \text{H. c.}$ is a non-trivial Hermitian operator, and its matrix $F_{nm}(0)$ is real-valued. We find

---

[3] As opposed to the Hamiltonian, these matrices do not belong to Gaussian ensembles. In Ref. [245], it is shown that for Wishart-ensemble matrices that have the form $M^\dagger M$ with rectangular matrix M from one of the Gaussian ensembles, the eigenvalue statistics of the bulk of the spectrum is still very well described by the universal Wigner-Dyson distributions. For operators that we consider, this appears to hold as well.
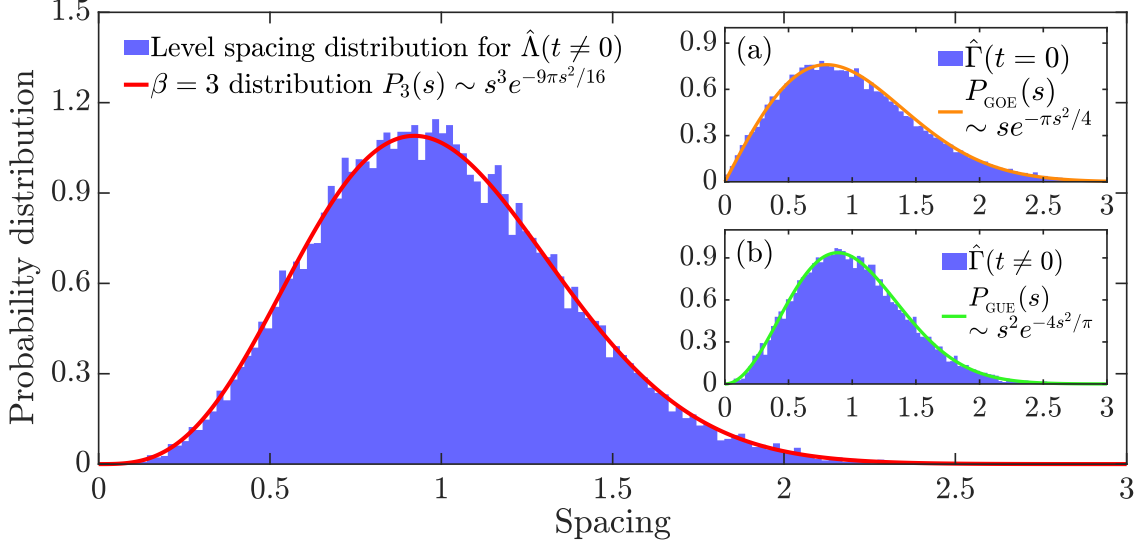
Figure 6.2: Eigenvalue-spacing distribution for the bulk of the Lyapunovian spectrum for every second state (within each parity block, combined). The total number of levels is 10^5. Insets: (a) bulk level spacing distribution for $\hat{\Gamma}(t = 0)$; (b) the same for $\hat{\Gamma}(t \neq 0)$. Solid lines show the corresponding Wigner-Dyson distributions.

– see inset (a) in Fig. 6.2 – that the bulk level statistics for $\hat{\Gamma}(0)$ [and for $\hat{F}(0)$] corresponds to GOE – the same ensemble as that of the Hamiltonian. The reason for this can be understood by representing the momentum operator as $\hat{p}_x = \frac{i}{\hbar_{\text{eff}}}[\hat{H}, \hat{x}]$, where $\hat{H} = \frac{\hat{p}_x^2 + \hat{p}_y^2}{2} + V_{\text{walls}}(\hat{x}, \hat{y})$ is the Hamiltonian of the billiard. Then $\hat{F}(0) = -\hbar_{\text{eff}}^{-2} \left(\hat{x} [\hat{H}, \hat{x}] \right)^2 + \text{H.c.}$

At any finite time, $t \neq 0$, all $C_{nm}^{(k)}(t)$ and $F_{nm}(t)$ become non-trivial Hermitian matrices with complex entries due to the unitary evolution of the operator $\hat{x}(t) = e^{i\hat{H}t}\hat{x}e^{-i\hat{H}t}$ with the random-matrix-like Hamiltonian. In Fig. 6.2, main plot and inset (b) show the bulk level statistics of the Lyapunovian and $\hat{\Gamma}(t)$, respectively, at a fixed time $t \neq 0$. Of course, microscopic details of both spectra are different and time-dependent, as the individual eigenvalues move with time. But we find that their bulk spectral statistics appear to be completely universal and remain the same for any $t \neq 0$. We should stress that for the operators defined this way in

111

the entire Hilbert space, there is no notion of short time (such as the collision or Ehrenfest times), so all times are equivalent, indeed. On the other hand, as shown in Sec. 6.4, one can observe dynamical evolution of the spectral properties of these operators when they are projected to a sub-space of the Hilbert space that consists of initially non-overlapping classical-like states only. In this case, after these classical-like states "dissolve" in the semiclassical phase space as the time reaches and exceeds t_E, the statistics tends to develop from the initial uncorrelated Poisson-like one to the Wigner-Dyson statistics – similar to that shown for the operators in the entire Hilbert space in Fig. 6.2.

The bulk level statistics of $\hat{\Lambda}_{2n-1}$ and $\hat{\Gamma}$ correspond to GUE [Fig. 6.2, inset (b)], while extracting level statistics of the Lyapunovian [the operators $\hat{\Lambda} \equiv \hat{\Lambda}_{2n}$ and $\hat{C}^{(2n)}$] requires one more step. The bulk level statistics of $\hat{C}^{(1)}$ and $\hat{\Lambda}_1$ correspond to GUE. But since the spectrum of $\hat{C}^{(1)}$ has positive and negative branches, and $\hat{C} \equiv \left[\hat{C}^{(1)} \right]^2$, the spectrum of $\hat{C}$ consists of these positive and negative branches squared and superimposed onto each other (this translates to the spectrum of the operator $\hat{\Lambda}$, as well). This results in the effective suppression of level repulsion, because the neighboring levels that originate from different branches of the spectrum of $\hat{C}^{(1)}$ have no short-range correlation. We present two ways to account for this effect. First, provided the knowledge of the spectrum of $\hat{C}^{(1)}$, one can filter the eigenvalues of $\hat{C}$ that originate from only one – positive or negative – branch. This results in the GUE filtered bulk level statistics for $\hat{C}$ and the Lyapunovian. Alternatively, without the knowledge of the spectrum of $\hat{C}^{(1)}$, but given that it is approximately evenly distributed around zero (the matrix tends to be traceless as its size is increased), one

112

can filter every second eigenvalue of $\hat{C}$ to greatly reduce the fraction of uncorrelated neighboring eigenstates. Following this approach, for every second level in the bulk of the spectra of $\hat{C}$ and $\hat{\Lambda}$, one finds the Wigner-Dyson distribution that corresponds to the Gaussian ensemble with the Dyson index $\beta = 3$ – intermediate between GUE and GSE [Fig. 6.2, main plot].

While the former (GUE) result is natural, the $\beta = 3$ ensemble for every second level of the Lyapunovian results from the combination of the operator's intrinsic structure and the filtering algorithm. However, it is still general – the same statistical properties can be found for next-nearest-neighbor level spacing in the bulk of the spectra of positive-definite matrices of the form M^2 (or $\ln M^2$), where M is an Hermitian random matrix drawn from GUE. This argument suggests that for all odd powers $2n - 1$, the bulk level statistics of $\hat{C}^{(2n-1)}(t \neq 0)$ should correspond to GUE, and for all even powers $2n$, the bulk level statistics for every second level of $\hat{C}^{(2n)}(t \neq 0)$ should correspond to the Gaussian ensemble with $\beta = 3$. We have verified that it is indeed the case for $k = 1, 2, 3,$ and 4.

We stress that in integrable models, the spectral structure of the Lyapunovian-type operators is drastically different from that in the non-integrable ones. There are multiple degeneracies in the Lyapunov-operator spectra in the integrable case, and the corresponding level-spacing distributions of the operators $\hat{\Lambda}_1$ and $\hat{\Lambda}$ are thus very tightly peaked around zero and are generally not even well defined, because the unfolding procedure cannot be performed. We checked it specifically for a circular billiard, a rectangular billiard, and for a 1D particle-in-a-box model (semi-analytically). In all these cases, the level repulsion is absent, and most of the

Lyapunovian eigenstates are (quasi)degenerate. So, one can readily distinguish such systems from the chaotic ones.

6.4 Time-dependent level statistics

We now turn to the particularly interesting question of connection between the exponential Lyapunov growth of the OTOC, $C(t) = \langle \Psi | e^{2t\hat{\Lambda}(t)} | \Psi \rangle \propto e^{2\tilde{\lambda}t}$, at early times and the Wigner-Dyson level statistics of the operator $\hat{\Lambda}(t)$. There appears to be a disconnect between the two: the former – the Lyapunov growth – is an early-time ($t < t_E$) classical behavior in the absence of quantum interference, while the latter is a consequence of well-developed quantum interference. We begin with a schematic demonstration of the mechanism of the correlation buildup between initially almost uncorrelated classical-like states. It also translates to the correlation build-up between the phase-space cells discussed in the next section. We start by projecting the operator $\hat{C}^{(1)}(t)$ onto an ensemble of 20 subspaces of the Hilbert space to form an ensemble of 20 projected operators (to improve statistics). Every subspace is composed of 8 almost non-overlapping minimal-uncertainty wave packets, each has unit average momentum. Note that although *all* possible coherent states form an over-complete basis, we do not have to project operators onto all of them and, instead, have to take a subset that consists of states which form an (almost) orthonormal basis in the corresponding subspace. Our subsets that satisfy these requirements are small due to numerical limitations, but in principle, can be arbitrary large, given small enough $\hbar_{\text{eff}}$. Letting these states evolve in time,

we calculate eigenvalue-spacing distribution for the projected operators at different times (excluding the smallest and the largest eigenvalues). Then we average these distributions over the ensemble of projected operators and, for better statistics, over time in two intervals: short times (between $10^{-3}t_E$ and $t_E/2$) and long times (between $2t_E$ and $200t_E$). After unfolding, we obtain distributions that roughly show the conversion from the uncorrelated – Fig. 6.3 (a) – to the correlated – Fig. 6.3 (b) – state of the phase space. The quality of the distribution is very limited by the small number of non-overlapping classical-like states that we fit into the billiard, but the principle can be observed.

6.5 Phase-space description of OTOC

We study two related phenomena: {1} the exponential growth of OTOC at early times (to be discussed in Sec. 6.6) and {2} the transition in the level statistics of "the projected Lyapunovian" from the Poisson to the Wigner-Dyson distribution. Here "the projected Lyapunovian" is a shorthand referral to a projection of the Lyapunov operator to a subspace of virtually non-overlapping classical-like states, as discussed above. To develop further intuition about the connection between {1} and {2}, we follow Cotler *et al.* [246] and consider the Lyapunov operator within the phase-space formulation. This is achieved by describing the quantum dynamics in terms of the Wigner function, $W(\mathbf{r}, \mathbf{p}, t)$, in the four-dimensional phase space that we parameterize by $z = (\mathbf{r}, \mathbf{p})$ for brevity. All operators are translated into phase-space distributions via the Wigner transform [247].
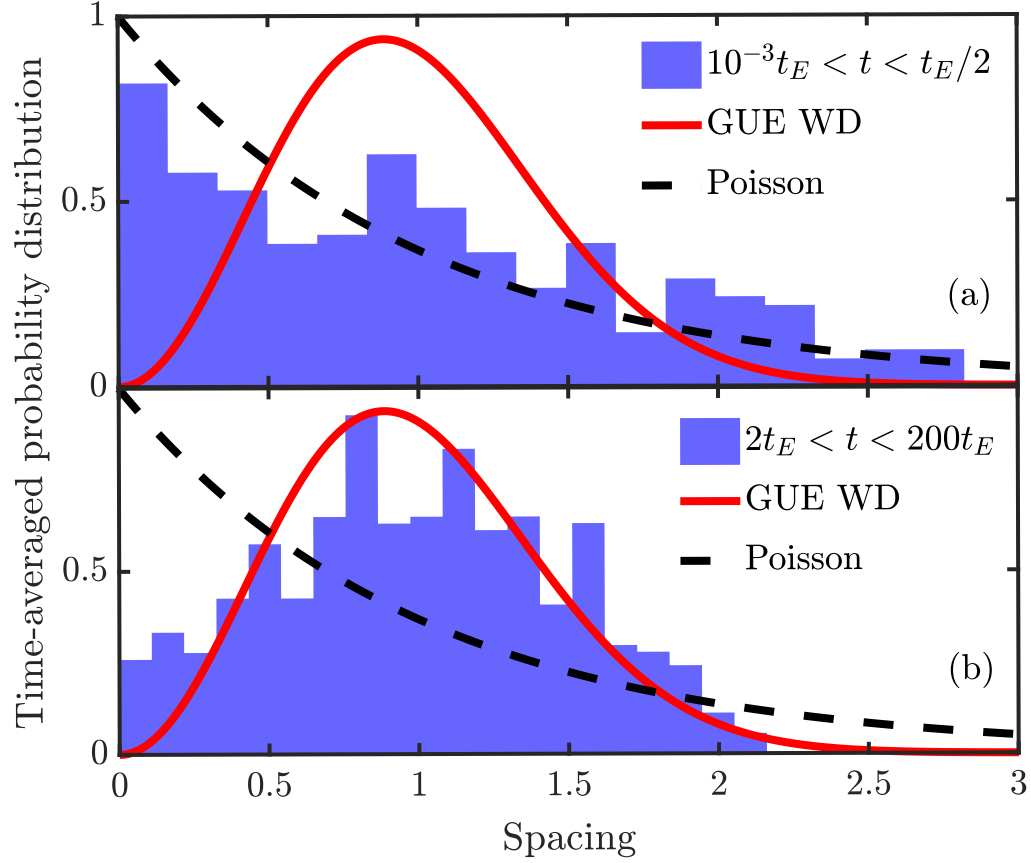
Figure 6.3: Eigenvalue-spacing distribution for the bulk of the spectra of an ensemble of projections of $\hat{C}^{(1)}(t)$ onto the coherent-state subspaces averaged over that ensemble and over time in two ranges of time: (a) at $t < t_E$, the distribution shows clear signatures of the Poisson component related to the uncorrelated nature of the phase space; (b) at $t > t_E$, the statistics tends to the universal GUE Wigner-Dyson distribution as phase-space correlations build up. With larger matrices, one can see that it becomes exact, such as the one shown in Fig. 2(b) in the main text. The low quality of the histograms is related to the small size of the subspaces (8×8 matrices).

In particular, the out-of-time-ordered operator $\hat{C}(t)$ corresponds to the Moyal brackets:

$$C_{\text{MB}}(z,t) = -[\![X(z,t), P(z,0)]\!]^2, \tag{6.6}$$

where we can choose $P(z,0) = p_{\text{cl}}(z,0)$ to be classical, and $X(z,t)$ is the solution of the Moyal evolution equation: $\dot{X}(z,t) = [\![H(z), X(z,t)]\!]$, where we also choose a classical initial condition $X(z,0) = x_{\text{cl}}(z,0)$. These choices correspond to the projection we introduced in the previous section. We can then express

$$X(z,t) = x_{\text{cl}}(z,t) + \sum_{k=1}^{\infty} \hbar_{\text{eff}}^{2k} x^{(2k)}(z,t), \tag{6.7}$$

and the series of quantum corrections vanishes at $t = 0$ according to the initial conditions: $x^{(2k)}(z,0) = 0$. This choice of initial conditions ensures that $X(z,t)$ is the Moyal trajectory which coincides with the classical trajectory $x_{\text{cl}}(z,t)$ in the $\hbar_{\text{eff}} \to 0$ limit. The classical trajectories are obtained by solving the Hamilton-Jacobi equation. The $\hbar_{\text{eff}}$-dependent corrections are obtained by solving the series of the following evolution equations:

$$\dot{x}^{(2n)}(z,t) = \sum_{k=0}^{n} [\![H(z), x^{(2k)}(z,t)]\!]_{2(n-k)}, \tag{6.8}$$

where the indexed brackets are defined as

$$[\![A, B]\!]_{2n} \equiv \frac{A(z) \left(\overleftarrow{\partial}_{\mathbf{r}} \overrightarrow{\partial}_{\mathbf{p}} - \overleftarrow{\partial}_{\mathbf{p}} \overrightarrow{\partial}_{\mathbf{r}} \right)^{2n+1} B(z)}{(2n+1)! \, (-4)^n}. \tag{6.9}$$

The initial conditions for the higher-order corrections are $x^{(2k)}(z, 0) = 0$ for all $k > 0$, since at time $t = 0$ all distributions are classical and are captured within the Poisson-bracket term of the evolution equation.

In this semiclassical approach, the classical phase space can be thought of as partitioned into the cells with the phase volume $\delta z = (2\pi\hbar_{\text{eff}})^2$. Within the phase-space formulation, the Lyapunov operator is represented via a matrix whose indices enumerate these cells. The elements of this matrix are functions supported only within one cell. The $\hbar_{\text{eff}}$-expansion of the corresponding evolution shows that the zeroth-order Larkin-Ovchinnikov classical term, $[\partial x_{\text{cl}}(z, t)/\partial x(z, 0)]^2 \propto e^{2\lambda(z)t}$, leads to independent Lyapunov exponents for each cell [Fig. 6.4(a)]. In other words, the Lyapunov operator in the classical limit is a matrix of uncorrelated Lyapunov exponents. A typical correlation term comes from an expression of the type $\hbar_{\text{eff}}^2 \left[\partial x^{(2)}(z, t)/\partial x(z, 0)\right] [\partial x_{\text{cl}}(z, t)/\partial x(z, 0)]$, which is the $\hbar_{\text{eff}}^2$-order correction to the trajectory [246]. The $\hbar_{\text{eff}}^2$-dependent corrections to $C_{\text{MB}}(z, t)$ generate correlations between the cells, and repulsion between the eigenvalues of the Lyapunov matrix "commences" [Fig. 6.4(b)]. Such correlations fully develop around the Ehrenfest time when the phase space becomes highly correlated [248] leading to the breakdown of the Moyal expansion – or any semiclassical description of OTOC [26] [Fig. 6.4(c)]. The full quantum operators such as $\hat{C}(t)$ generally correspond to late times $(t > t_E)$ in this picture, since they encapsulate full quantum interference effects resulting in the universal Wigner-Dyson statistics as shown in Fig. 6.2. However, as shown in Sec. 6.4, when projected to a subspace of initially classical-like states, these operators demonstrate the statistics change across the Ehrenfest time from the Poisson-
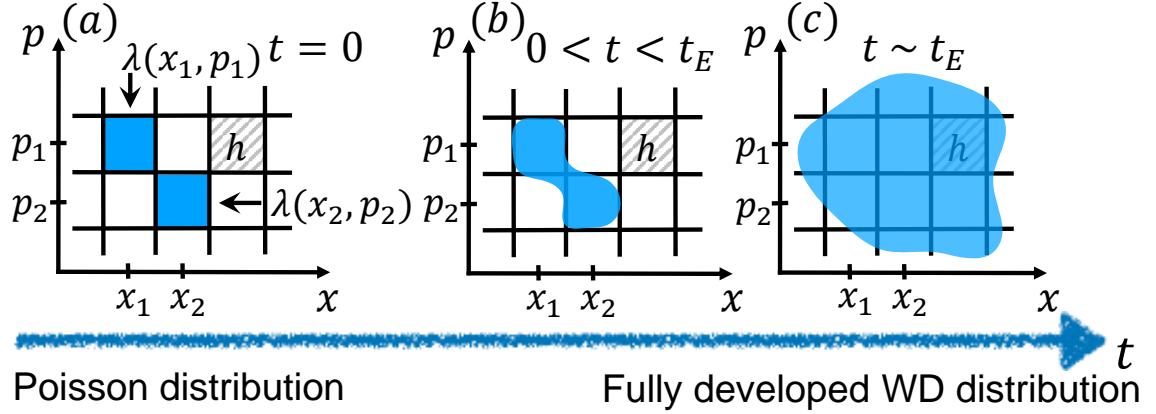
Figure 6.4: Schematics of the correlation development in phase space with time if initial states are semiclassical. (a) At times $t \ll t_E$, the local finite-time Lyapunov exponents are independent in different cells. (b) As time goes towards t_E, the correlations build up. (c) Around t_E, the phase-space becomes fully correlated, as shown by the distributions in Fig. 6.2.

dominated distribution to the Wigner-Dyson one.

6.6   Early-time behavior of OTOC

Finally, we address the question of how to actually extract the classical Lyapunov exponent from the Lyapunov operator in a way similar to that in Chapter 5 [230]. As noted above, not any matrix element would result in the exponential growth. For example, Hashimoto *et al.* [249] reported lack of exponential growth in the thermal average of the out-of-time-ordered operator – defined as $\text{OTOC}_\beta(t) = Z^{-1} \sum_n e^{-\beta E_n} \langle E_n | \hat{C}(t) | E_n \rangle$ – for the quantum stadium billiard. One would expect it to be the case, indeed, because the quantum thermal state in this system has no semiclassical description, which would correspond to a particle moving with a definite velocity. Instead, it mixes up different momenta and positions. So, this thermal average involves the states with well-developed quantum interference, where no classical dynamics is present already at $t = 0$. In addition, it primarily

119

accounts for "the most quantum" low-energy states (unless the temperature β^{-1} is very high) that also have low momenta, while the Lyapunov exponent is proportional to the momentum.

To get exponential growth in this and, we believe, in many other systems, we have to identify "the most classical" initial state and let it evolve with time. In the case of a billiard, the natural choice is a Gaussian minimal-uncertainty wave packet:

$$\Psi_{\text{cl}}(\mathbf{r}) \propto \exp\left[-\frac{(\mathbf{r} - \mathbf{r}_0)^2}{2\hbar_{\text{eff}}\sigma^2} + \frac{i}{\hbar_{\text{eff}}}\mathbf{p_0} \cdot \mathbf{r}\right], \tag{6.10}$$

where σ controls initial squeezing, and the parameters $\mathbf{r}_0$ and $\mathbf{p_0}$ are the initial average position and momentum of the wave packet. $|\mathbf{p}_0| = p_0 = 1$ is the unit of momentum introduced before.

Let λ_{cl} denote the classical Lyapunov exponent of the system at unit momentum $|\mathbf{p}| = 1$ (the mass is fixed at $m = 1$, so $\lambda_{\text{cl}}|_{\mathbf{p}} \propto |\mathbf{p}|$). There are two relevant time scales: the collision time $t_c \sim 1/\lambda_{\text{cl}}$ is of the order of the time it takes the wave packet to hit the billiard's wall, and the Ehrenfest time $t_E \sim |\ln \hbar_{\text{eff}}|/\lambda_{\text{cl}}$ is of the order of the time it takes a minimal-uncertainty wave packet to spread across the entire system. Classically, λ_{cl} is defined as the infinite-time average and can be obtained for (almost) any initial condition by allowing enough time for a trial trajectory to explore a sufficient fraction of the phase space. At early times, though, the exponent fluctuates a lot before it reaches its average value, and the early-time values depend on the initial conditions. In the quantum calculation, the classical physics is limited to $t < t_E$, which in our case allows for just a few collisions with
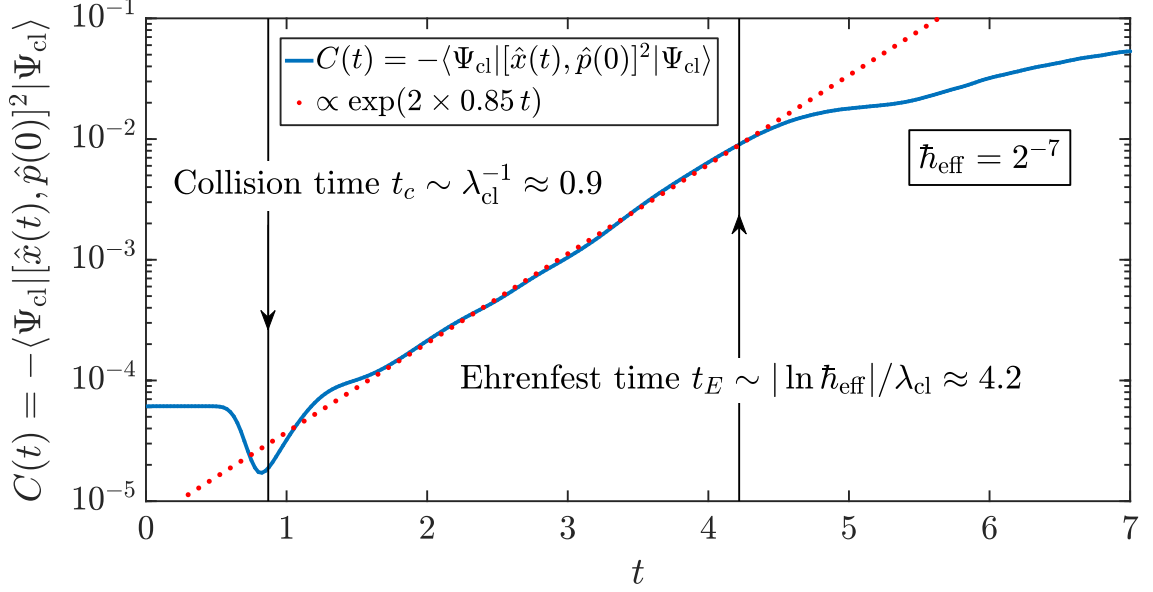
Figure 6.5: OTOC as the operator (6.1) averaged over the initial state (6.10) at early times (semi-log scale). $\hbar_{\text{eff}} = 2^{-7}$, $x_0 = y_0 = 0$, $p_{0x}/p_{0y} = e$, $\sigma = 1/\sqrt{2}$. Between t_c and t_E, the growth is nearly exponential, $C(t) \propto e^{2\tilde{\lambda}t}$, for the time longer than $4/(2\tilde{\lambda})$, but the value of $\tilde{\lambda}$ is not self-averaged yet.

the walls. But instead of a single trial trajectory, we start with a wave packet that is equivalent to averaging over an ensemble of trajectories, which, in turn, is equivalent to averaging over a longer time and decreases the fluctuations. Within our numerics, we were still unable to reach complete self-averaging, so while we see a robust exponential growth spanning the interval between t_c and t_E, the value of the exponent does depend on the initial wave packet and fluctuates moderately. However, it does not indicate any disagreement between quantum and classical description at early times. Classically, one can see the same fluctuations in the short-time Lyapunov exponent averaged over Wigner distributions of initial conditions that correspond to minimal-uncertainty wave packets used as initial conditions in our quantum calculations [250]. The fluctuations occur both as functions of time and initial conditions.

As shown in Fig. 6.5, at early times ($t < t_E$), OTOC does grow exponentially: $C(t) \propto e^{2\tilde{\lambda}t}$. In this semiclassical regime, we can replace the commutator with the Poisson brackets and average them classically over the ensemble of trajectories that corresponds to the Gaussian Wigner distribution $W_{\mathrm{cl}}(z)$ built from the initial state $|\Psi_{\mathrm{cl}}\rangle$. We denote this average as $\langle\!\langle \ldots \rangle\!\rangle$ [4]. We then have $C(t) \approx C_{\mathrm{cl}}(t)$ at $t < t_E$, where:

$$C(t) = \langle \Psi_{\mathrm{cl}} | \hat{C}(t) | \Psi_{\mathrm{cl}} \rangle \propto e^{2\tilde{\lambda}t}, \tag{6.11}$$

$$C_{\mathrm{cl}}(t) = \hbar^2 \left\langle\!\!\left\langle \left(\frac{\partial x(z,t)}{\partial x(z,0)} \right)^2 \right\rangle\!\!\right\rangle \propto \left\langle\!\!\left\langle e^{2\lambda_{\mathrm{cl}}^{\mathrm{ps}}(z,t)t} \right\rangle\!\!\right\rangle = e^{2\lambda t}, \tag{6.12}$$

and $\lambda_{\mathrm{cl}}^{\mathrm{ps}}(z,t)$ accounts for both the proportionality to the total momentum and the short-time effects giving $\lambda_{\mathrm{cl}}^{\mathrm{ps}}(z,t)$ the dependence on the rest of the phase-space coordinates and time. Note that λ in Eq. (6.12) is very close in spirit to the notion of the expansion entropy used for the recently updated definition of classical chaos [251]. Strictly speaking, one has to compare the quantum exponent $\tilde{\lambda}$ to the classical value of λ. But as noted above, available time $t < t_E$ is not sufficient for the quantum exponent $\tilde{\lambda}$ to self-average, and we do not reach exact quantitative agreement. Instead, in various calculations, we got $\tilde{\lambda}$ in the interval between $\lambda_{\mathrm{cl}}/2$ and $3\lambda_{\mathrm{cl}}/2$, while $\lambda \gtrsim \lambda_{\mathrm{cl}}$. $\lambda_{\mathrm{cl}} \approx 1.15$ is calculated for the classical stadium billiard in Refs. [37, 38, 39] [5]. We reproduced the same value in our classical-billiard cal-

---

[4]Note that the Wigner distribution $W_{\mathrm{cl}}(z)$ is everywhere positive, so that it is an actual probability distribution, reflecting the fact that the initial state does not have quantum interferences built in.

[5]In Refs. [37, 38, 39], the billiard area $A = \pi + 4$, hence they provide a different numerical value for the exponent (0.43) that scales as $A^{-1/2}$ and gives 1.15 for $A = 1$.

culation. The example of the quantum-billiard calculation in Fig. 4 has $\tilde{\lambda} \approx 0.85$ [6].

6.7 Summary and Outlook

We proposed a novel tool to study and even define quantum chaos in general quantum systems – the Lyapunov operator. We investigated the behavior of its level statistics and benchmarked it in a simple example of the stadium billiard. The Lyapunovian allowed us to unify the early-time signatures of chaos in the absence of quantum interference and the late-time ones related to well developed interference in a single quantity. Moreover, the Lyapunov operator can probe the transition between the two regimes and generalize a straightforward intuition behind the quantum-to-classical correspondence to a wider class of quantum systems. As compared to the OTOC, the Lyapunovian is free from the ambiguity of the initial-state choice, and thus can more reliably answer the question of regular-vs-chaotic nature of a given system.

We also demonstrated that, as opposed to the recently reported results [249], OTOC can be found to grow exponentially in chaotic systems when averaged appropriately.

Note that the level-spacing statistics is only one of the ways to study spectral correlations, and it only captures those at short ranges. Other statistical tools can uncover additional information hidden in the Lyapunovian. One interesting question

---

[6]Note that classical Lyapunov exponent was first extracted in a related way in Refs. [211, 229] from Loschmidt echo, which is closely related to OTOC.

is to study long-range correlations in the spectra of Lyapunov operators with such tools as spectral rigidity.

Chapter 7:   Early-Time Exponential Instabilities in Non-Chaotic Quantum Systems

7.1   Introduction

Quantum mechanics has a general effect that it washes out sharp features of classical dynamics due to its wave-like nature and the uncertainty principle. This effect becomes crucial for chaotic systems because sharp features such as sensitive dependence on initial conditions, that is the butterfly effect, are eventually destroyed. In isolated systems, this suppression of the butterfly effect occurs after a short period of semiclassical evolution – the length of this period grows logarithmically with system size [4, 189, 248, 252, 253, 254, 255, 256]. This time scale is known as the scrambling or Ehrenfest time, t_E.

Even though the scrambling time is usually short even in macroscopic isolated systems (which seems to be in a disagreement with observable phenomena), system's decoherence often resets dynamics back to the semiclassical regime. This explains why classical chaotic dynamics is ubiquitously observable [3, 255, 256, 257] (for alternative views on the long Erhenfest-time "paradox," see Refs. [258, 259]). Regardless of the explanation, the behavior of quantum systems in the Erhenfest window and

the fate of classical-to-quantum correspondence in this regime are clearly of fundamental interest, and we focus on this regime in the present manuscript.

In particular, we demonstrate here that in contrast to conventional wisdom, quantum mechanics can induce certain short-time exponential instabilities in models, which are classically non-chaotic [260]. While our construction, described below, is specific to billiards and out-of-time-ordered correlators, we believe that this behavior can exist in a variety of dynamical systems. Besides, both classical and quantum billiards are deeply connected to disordered metals [261, 262, 263, 264, 265, 266] (for a review, see Ref. [267]), transport phenomena in various systems, such as propagation of particles through rippled channels (see, e.g., Refs. [168, 169, 171, 173] and references therein), and also quantum dots (see, e.g., Ref. [268]).

We start with a model based on an illustrative set of observations. Consider a classical "mathematical billiard," i.e. a point particle within a closed domain reflecting off of its hard walls, such as the polygonal black shape in Fig. 7.1. It has been rigorously proven [269, 270] that the Kolmogorov-Sinai (KS) entropy and the closely related Lyapunov exponents of *any* polygonal billiard are strictly zero. Next, consider the corresponding "physical billiard," a classical hard disk of radius r_p reflecting off of the same polygonal walls. Clearly, this physical billiard is equivalent to a mathematical billiard of a smaller size, since the particle's center is not allowed to approach the walls of the physical billiard closer than r_p. Such equivalent billiard is shown by the inner blue shape in Fig. 7.1. We assume that the particle's mass is concentrated in the center, and ignore rotational motion. A crucial observation [271, 272] is that this redrawing may give rise to a smoothing of sharp features of non-
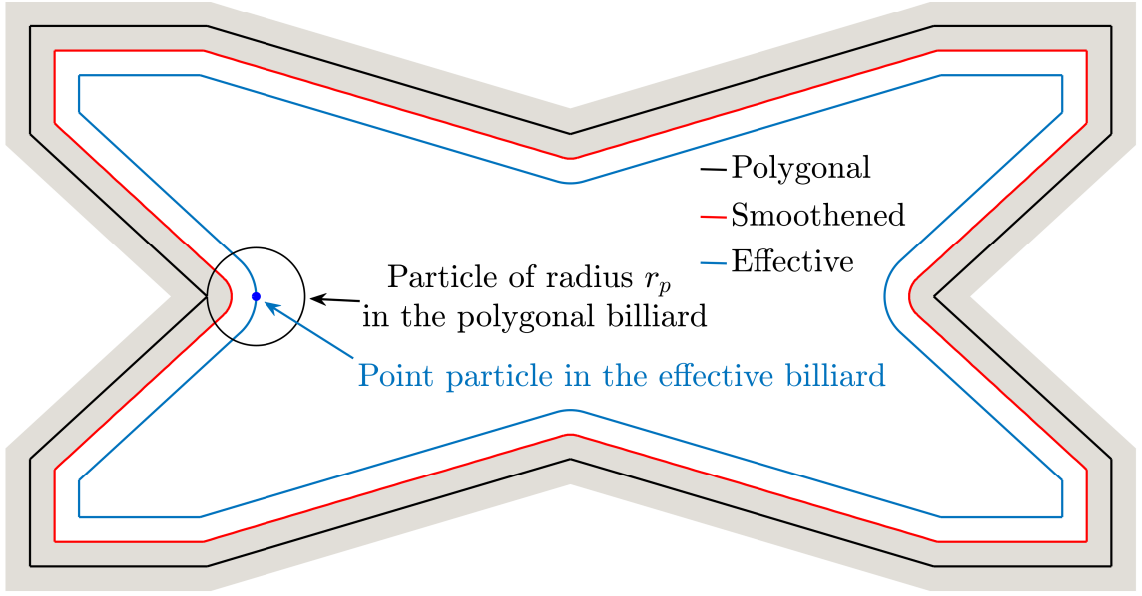
Figure 7.1: Outer black line: polygonal butterfly-shaped billiard. The area is unit. Inner blue line: effective mathematical billiard hosting a point particle classically equivalent to the outer polygonal billiard hosting a rigid circular particle of radius $r_p = \sigma\sqrt{\hbar_{\text{eff}}/2}$ and zero moment of inertia. Note that the inward-pointing corners of the polygonal billiard are rounded into circular arcs or radius r_p, making the effective mathematical billiard classically chaotic with positive Lyapunov exponent. Gray shaded region: a close sub-r_p vicinity of the billiard wall: small changes of the billiard geometry within this region do not affect the early-time quantum dynamics. Middle red line: a smoothened billiard used for comparison purposes below.

convex polygons, such as the black shape in Fig. 7.1. The resulting shape is no longer a polygon, and the obstruction for the KS entropy to vanish is removed. Indeed, the inner blue billiard in Fig. 7.1 is classically chaotic, with a positive Lyapunov exponent. Finally, consider a quantum particle embedded into a non-convex polygonal billiard. Semiclassical early-time dynamics of a quantum wave packet is in a certain sense similar to motion of a finite-size classical particle; i.e., classically chaotic motion in the physical billiard. As shown below, there is indeed the onset of exponential instabilities in the classically non-chaotic systems such as this one, hence providing an example of violation of the conventional view on the classical-to-quantum correspondence.

To diagnose this behavior, we employ the out-of-time-ordered correlator (OTOC). The OTOC was introduced by Larkin and Ovchinnikov [26] in the context of quasi-classical approximation in the theory of superconductivity in disordered metals and used recently in the pioneering works by Kitaev [27] and Maldacena et al. [28] to define and describe many-body quantum chaos with an eye on fundamental puzzles in black-hole physics. In the last few years, the OTOC has become a popular tool to describe "quantum chaos" in many-body quantum systems (see e.g. Refs. [195, 196, 197, 198, 199, 200, 231, 273, 274, 275, 276, 277]). It was shown in Refs. [230, 278, 279] (see Chapters 5 and 6) that the exponential growth of the OTOC, although not always equal, might be connected to the exponential divergences of orbits in the phase space of an effective classical system. In certain cases, such as the celebrated Sinai billiard [33] and Bunimovich stadium [34, 35], it is straightforward to understand this classical limit. Below, we consider non-chaotic

Figure 7.2: Ergodic hierarchy [20] provides a nested classification of non-integrable systems. Only K- and B-systems are chaotic and have positive Lyapunov exponents, while merely ergodic and merely mixing systems have no exponential instabilities.

polygonal billiards instead. In a polygon, for any pair of trajectories – no matter how close the initial conditions are – one can identify the origin of each trajectory evolving the dynamics backward in time [269, 270], ensuring that the KS entropy is zero. Note that in the ergodic hierarchy, which is displayed in Fig. 7.2 in the order of "increasing chaoticity," polygonal billiards fall within at most the strongly mixing class (only K- and B-systems have a positive KS entropy; see e.g. Ref. [20] for a detailed discussion of the hierarchy). Interestingly, however, the mixing property at the classical level can be sufficient to generate Wigner-Dyson or intermediate energy-level statistics on the quantum side, as was shown, for example, in Ref. [32] for a family of irrational triangular billiards [280].

Apart from this "quantum" Lyapunov instability, where quantum mechanics effectively promotes the corresponding classical system in the ergodic hierarchy, there are potentially more prosaic sources of early-time instabilities in OTOC in

various systems. First, note that the classical definition of exponential Lyapunov instabilities involves taking two limits: infinitesimally small initial separation in the phase space and infinite time-limit in the subsequent evolution. However, neither limit is available quantum-mechanically because a wave-packet always has a finite size per uncertainty principle and subsequently spreads out on time-scales of order the Ehrenfest time. Second, there is a distinction between the quantum-mechanical expectation value in the way quasiclassical trajectories are accounted for and the classical phase-space average (see Chapter 5 and Ref. [230]). Therefore, in most numerical simulations of OTOCs the proper Lyapunov limit can not be enforced and the dynamics of the wave-packets may involve rapid growth, which is however spurious in nature. To explore these types of phenomena, we also study convex polygonal billiards (specifically an irrational triangle) and some integrable systems.

7.2   Models

We perform explicit calculations for the butterfly-shaped polygonal billiard shown in Fig. 7.1 (outer black line) [260], the quadrilateral non-convex billiard shown in Fig. 7.3, and a triangular billiard obtained from it by removing the vertex at $(0; 0)$.

We launch a wave-packet with the initial wave-function

$$\Psi_0(\mathbf{r}) \propto \exp\left[-\frac{(\mathbf{r} - \mathbf{r}_0)^2}{2\hbar_{\text{eff}}\sigma^2} + \frac{i}{\hbar_{\text{eff}}}\mathbf{p_0} \cdot \mathbf{r}\right] \tag{7.1}$$

by decomposing it into the billiard's energy eigenstates and evolving accordingly.
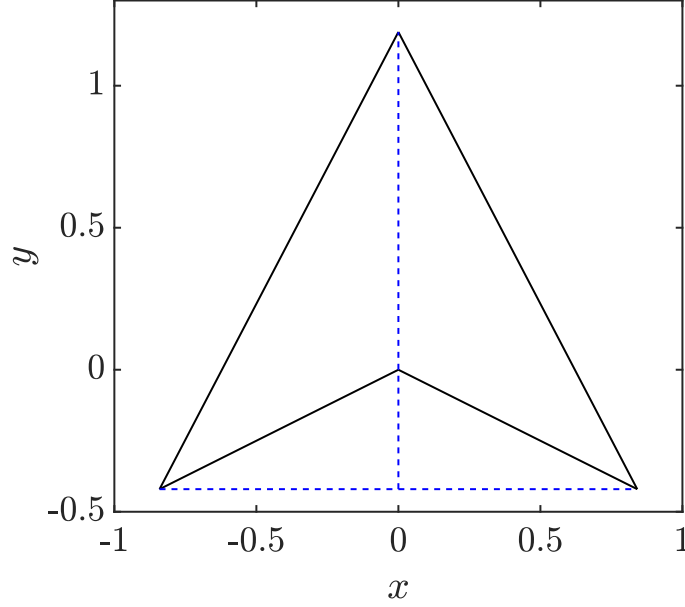
Figure 7.3: Deformed triangular billiard (unit area). All angles are incommensurate with π. For a finite particle, the inward-pointing corner gets rounded analogous to those in Fig. 7.1.

This requires numerical solution of the Schrödinger equation for the billiard:

$$-\frac{\hbar_{\text{eff}}^2}{2}\nabla^2\Psi(\mathbf{r}) = E\Psi(\mathbf{r}), \quad \Psi(\mathbf{r})\Big|_{\mathbf{r}\in\text{billard walls}} = 0. \tag{7.2}$$

Here $\hbar_{\text{eff}} = \hbar/(p_0\sqrt{A})$, A is the billiard's area, and $p_0 = |\mathbf{p}_0|$ is the wave-packet's average momentum. $A = 1$ and $p_0 = 1$ are chosen as the units along with the particle's mass $m = 1$. The butterfly-shaped billiard has two reflection symmetries with respect to $x \to -x$ and $y \to -y$. Thus, its eigenstates fall into four parity classes. In order to enforce these parities and speed up the calculations, one typically solves the eigenvalue problem on a quarter of the billiard imposing the Dirichlet and/or Neumann boundary conditions on each cut, thereby determining the parity class of the solutions. We solve these four boundary-value problems for the Laplace operator numerically using the finite-element method, and find eigenstates of each

131

class up to a certain energy cutoff. The accuracy of the numerical solution generally decreases with the number of found eigenstates [244]. We use Weyl's formula for the number of modes [182] to control it. Weyl's law sets the asymptotic behavior of the average number $\mathcal{N}(E)$ of eigenstates below energy E as: $\mathcal{N}(E) \simeq [A/(4\pi)]\,\varepsilon - [P/(4\pi)]\,\sqrt{\varepsilon}, \quad \varepsilon \to \infty$, where $\varepsilon = 2E/\hbar_{\mathrm{eff}}^2$ and P is the billiard's perimeter. For our present purposes, it is sufficient to use around $N_{\mathrm{max}} = 10^4$ eigenstates, and within this range, we have exact agreement with Weyl's law, i.e. the number of found states is centered around Weyl's asymptote. In addition, we repeat the calculations with the boundary-integral method and obtain the same results.

Due to the lack of narrow outer corners, the butterfly-shaped billiard allows for a relatively long lifetime of the initial minimal-uncertainty wave packet until this packet becomes completely scrambled and loses classical-like dynamics (see Fig. 7.4). Along with this billiard, we introduce an effective mathematical billiard (Fig. 7.1, inner blue line) that is obtained by tracing the set of positions available to the center of a circular particle of radius $\sigma\sqrt{\hbar_{\mathrm{eff}}/2}$ inside the polygonal butterfly billiard. The squeezing parameter σ is defined in Eq. (7.1).

7.3 Diagnostic tool

As a measure of quantum chaotic dynamics, we use the OTOC [27, 28, 195, 196, 197, 198, 199, 200, 230, 231, 273, 274, 275, 276, 277, 278, 279] defined as:

$$C(t) = -\left\langle [\hat{x}(t),\,\hat{p}_x(0)]^2 \right\rangle,\tag{7.3}$$
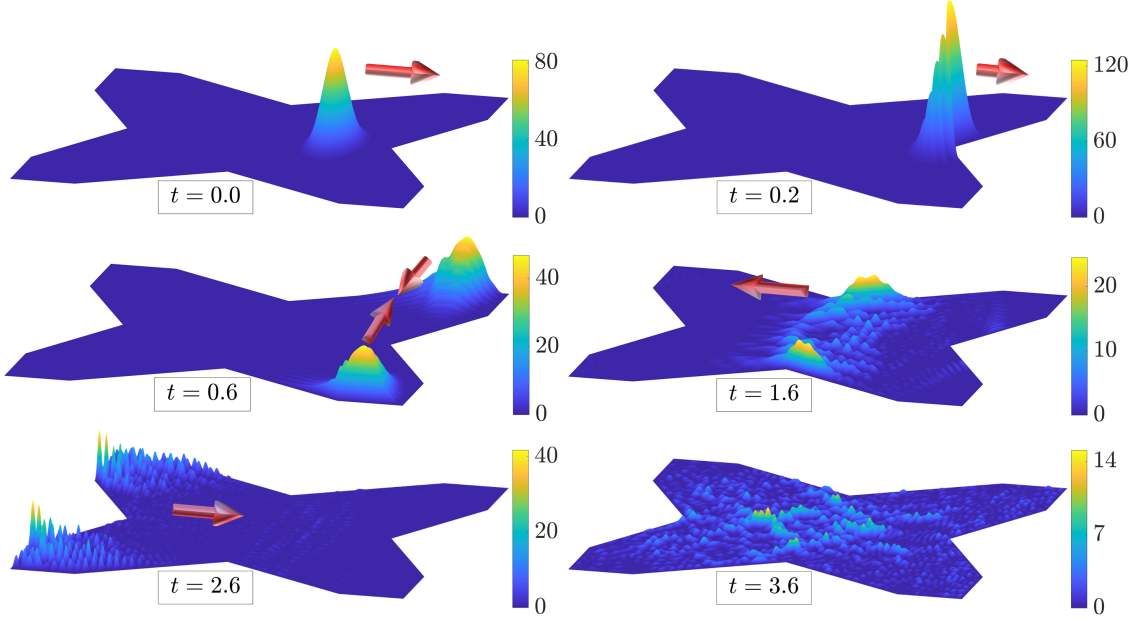
Figure 7.4: An example of successive stages of the wave-packet evolution, $|\Psi(\mathbf{r}, t)|^2$, in the butterfly-shaped polygonal billiard. Red arrows indicate the directions of motion of the components. Initial velocity is aimed at an inner corner.

where $\hat{x}(t)$ and $\hat{p}_x(t)$ are the Heisenberg operators of the x-components of the particle's position and momentum. As was first pointed out by Larkin and Ovchinnikov [26], the OTOC probes the sensitivity of quasiclassical trajectories to initial conditions as $\hat{p}_x(0) = -i\hbar_{\text{eff}}\partial/\partial x(0)$, and hence $C(t) = \hbar^2 \left\langle \left(\frac{\partial x(t)}{\partial x(0)} \right)^2 \right\rangle$. Therefore, classical Lyapunov-like growth is anticipated at early times, $C(t) \propto \exp(2\tilde{\lambda}t)$, for a chaotic system, with $\tilde{\lambda}$ related to its Lyapunov exponent in the respective subspace.

As was shown in Chapter 6 and Ref. [279], whether the OTOC actually grows exponentially or not, depends on an initial quantum state and on the existence of a finite time window between the first collision and the Ehrenfest time. For billiards, a natural choice of the initial state is the minimal-uncertainty wave-packet, Eq. (7.1). The scrambling (Ehrenfest) time in chaotic systems is short and grows logarithmically slowly with system size: $t_E = \ln(\hbar_{\text{eff}}^{-1})/\lambda_{\text{cl}}$, where λ_{cl} is the posi-

tive Lyapunov exponent of the classical counterpart of the system [4, 252]. This estimate is based on the fact that, in contrast to non-chaotic systems where the spreading of wave-packets is algebraic in time, the spreading is typically exponential in chaotic systems, i.e. in quantum counterparts of K- and B-systems from the ergodic hierarchy. Extending the Ehrenfest window to cover the long-time ergodic classical behavior, which is required to define the global Lyapunov exponents in chaotic systems, is an exponentially demanding numerical task. However, local finite-time Lyapunov exponents can be defined, although they fluctuate at these short times [279].

7.4   Breakdown of classical-to-quantum correspondence

As discussed in Chapter 6 [279], in quantum billiards, which are classically chaotic, the exponential growth of the OTOC may be related to the classical Lyapunov instability and extends up until the Ehrenfest time. After that, the wave packet is spread across the entire system, and no further exponential growth is possible.

The classical counterpart of the OTOC is defined as:

$$C_{\text{cl}}(t) = \left\langle\!\!\!\left\langle \lim_{\Delta x(0) \to 0} \left(\frac{\Delta x(t)}{\Delta x(0)} \right)^2 \right\rangle\!\!\!\right\rangle, \tag{7.4}$$

where $\langle\!\langle \ldots \rangle\!\rangle$ denotes the classical phase-space average over the Gaussian Wigner function corresponding to the initial quantum packet in Eq. (7.1), and Δx is the distance along the $x-$axis between a pair of trajectories starting near some point

in the phase space. $C_{\mathrm{cl}}(t)$ agrees with $C(t)/\hbar_{\mathrm{eff}}^2$ all the way up to t_E. After that, they deviate from each other. The quantum-mechanical OTOC slows down and eventually saturates, while the classical one continues to grow exponentially.

In the polygonal billiards, there are no positive classical Lyapunov exponents, and the corresponding classical OTOC does not grow exponentially at any time, as shown in the inset in Fig. 7.5 for the case of the butterfly-shaped polygonal billiard (dotted black and solid green lines). However the quantum-mechanical OTOC in polygonal billiards shows a clear exponential growth at early times that has no origin in the classical counterparts, as demonstrated in Fig. 7.5 (main plot and inset), as well as in Figs. 7.6, and 7.7 (described below).

As discussed in the introduction, the motion of a minimal-uncertainty wave packet is in some sense similar to that of a finite-size disk. Classical motion of such a disk gives rise to an effective billiard which hosts a point-like particle at the disk's center that is not allowed to approach the walls of the original billiard closer than by the disk's radius. Many billiards preserve their status within the ergodic hierarchy upon this procedure (e.g., a Bunimovich stadium remains a stadium with a smaller area and convex polygons also turn into similar convex polygons). Not so for non-convex polygonal billiards, which go up the ergodic hierarchy for a finite-sized particle from the strongly mixing class to the K-chaotic one. In such non-chaotic systems, there can still be measure-zero sets of unstable points, and these get smeared over finite-measure regions by introducing a finite size of the particle. A quantum wave packet, which always has a finite width, can have a similar effect.

An additional consideration is that polygons constitute an everywhere dense
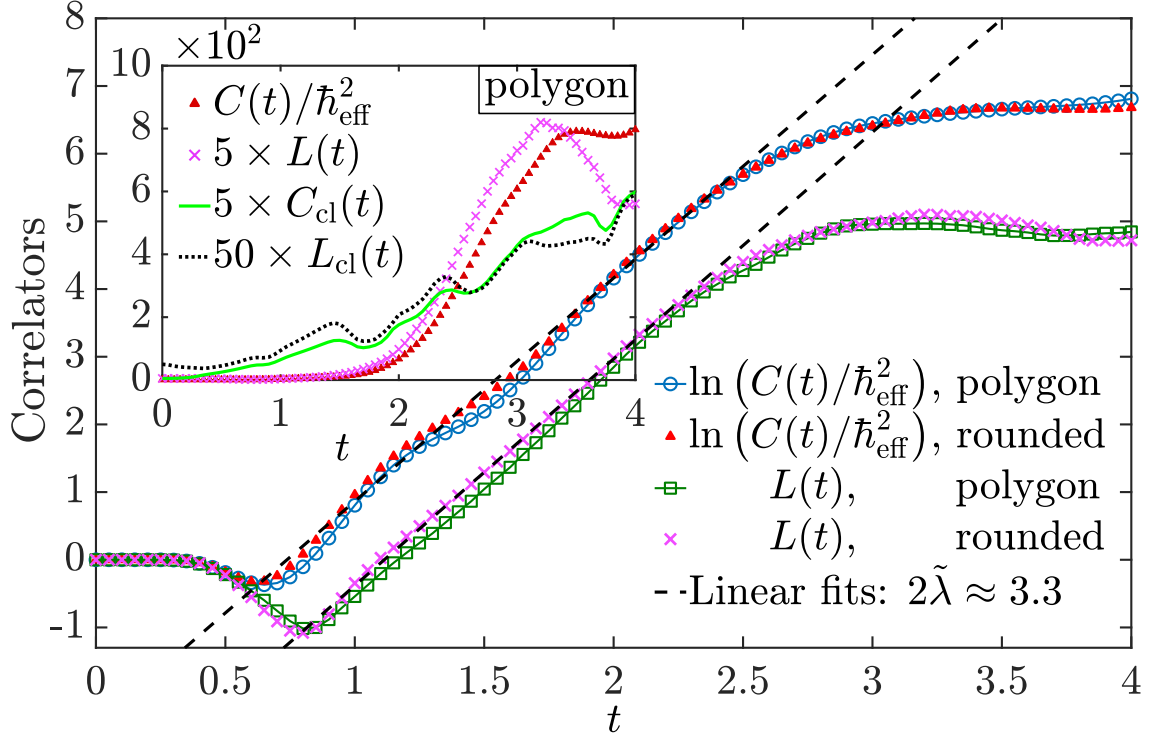
Figure 7.5: Main plot – open blue circles and line: logarithm of the OTOC in the polygonal butterfly-shaped billiard: $\ln\left(C(t)/\hbar_{\text{eff}}^2\right) = \ln\left(-\frac{1}{\hbar_{\text{eff}}^2}\left\langle[\hat{x}(t),\hat{p}_x(0)]^2\right\rangle\right)$. Solid red triangles: the same in the rounded version of this billiard (middle red line in Fig. 7.1). A remarkable agreement demonstrates that the growth in both cases is the same, supporting our finite-size-related arguments. In addition, we show the corresponding behavior of an alternative diagnostic, $L(t) = \left\langle\ln\left(-\frac{1}{\hbar_{\text{eff}}^2}[\hat{x}(t),\hat{p}_x(0)]^2\right)\right\rangle$, that swaps the order of averaging and logarithm to that of the proper definition of the classical Lyapunov exponent. For chaotic systems with uniform phase space, one would expect $L(t) = 2\tilde{\lambda}t + \text{const}$ at $t < t_E$. Green squares and line: $L(t)$ in the polygonal butterfly-shaped billiard. Pink crosses: $L(t)$ in the rounded billiard. Dashed black lines: linear fits for $\ln(C(t)/\hbar_{\text{eff}}^2)$ and $L(t)$ in the polygon. Both show the exponent $2\tilde{\lambda} \approx 3.3$ that is 5 times larger than the inverse time-window, which ensures that the fit is valid. Inset – the comparison between $C(t)/\hbar_{\text{eff}}^2$ and $C_{\text{cl}}(t) = \left\langle\{x(t),p_x(0)\}_{\text{Poisson}}^2\right\rangle$ [see Eq. (7.4)] and between $\exp[L(t)]$ and $\exp[L_{\text{cl}}(t)] = \exp\left[\left\langle\ln\{x(t),p_x(0)\}_{\text{Poisson}}^2\right\rangle\right]$ in the polygonal quantum and classical billiards, respectively. $\hbar_{\text{eff}} = 2^{-7}$, $\sigma = 1/\sqrt{2}$, $R_s = \frac{\sqrt{2}-1}{16\sqrt{2}} \approx 0.02$.
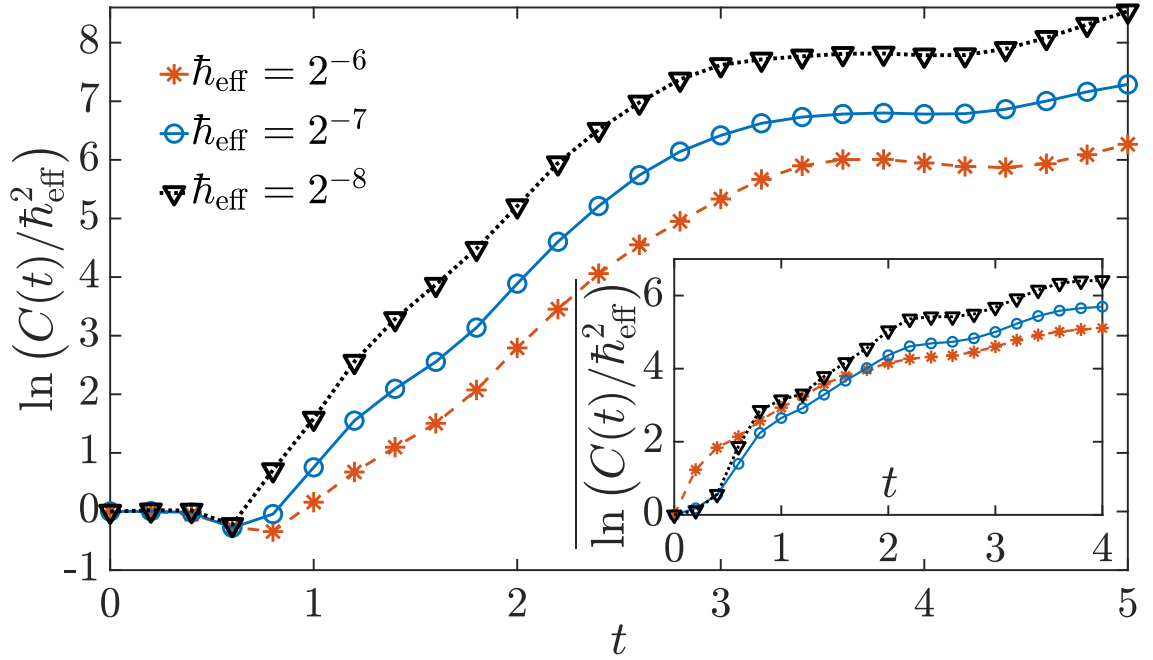
Figure 7.6: Main plot – logarithm of the OTOC as a function of time in the polygonal butterfly-shaped billiard at three different values of $\hbar_{\text{eff}}$. The exponential growth of the OTOC hinges on the finite wave-packet size. Inset – logarithm of the OTOC in the quadrilateral billiard (Fig. 7.3), averaged over an ensemble of initial conditions as indicated by the bar, $\overline{\cdots}$, with the corresponding values of $\hbar_{\text{eff}}$. $\sigma = 1/\sqrt{2}$.

measure-zero set in the space of closed curves on a plane, and the phase space of the corresponding billiards contains isolated unstable points. A slight variation of the wall's shape almost always results in finite-curvature regions and smears out singular phase-space points. A possible consequence of that would manifest in that a quantum-mechanical wave packet effectively "rounds" singularities even if they originate from outer corners of polygons, including those in convex polygonal billiards considered below. This can be generalized to a statement that quantum mechanics promotes measure-zero sets of unstable points into finite-measure sets [260]. We check these conjectures by varying the billiard's boundary within the shaded gray region in Fig. 7.1, and, in particular, compare the behavior of the OTOC in the polygonal and in a rounded billiard, such as the middle red line in Fig 7.1. The latter system is classically chaotic. We find a good agreement between the quantum OTOCs in the two, as demonstrated in Fig. 7.5. In addition, from this comparison we can infer that there are no significant effects related to the non-smoothness of the polygonal boundary, such as diffraction, as in the case in the quantum baker's map [281]. Note a major difference between the Lyapunov behaviors of the quantum baker's map and our billiards: the latter do not have a classical Lyapunov exponent at all and the exponential growth of the OTOC there is a purely quantum effect.

At smaller values of $\hbar_{\mathrm{eff}}$, the wave packets are tighter, and their sides become steeper. Following the reasoning in Refs. [282, 283], it causes the rate of the OTOC's divergence, $\tilde{\lambda}$, to be larger than that at larger values of $\hbar_{\mathrm{eff}}$, as shown in Fig. 7.6, main plot. The inset in Fig. 7.6 shows an analogous behavior for the quadrilateral billiard shown in Fig. 7.3.

7.5 Quantum dynamics in convex polygonal and integrable billiards

Classical convex polygonal billiards do not change their status within the ergodic hierarchy upon promoting their point-particle versions to those with finite-size hard particles. However, quantum-mechanically, they still show a rapid initial growth of the OTOC coexisting with an oscillatory behavior, as we demonstrate for an irrational triangular billiard obtained from the quadrilateral one in Fig. 7.3 by removing the vertex at $(0;0)$. The effective rate of growth is smaller than for the non-convex billiard, but similar signs of instability are present. Note that this growth should not be attributed to any mixing dynamics in the classical counterparts of these billiards. Upon quantization, the level statistics of irrational triangular billiards – the most widely used "quantum-chaotic" diagnostic – is close to the Wigner-Dyson surmise [32], putting them outside of the Bohigas-Giannoni-Schmit conjecture [29, 30]. As shown in Fig. 7.7, the early-time behavior has a period of what looks very much like an exponential growth, although it is modulated by the effects of collisions with the walls.

We believe that this behavior of OTOC in convex billiards is due to the fact that a quantum simulation can not as a matter of principle access the proper small-distance and long-time limit where classical Lyapunov exponents are defined. As such, this type of growth in OTOC is a property of the initial wave-packet rather than the system where it propagates. If so, similar growth should be observable in integrable systems as well. We have considered the simplest billiard – the rectangular billiard – and indeed found that a weak growth can be detected (again superimposed

Figure 7.7: Logarithm of the OTOC, $\ln(C(t)/\hbar_{\mathrm{eff}}^2)$, in an irrational triangular billiard (upper blue line and open circles). After an initial-condition-dependent delay, the OTOC shows exponential grows, although at a rate lower than that for the non-convex billiard. The other related correlator, $L(t)$, introduced in Fig. 7.5, is shown for comparison (lower red line and asterisks). Black dashed lines show linear fits with $2\tilde{\lambda} \approx 1$, which is over 5 times larger than the inverse time window, ensuring that the fit is valid.

on oscillations). Since the rectangle factorizes into two one-dimensional segments, one can also look at the most basic textbook quantum mechanical problem – a particle in a box. The OTOC can be calculated to a large degree analytically in this case and shows clear recurrent oscillations including short time-intervals of growth. Of course these periods of growth have no relation to chaos or the butterfly effect and do not contain any valuable information. The behavior of OTOC in these integrable systems is presented in the following section.

All in all, there appear to exist two sources of rapid growth of OTOC in billiards: one related to a genuine Lyapunov instability (in chaotic billiards and those that are promoted in the chaotic hierarchy upon quantization) and a spurious growth related to a finite-size wave-packet enforcing the "wrong" averaging of the underlying classical dynamics. Such growth is present independently of the status of the effective billiard in the chaotic hierarchy. In order for OTOC to have a physical meaning, it is important to disentangle the two types of contributions. It should be possible by looking at how the growth rates scale with the Planck constant and extracting the "interesting" genuine Lyapunov growth, if any. The details of this scaling procedure will be discussed in a subsequent publication.

7.6 Quantum dynamics in integrable polygonal billiards and a 1D particle in a box

We show here that integrable polygonal billiards and even the textbook example of a particle in a 1D box also demonstrate what appears as an exponential

instability in the OTOC. Fig. 7.8 shows fast growth of the OTOC by more than 8 orders of magnitude in a rectangular billiard. As this billiard is completely separable in the (x, y) coordinates, and we only consider operators along the x axis, we should observe exactly the same dynamics in a 1D particle-in-a-box model. We do an independent semi-analytic calculation of the OTOC in the latter case. In particular, we use the analytically known eigenvalues and eigenfunctions of the 1D box to decompose the initial Gaussian wave packet, $\Psi_0 = \sum_n \psi_n |n\rangle$, where $\psi_n = \langle n|\Psi_0\rangle$ and $\hat{H}_{\text{box}}|n\rangle = E_n|n\rangle \equiv \hbar_{\text{eff}}\varepsilon_n|n\rangle$, and propagate it in time. The only two steps done numerically are the calculation of the overlap coefficients ψ_n and the summation of the corresponding series, as shown in the following equations:

$$C(t) = -\left\langle \Psi_0 \left| [\hat{x}(t), \hat{p}_x(0)]^2 \right| \Psi_0 \right\rangle = -\sum_{n,m} \psi_n^* \psi_m \left\langle n \left| [\hat{x}(t), \hat{p}_x(0)]^2 \right| m \right\rangle, \qquad (7.5)$$

$$\left\langle n \left| [\hat{x}(t), \hat{p}_x(0)]^2 \right| m \right\rangle = \sum_k \left\langle n \left| [\hat{x}(t), \hat{p}_x(0)] \right| k \right\rangle \left\langle k \left| [\hat{x}(t), \hat{p}_x(0)] \right| m \right\rangle, \qquad (7.6)$$

$$\langle n |\hat{x}(t)\hat{p}_x(0)| k\rangle = \left\langle n \left| e^{it\frac{\hat{H}_{\text{box}}}{\hbar_{\text{eff}}}} \hat{x} e^{-it\frac{\hat{H}_{\text{box}}}{\hbar_{\text{eff}}}} \hat{p}_x \right| k \right\rangle = \sum_j e^{it\varepsilon_n} (x)_{nj} e^{-it\varepsilon_j} (p_x)_{jk}, \qquad (7.7)$$

$$(x)_{nm} = \left(\frac{2}{\pi}\right)^2 L \frac{nm\left[(-1)^{n+m} - 1\right]}{(n^2 - m^2)^2}, \quad (p_x)_{nm} = \frac{2}{L} \frac{nm\left[(-1)^{n+m} - 1\right]}{(n^2 - m^2)}, \quad n \neq m, \tag{7.8}$$

where L is the length of the box, $(x)_{nm}$ and $(p_x)_{nm}$ are the matrices of the operators $\hat{x} = \hat{x}(0)$ and $\hat{p}_x = \hat{p}_x(0)$, respectively, in the eigenbasis of the model. $(x)_{nn} \equiv L/2$ and $(p_x)_{nn} \equiv 0$ for any n. We repeatedly used the resolution of identity in these transformations. And indeed, we obtain the same results as in
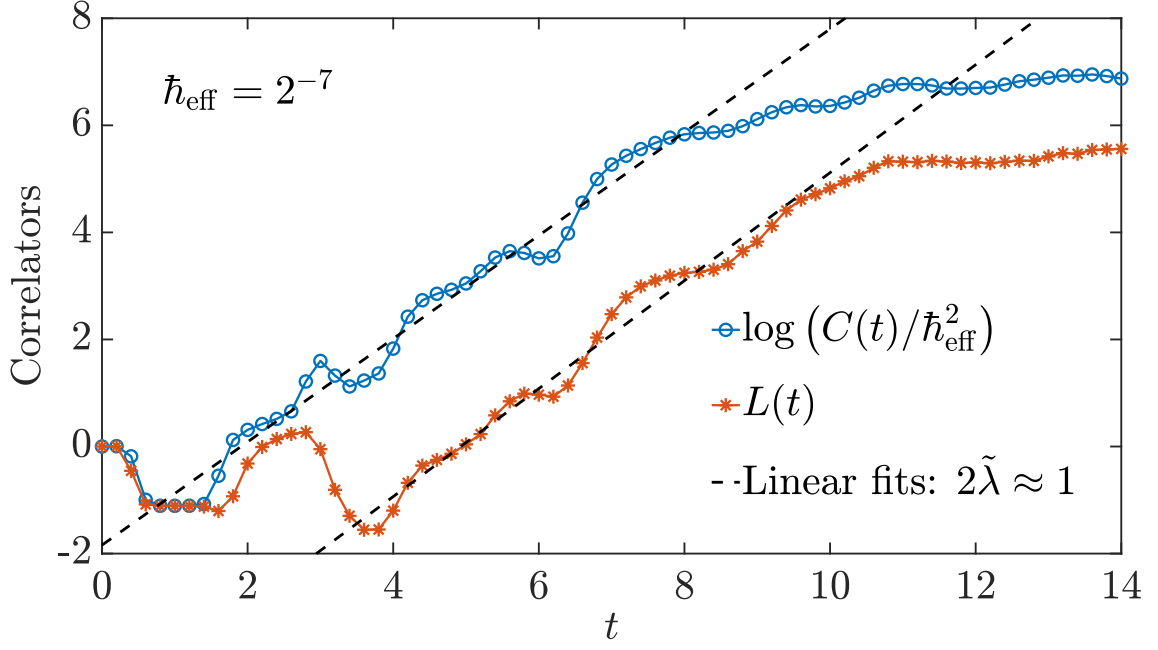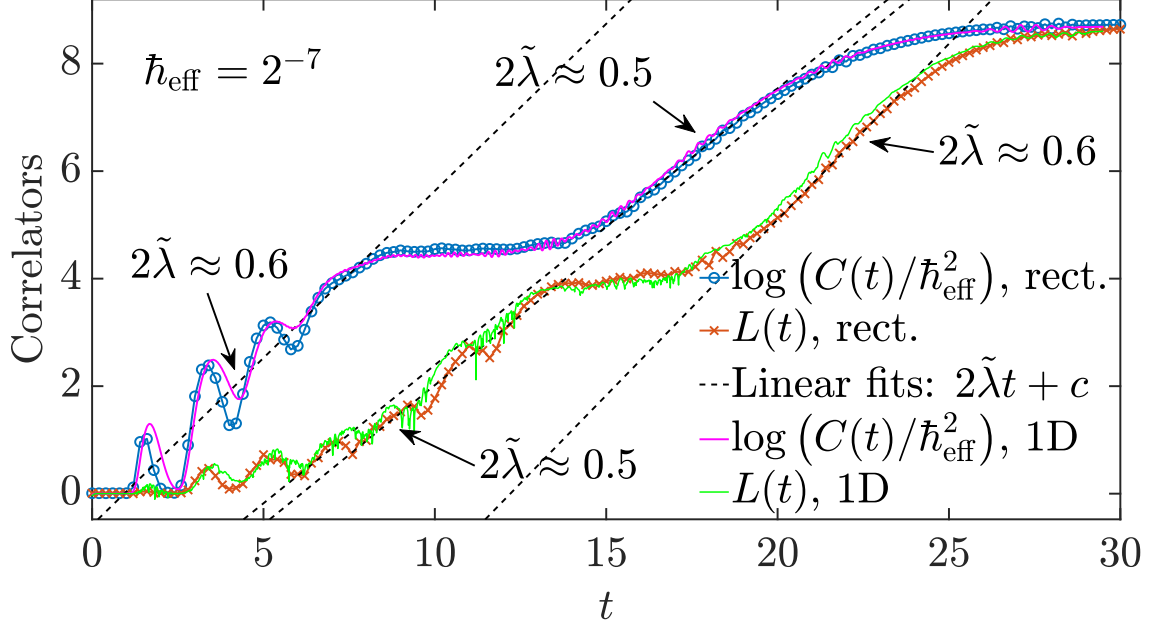
Figure 7.8: Logarithm of the OTOC, $\ln(C(t)/\hbar_{\mathrm{eff}}^2)$, in a rectangular billiard (upper blue line and open circles). The OTOC shows periods of what appears as exponential growth superimposed with oscillations due to collisions. The growth rate is the smallest among our examples but can be made continuous all the way to the saturation value by varying the initial conditions. The related L-correlator, introduced in Fig. 5 in the main text, is shown for comparison (lower red line and crosses) and demonstrates the same behavior. Black dashed lines show linear fits with $2\tilde{\lambda} \approx 0.5 \div 0.6$, which is over 3 times larger than the individual inverse time-windows, ensuring the adequate fit. Pink and light-green lines show the comparison with the case of a particle in a 1D box. The data agrees, as expected. Longer-time data for the 1D case is presented in Fig. 7.9.
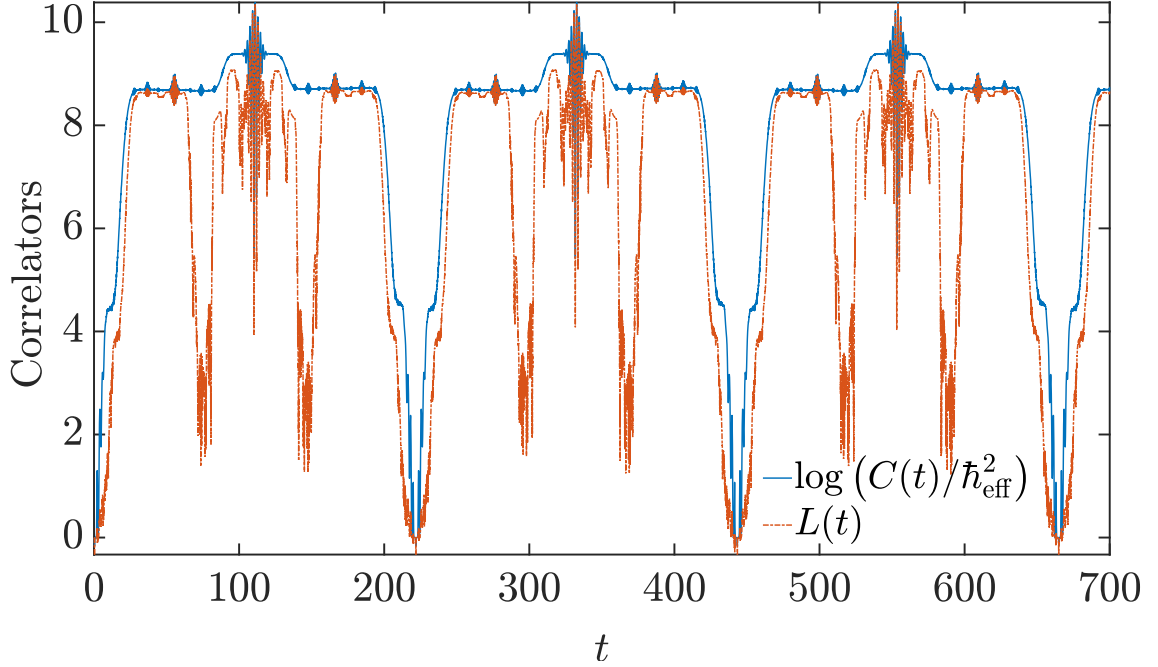
Figure 7.9: Logarithm of the OTOC, $\ln(C(t)/\hbar_{\text{eff}}^2)$, for a particle in a 1D box (upper blue line). The OTOC shows periods of "exponential" growth and decay, as well as those of oscillatory and stable behavior, and its evolution is strictly periodic. The L-correlator, introduced in Fig. 5 in the main text, is shown for comparison (lower red dashed-dotted line). It demonstrates the same "exponential" instability at early time and periodic structure at longer time. The length of the box of ≈ 1.65 and the particle's momentum $p_0 \approx 0.89$ are chosen to correspond to those along the $x-$axis in the rectangular billiard in Fig. 7.8.

our numerical curves for the rectangular billiard that show the same exponential-looking growth – see Fig. 7.8. Given that this system is 1D and integrable, its dynamics is inevitably periodic, which is confirmed by extending the time further, as demonstrated in Fig. 7.9. However, at relatively short times, the growth of OTOC and the L-correlator both show divergences well fitted by exponential functions.

Chapter 8: Conclusion

The present thesis is devoted to a number of novel developments that can be broadly attributed to the field of quantum chaos, which has started to undergo a rapid revival of broad interest in the past few years, with a particular emphasis on its many-body generalizations and peculiar effects that violate some of the textbook truths, make our intuition fail, pose new questions and even open doors for some opportunities in quantum technologies. We, however, started to work in the field a little before the latest wave of interest emerged, and used our unique position to step back and devote our efforts to ensure that the novel developments – our own ones included – are given a thorough examination from the well-established perspective of the traditional quantum chaos, that offers many vital connections to classical physics and visual interpretations that the "many-body quantum chaos", as it is often called now, lacks due to its high complexity.

In Chapters 2 and 3, we studied dynamical localization in few- and many-body settings. It has been considered multiple times in various models in the traditional quantum chaos research before. But we were able to give for the first time an affirmative answer to the question of whether it can survive in the presence of interactions and in the absence of explicit integrability.

In Chapter 4, we applied a novel localization-landscape-based approach to study transport and an analog of Anderson localization in rippled channels. We showed how visually instructive the effective confining potential is. It allows one to predict transport properties of a channel in a much simpler way than the traditional way based on solving the Schrödinger equation directly.

In Chapter 5, we revisited a recently introduced approach to define quantum Lyapunov exponents based on the notion of the OTOC. We showed what the OTOC means in the systems that can be studied efficiently from both quantum and classical perspectives, gave it a precise classical interpretation, and showed how its exponential growth can abruptly end due to quantum interference. We also demonstrated the intrinsic scaling characteristic of the OTOC.

In Chapter 6, we introduced a new hybrid quantum-chaotic measure, the Lyapunovian level statistics, which allowed us to bridge the gap between seemingly unrelated early-time and infinite-time approaches to quantum chaos – the OTOC and the random-matrix theory.

Then, in Chapter 7, we showed that OTOC can pick up zero-measure divergences in classical phase space that are not significant for classical dynamics and, thereby, could lead to a – somewhat artificial in our opinion – effect of quantum generation of chaos, as measured by the OTOC.

Bibliography

[1] N. Bohr. Über die serienspektra der elemente. *Zeitschrift für Physik*, 2(5):423–469, Oct 1920.

[2] Tien-Yien Li and James A. Yorke. Period three implies chaos. *The American Mathematical Monthly*, 82(10):985–992, 1975.

[3] Wojciech Hubert Zurek and Juan Pablo Paz. *Why We Don't Need Quantum Planetary Dynamics: Decoherence and the Correspondence Principle for Chaotic Systems*, pages 167–177. Springer Netherlands, Dordrecht, 1999.

[4] G. P. Berman and G. M. Zaslavsky. Condition of stochasticity in quantum nonlinear systems. *Physica A*, 91(3):450 – 460, 1978.

[5] G. Casati, B.V. Chirikov, F.M. Izraelev, and Joseph Ford. Stochastic behavior of a quantum pendulum under a periodic perturbation. In Giulio Casati and Joseph Ford, editors, *Stochastic Behavior in Classical and Quantum Hamiltonian Systems*, volume 93 of *Lecture Notes in Physics*, pages 334–352. Springer Berlin Heidelberg, 1979.

[6] Fritz Haake. *Quantum Signatures of Chaos*, volume 54 of *0172-7389*. Springer-Verlag Berlin Heidelberg, 3 edition, 2010.

[7] Michael Berry. Quantum chaology, not quantum chaos. *Physica Scripta*, 40(3):335–336, sep 1989.

[8] B. V. Chirikov. A universal instability of many-dimensional oscillator systems. *Phys. Rep.*, 52(5):263 – 379, 1979.

[9] B.V. Chirikov and D.L. Shepelyanskii. Localization of dynamical chaos in quantum systems. *Plenum Publishing Corporation, translated from Izvestiya Vysshikh Uchebnykh Zavedenii, Radiofizika*, 29(9):1041–1049, 1986.

[10] D.L. Shepelyansky. Localization of diffusive excitation in multi-level systems. *Physica D: Nonlinear Phenomena*, 28(1):103 – 114, 1987.

[11] P. W. Anderson. Absence of diffusion in certain random lattices. *Phys. Rev.*, 109:1492–1505, Mar 1958.

[12] Shmuel Fishman, D. R. Grempel, and R. E. Prange. Chaos, quantum recurrences, and anderson localization. *Phys. Rev. Lett.*, 49:509–512, Aug 1982.

[13] D. R. Grempel, Shmuel Fishman, and R. E. Prange. Localization in an incommensurate potential: An exactly solvable model. *Phys. Rev. Lett.*, 49:833–836, Sep 1982.

[14] Shmuel Fishman, D. R. Grempel, and R. E. Prange. Localization in a d-dimensional incommensurate structure. *Phys. Rev. B*, 29:4272–4276, Apr 1984.

[15] D. R. Grempel, R. E. Prange, and Shmuel Fishman. Quantum dynamics of a nonintegrable system. *Phys. Rev. A*, 29:1639–1647, Apr 1984.

[16] D. L. Shepelyansky. Localization of quasienergy eigenfunctions in action space. *Phys. Rev. Lett.*, 56:677–680, Feb 1986.

[17] Marcel Filoche and Svitlana Mayboroda. Universal mechanism for anderson and weak localization. *Proceedings of the National Academy of Sciences*, 109(37):14761–14766, 2012.

[18] A.N. Kolmogorov. New metric invariant of transitive dynamical systems and endomorphisms of lebesgue spaces. *Doklady of Russian Academy of Sciences*, 119:861–864, 1958.

[19] Ya.G. Sinai. On the notion of entropy of a dynamical system. *Doklady of Russian Academy of Sciences*, 124:768–771, 1959.

[20] Ya. G. Sinai. *Introduction to Ergodic Theory*. Mathematical Notes (Book 18). Princeton University Press, 1977.

[21] Ya. B. Pesin. Characteristic lyapunov exponents and smooth ergodic theory. *Russian Mathematical Surveys*, 32(4):55–114, 1977. [Ya. B. Pesin, Characteristic Lyapunov exponents and smooth ergodic theory, *Uspekhi Mat. Nauk*, 32(4):55–112, 1977].

[22] Ricardo Mañé. A proof of pesin's formula. *Ergodic Theory and Dynamical Systems*, 1(1):95102, 1981.

[23] Luis Barreira and Yakov Pesin. *Nonuniform Hyperbolicity: Dynamics of Systems with Nonzero Lyapunov Exponents*. Encyclopedia of Mathematics and its Applications. Cambridge University Press, 2007.

[24] A. M. Lyapunov. The general problem of the stability of motion. *International Journal of Control*, 55(3):531–534, 1992. [A. M. Lyapunov, Obshchaya zadacha ob ustoichivosti dvizheniya, *Mathematical Society of Kharkov*, 1892].

[25] P. Cvitanović, R. Artuso, R. Mainieri, G. Tanner, and G. Vattay. *Lyapunov exponents*, chapter Lyapunov exponents, pages 115–124. `ChaosBook.org`, Niels Bohr Institute, Copenhagen, 2016.

[26] A. I. Larkin and Yu. N. Ovchinnikov. Quasiclassical method in the theory of superconductivity. *Sov. Phys. – JETP*, 28:1200, 1969. [Zh. Eksp. Teor. Fiz. **55**, 2262 (1969)].

[27] A. Kitaev. Hidden correlations in the hawking radiation and thermal noise. *KITP talk, http://online.kitp.ucsb.edu/ online/entangled15/kitaev/*, Nov 10, 2014.

[28] Juan Maldacena, Stephen H. Shenker, and Douglas Stanford. A bound on chaos. *J. High Energy Phys.*, 2016:106(8):1–17, 2016.

[29] O Bohigas, M J Giannoni, and C Schmit. Characterization of chaotic quantum spectra and universality of level fluctuation laws. *Phys. Rev. Lett.*, 52:1–4, Jan 1984.

[30] G Casati, F Valz-Gris, and I Guarnieri. On the connection between quantization of nonintegrable systems and statistical theory of spectra. *Lett. Nuovo Cimento*, 28(8):279–282, Jun 1980.

[31] Subir Sachdev. Bekenstein-hawking entropy and strange metals. *Phys. Rev. X*, 5:041025, Nov 2015.

[32] T. Araújo Lima, S. Rodríguez-Pérez, and F. M. de Aguiar. Ergodicity and quantum correlations in irrational triangular billiards. *Phys. Rev. E*, 87:062902, Jun 2013.

[33] Yakov Grigor'evich Sinai. Dynamical systems with elastic reflections. *Russian Math. Surv.*, 25(2):137–189, 1970.

[34] L A Bunimovich. On ergodic properties of certain billiards. *Functional Analysis and Its Applications*, 8(3):254–255, Jul 1974.

[35] L A Bunimovich. On the ergodic properties of nowhere dispersing billiards. *Commun. Math. Phys.*, 65(3):295–312, Oct 1979.

[36] Leonid Abramovich Bunimovich, Yakov Grigor'evich Sinai, and Nikolai Ivanovich Chernov. Statistical properties of two-dimensional hyperbolic billiards. *Russian Math. Surv.*, 46(4):47–106, 1991.

[37] G Benettin and J.-M Strelcyn. Numerical experiments on the free motion of a point mass moving in a plane convex region: Stochastic transition and entropy. *Phys. Rev. A*, 17:773–785, Feb 1978.

[38] Ch Dellago and H A Posch. Lyapunov exponents of systems with elastic hard collisions. *Phys. Rev. E*, 52:2401–2406, Sep 1995.

[39] Ofer Biham and Mark Kvale. Unstable periodic orbits in the stadium billiard. *Phys. Rev. A*, 46:6334–6339, Nov 1992.

[40] D.M. Basko, I.L. Aleiner, and B.L. Altshuler. Metalinsulator transition in a weakly interacting many-electron system with localized single-particle states. *Ann. Phys.*, 321(5):1126 – 1205, 2006.

[41] Robert Sims and Gunter Stolz. Many-body localization: Concepts and simple models. `arXiv:1312.0577`, 2012.

[42] I. V. Gornyi, A. D. Mirlin, and D. G. Polyakov. Interacting electrons in disordered wires: Anderson localization and low-t transport. *Phys. Rev. Lett.*, 95:206603, Nov 2005.

[43] Marko Žnidarič, Tomaž Prosen, and Peter Prelovšek. Many-body localization in the heisenberg xxz magnet in a random field. *Phys. Rev. B*, 77:064426, Feb 2008.

[44] Arijeet Pal and David A. Huse. Many-body localization phase transition. *Phys. Rev. B*, 82:174411, Nov 2010.

[45] Pedro Ponte, Z. Papić, François Huveneers, and Dmitry A. Abanin. Many-body localization in periodically driven systems. *Phys. Rev. Lett.*, 114:140401, Apr 2015.

[46] Achilleas Lazarides, Arnab Das, and Roderich Moessner. Fate of many-body localization under periodic driving. *Phys. Rev. Lett.*, 115:030402, Jul 2015.

[47] Rahul Nandkishore and David A. Huse. Many-body localization and thermalization in quantum statistical mechanics. *Ann. Rev. Cond. Mat. Phys.*, 6(1):15–38, 2015.

[48] Ehud Altman and Ronen Vosk. Universal dynamics and renormalization in many-body-localized systems. *Ann. Rev. Cond. Mat. Phys.*, 6(1):383–409, 2015.

[49] F. M. Izrailev and D. L. Shepelyansky. Quantum resonance for a rotator in a nonlinear periodic field. *Theor. Math. Phys.*, 43:553, 1980. [Teor. Mat. Fiz. **43**, 417 (1980)].

[50] B. V. Chirikov, F. M. Izrailev, and D. L. Shepelyansky. Dynamical stochasticity in classical and quantum mechanics. *Sov. Sci. Rev.*, Sec. C 2:209, 1981.

[51] F. L. Moore, J. C. Robinson, C. F. Bharucha, Bala Sundaram, and M. G. Raizen. Atom optics realization of the quantum δ-kicked rotor. *Phys. Rev. Lett.*, 75:4598–4601, Dec 1995.

[52] S. Adachi, M. Toda, and K. Ikeda. Quantum-classical correspondence in many-dimensional quantum chaos. *Phys. Rev. Lett.*, 61:659–661, Aug 1988.

[53] Kin'ya Takahashi. Distribution functions in classical and quantum mechanics. *Prog. Theor. Phys. Suppl.*, 98:109–156, 1989.

[54] T. Yukawa and N. Tsuda. Spontaneous decoherence in coupled quantum kicked rotators. *KEK-CP-022, KEK-PREPRINT-94-161, TIT-HEP-274*, 1994.

[55] N. Tsuda and T. Yukawa. Spontaneous decoherence in coupled quantum kicked rotators. `arXiv:chao-dyn/9711021`, Nov 1997.

[56] Masa-aki Sakagami. Emergence of classical properties from quantum theory. *Prog. Theor. Phys. Suppl.*, 116:393–401, 1994.

[57] Hiroto Kubotani, Takashi Okamura, and Masa-aki Sakagami. Quantum decoherence due to non-linear dynamics of environment. *Physica A*, 214(4):560 – 583, 1995.

[58] D. Weinmann, A. Müller-Groeling, J.-L. Pichard, and K. Frahm. $h/2e$ oscillations for correlated electron pairs in disordered mesoscopic rings. *Phys. Rev. Lett.*, 75:1598–1601, Aug 1995.

[59] Dima L. Shepelyansky and Pil Hun Song. Quantum ergodicity for electrons in two dimensions. *Annalen der Physik*, 8(7-9):665–673, 1999.

[60] D. L. Shepelyansky. Two electron view on metal-insulator transition in two dimensions. `arXiv:cond-mat/9905231`, May 1999.

[61] D. L. Shepelyansky. Three-dimensional anderson transition for two electrons in two dimensions. *Phys. Rev. B*, 61:4588–4591, Feb 2000.

[62] J. Lages and D. L. Shepelyansky. Delocalization of two-particle ring near the fermi level of 2d anderson model. *Eur. Phys. J. B*, 21(1):129–133, 2001.

[63] Hiroyuki Shima and Tsuneyoshi Nakayama. Orienting coupled quantum rotors by ultrashort laser pulses. *Phys. Rev. A*, 70:013401, Jul 2004.

[64] Zhao Wen-Lei and Jie Quan-Lin. Quantum to classical transition in a system of two coupled kicked rotors. *Comm. Theor. Phys.*, 51(3):465, 2009.

[65] Zhao Wen-Lei, Jie Quan-Lin, and Zhou Bo. Quantum to classical transition by a classically small interaction. *Comm. Theor. Phys.*, 54(2):247, 2010.

[66] T. Boness, K. Kudo, and T. S. Monteiro. Doubly excited ferromagnetic spin chain as a pair of coupled kicked rotors. *Phys. Rev. E*, 81:046201, Apr 2010.

[67] D. L. Shepelyansky. Some statistical properties of simple classically stochastic quantum systems. *Physica D*, 8(1):208 – 222, 1983.

[68] E. Ott, T. M. Antonsen, and J. D. Hanson. Effect of noise on time-dependent quantum chaos. *Phys. Rev. Lett.*, 53:2187–2190, Dec 1984.

[69] Doron Cohen. Destruction of localization due to coupling to a bath in the kicked-rotator problem. *Phys. Rev. A*, 43:639–645, Jan 1991.

[70] Doron Cohen. Quantum chaos, dynamical correlations, and the effect of noise on localization. *Phys. Rev. A*, 44:2292–2313, Aug 1991.

[71] Doron Cohen. Localization, dynamical correlations, and the effect of colored noise on coherence. *Phys. Rev. Lett.*, 67:1945–1948, Oct 1991.

[72] D Cohen. Noise, dissipation and the classical limit in the quantum kicked-rotator problem. *J. Phys. A*, 27(14):4805, 1994.

[73] K. Shiokawa and B. L. Hu. Decoherence, delocalization, and irreversibility in quantum chaotic systems. *Phys. Rev. E*, 52:2497–2509, Sep 1995.

[74] F. Borgonovi and D. L. Shepelyansky. Effect of noise for two interacting particles in a random potential. *Europhys. Lett.*, 35(7):517, 1996.

[75] Henning Schomerus and Eric Lutz. Controlled decoherence in a quantum lévy kicked rotator. *Phys. Rev. A*, 77:062113, Jun 2008.

[76] T Dittrich and R Graham. Long time behavior in the quantized standard map with dissipation. *Ann. Phys.*, 200(2):363 – 421, 1990.

[77] T. Dittrich and R. Graham. Continuous quantum measurements and chaos. *Phys. Rev. A*, 42:4647–4660, Oct 1990.

[78] S. Dyrting and G. J. Milburn. Dissipative nonlinear quantum dynamics in atomic optics. *Phys. Rev. A*, 51:3136–3147, Apr 1995.

[79] Francesco Benvenuto, Giulio Casati, Arkady S. Pikovsky, and Dima L. Shepelyansky. Manifestations of classical and quantum chaos in nonlinear wave propagation. *Phys. Rev. A*, 44:R3423–R3426, Sep 1991.

[80] D. L. Shepelyansky. Delocalization of quantum chaos by weak nonlinearity. *Phys. Rev. Lett.*, 70:1787–1790, Mar 1993.

[81] A. S. Pikovsky and D. L. Shepelyansky. Destruction of anderson localization by a weak nonlinearity. *Phys. Rev. Lett.*, 100:094101, Mar 2008.

[82] L Ermann and D L Shepelyansky. Destruction of anderson localization by nonlinearity in kicked rotator at different effective dimensions. *J. Phys. A*, 47(33):335101, 2014.

[83] B Mieck and R Graham. Boseeinstein condensate of kicked rotators. *J. Phys. A*, 37(44):L581, 2004.

[84] Ignacio García-Mata and Dima L. Shepelyansky. Delocalization induced by nonlinearity in systems with disorder. *Phys. Rev. E*, 79:026205, Feb 2009.

[85] S. Flach, D. O. Krimer, and Ch. Skokos. Universal spreading of wave packets in disordered nonlinear systems. *Phys. Rev. Lett.*, 102:024101, Jan 2009.

[86] Mario Mulansky, Karsten Ahnert, Arkady Pikovsky, and Dima L. Shepelyansky. Dynamical thermalization of disordered nonlinear lattices. *Phys. Rev. E*, 80:056212, Nov 2009.

[87] G. Gligorić, J. D. Bodyfelt, and S. Flach. Interactions destroy dynamical localization with strong and weak chaos. *Europhys. Lett.*, 96(3):30004, 2011.

[88] D. S. Brambila and A. Fratalocchi. Nonlinearly-enhanced energy transport in many dimensional quantum chaos. *Sci. Rep.*, 3:2359, Aug 2013.

[89] R. Graham and A.R. Kolovsky. Dynamical localization for a kicked atom in two standing waves. *Phys. Lett. A*, 222(12):47 – 49, 1996.

[90] B. G. Klappauf, W. H. Oskay, D. A. Steck, and M. G. Raizen. Observation of noise and dissipation effects on dynamical localization. *Phys. Rev. Lett.*, 81:1203–1206, Aug 1998.

[91] M. B. d'Arcy, R. M. Godun, M. K. Oberthaler, G. S. Summy, K. Burnett, and S. A. Gardiner. Approaching classicality in quantum accelerator modes through decoherence. *Phys. Rev. E*, 64:056233, Oct 2001.

[92] Chuanwei Zhang, Jie Liu, Mark G. Raizen, and Qian Niu. Transition to instability in a kicked bose-einstein condensate. *Phys. Rev. Lett.*, 92:054101, Feb 2004.

[93] G. J. Duffy, A. S. Mellish, K. J. Challis, and A. C. Wilson. Nonlinear atom-optical δ-kicked harmonic oscillator using a bose-einstein condensate. *Phys. Rev. A*, 70:041602, Oct 2004.

[94] Bryce Gadway, Jeremy Reeves, Ludwig Krinner, and Dominik Schneble. Evidence for a quantum-to-classical transition in a pair of coupled quantum rotors. *Phys. Rev. Lett.*, 110:190401, May 2013.

[95] Eyal Doron and Shmuel Fishman. Anderson localization for a two-dimensional rotor. *Phys. Rev. Lett.*, 60:867–870, Mar 1988.

[96] D. L. Shepelyansky. Coherent propagation of two interacting particles in a random potential. *Phys. Rev. Lett.*, 73:2607–2610, Nov 1994.

[97] Y. Imry. Coherent propagation of two interacting particles in a random potential. *Europhys. Lett.*, 30(7):405, 1995.

[98] K. Frahm, A. Müller-Groeling, J.-L. Pichard, and D. Weinmann. Scaling in interaction-assisted coherent transport. *Europhys. Lett.*, 31(3):169, 1995.

[99] F Borgonovi and D L Shepelyansky. Enhancement of localization length for two interacting kicked rotators. *Nonlinearity*, 8(5):877, 1995.

[100] Fausto Borgonovi and Dima L. Shepelyansky. Two interacting particles in an effective 2-3-d random potential. *J. Phys. I (France)*, 6(2):287–299, 1996.

[101] D. L. Shepelyansky. Interactions and localization: two interacting particles approach. `arXiv:cond-mat/9603086`, Mar 1996.

[102] Borzumehr Toloui. Quantum localization in momentum-space for two coupled kicked rotors. *Master thesis, Simon Fraser University,*, 2007.

[103] Borzumehr Toloui and Leslie E. Ballentine. Quantum localization for two coupled kicked rotors. `arXiv:0903.4632v2`, Oct 2009.

[104] Aydin Cem Keser, Sriram Ganeshan, Gil Refael, and Victor Galitski. Dynamical many-body localization in an integrable model. *Phys. Rev. B*, 94:085120, Aug 2016.

[105] D U Matrasulov and G M Milibaeva. The relativistic quantum periodically driven rotator. *Phys. Scr.*, 68(4):215, 2003.

[106] D. U. Matrasulov, G. M. Milibaeva, U. R. Salomov, and Bala Sundaram. Relativistic kicked rotor. *Phys. Rev. E*, 72:016213, Jul 2005.

[107] A. A. Chernikov, T. Tél, G. Vattay, and G. M. Zaslavsky. Chaos in the relativistic generalization of the standard map. *Phys. Rev. A*, 40:4072–4076, Oct 1989.

[108] R. E. Prange, D. R. Grempel, and Shmuel Fishman. Solvable model of quantum motion in an incommensurate potential. *Phys. Rev. B*, 29:6500–6512, Jun 1984.

[109] M. V. Berry. Incommensurability in an exactly-soluble quantal and classical model for a kicked rotator. *Physica D*, 10(3):369 – 378, 1984.

[110] Barry Simon. Almost periodic schrdinger operators iv. the maryland model. *Ann. Phys.*, 159(1):157 – 183, 1985.

[111] Qifang Zhao, Cord A. Müller, and Jiangbin Gong. Quantum and classical superballistic transport in a relativistic kicked-rotor system. *Phys. Rev. E*, 90:022921, Aug 2014.

[112] L. Hufnagel, R. Ketzmerick, T. Kottos, and T. Geisel. Superballistic spreading of wave packets. *Phys. Rev. E*, 64:012301, Jun 2001.

[113] Zhenjun Zhang, Peiqing Tong, Jiangbin Gong, and Baowen Li. Quantum hyperdiffusion in one-dimensional tight-binding lattices. *Phys. Rev. Lett.*, 108:070603, Feb 2012.

[114] S. Stützer, T. Kottos, A. Tünnermann, S. Nolte, D. N. Christodoulides, and A. Szameit. Superballistic growth of the variance of optical wave packets. *Opt. Lett.*, 38(22):4675–4678, Nov 2013.

[115] Stefano Lubini, Octavi Boada, Yasser Omar, and Francesco Piazza. Transport of quantum excitations coupled to spatially extended nonlinear many-body systems. *New Journal of Physics*, 17(11):113030, 2015.

[116] R. Scharf. Kicked rotator for a spin-1/2 particle. *J. Phys. A*, 22(19):4223, 1989.

[117] M. Thaha and R. Blümel. Nonuniversality of the localization length in a quantum chaotic system. *Phys. Rev. Lett.*, 72:72–75, Jan 1994.

[118] A. Ossipov, M. D. Basko, and E. V. Kravtsov. A super-ohmic energy absorption in driven quantum chaotic systems. *Eur. Phys. J. B*, 42(4):457–460, 2004.

[119] J. P. Dahlhaus, J. M. Edge, J. Tworzydło, and C. W. J. Beenakker. Quantum hall effect in a one-dimensional dynamical system. *Phys. Rev. B*, 84:115133, Sep 2011.

[120] Yu Chen and Chushun Tian. Planck's quantum-driven integer quantum hall effect in chaos. *Phys. Rev. Lett.*, 113:216802, Nov 2014.

[121] Chushun Tian, Yu Chen, and Jiao Wang. Emergence of integer quantum hall effect from chaos. *Phys. Rev. B*, 93:075403, Feb 2016.

[122] A. L. Figotin and L. A. Pastur. An exactly solvable model of a multidimensional incommensurate structure. *Comm. Math. Phys.*, 95(4):401–425, 1984.

[123] Achilleas Lazarides, Arnab Das, and Roderich Moessner. Periodic thermodynamics of isolated quantum systems. *Phys. Rev. Lett.*, 112:150401, Apr 2014.

[124] Dmitry A. Abanin, Wojciech De Roeck, and Franois Huveneers. Theory of many-body localization in periodically driven systems. *Annals of Physics*, 372:1 – 11, 2016.

[125] Pedro Ponte, Anushya Chandran, Z. Papić, and Dmitry A. Abanin. Periodically driven ergodic and many-body localized quantum systems. *Ann. Phys.*, 353:196 – 204, 2015.

[126] M. B. d'Arcy, R. M. Godun, M. K. Oberthaler, D. Cassettari, and G. S. Summy. Quantum enhancement of momentum diffusion in the delta-kicked rotor. *Phys. Rev. Lett.*, 87:074102, Jul 2001.

[127] Julien Chabé, Gabriel Lemarié, Benoît Grémaud, Dominique Delande, Pascal Szriftgiser, and Jean Claude Garreau. Experimental observation of the anderson metal-insulator transition with atomic matter waves. *Phys. Rev. Lett.*, 101:255702, Dec 2008.

[128] Efim B. Rozenbaum and Victor Galitski. Dynamical localization of coupled relativistic kicked rotors. *Phys. Rev. B*, 95:064303, Feb 2017.

[129] Simone Notarnicola, Fernando Iemini, Davide Rossini, Rosario Fazio, Alessandro Silva, and Angelo Russomanno. From localization to anomalous diffusion in the dynamics of coupled kicked rotors. *Phys. Rev. E*, 97:022202, Feb 2018.

[130] P. Qin, A. Andreanov, H. C. Park, and S. Flach. Interacting ultracold atomic kicked rotors: loss of dynamical localization. *Sci. Rep.*, 7:41139, 2017.

[131] L. A. Toikka and A. Andreanov. Many-body dynamical localisation of coupled quantum kicked rotors. *arXiv:1901.09362*, 2019.

[132] Immanuel Bloch, Jean Dalibard, and Wilhelm Zwerger. Many-body physics with ultracold gases. *Rev. Mod. Phys.*, 80:885–964, Jul 2008.

[133] Luca DAlessio and Anatoli Polkovnikov. Many-body energy localization transition in periodically driven systems. *Ann. Phys.*, 333(0):19 – 33, 2013.

[134] Marin Bukov, Luca DAlessio, and Anatoli Polkovnikov. Universal high-frequency behavior of periodically driven systems: from dynamical stabilization to floquet engineering. *Advances in Physics*, 64(2):139226, Mar 2015.

[135] Roberta Citro, Emanuele G. Dalla Torre, Luca DAlessio, Anatoli Polkovnikov, Mehrtash Babadi, Takashi Oka, and Eugene Demler. Dynamical stability of a many-body kapitza pendulum. *Ann. Phys.*, 360:694 – 710, 2015.

[136] Atanu Rajak, Itzhack Dana, and Emanuele G. Dalla Torre. Characterizations of prethermal states in periodically driven many-body systems with unbounded chaotic diffusion. *Phys. Rev. B*, 100:100302(R), Sep 2019.

[137] T. Giamarchi. *Quantum Physics in One Dimension*. International Series of Monographs on Physics. Clarendon Press, 2003.

[138] A.O. Gogolin, A.A. Nersesyan, and A.M. Tsvelik. *Bosonization and Strongly Correlated Systems*. Cambridge University Press, 2004.

[139] Bruno Bertini, Mario Collura, Jacopo De Nardis, and Maurizio Fagotti. Transport in out-of-equilibrium xxz chains: Exact profiles of charges and currents. *Phys. Rev. Lett.*, 117:207201, Nov 2016.

[140] Olalla A. Castro-Alvaredo, Benjamin Doyon, and Takato Yoshimura. Emergent hydrodynamics in integrable quantum systems out of equilibrium. *Phys. Rev. X*, 6:041065, Dec 2016.

[141] Elliott H. Lieb and Werner Liniger. Exact analysis of an interacting bose gas. i. the general solution and the ground state. *Phys. Rev.*, 130:1605–1616, May 1963.

[142] Elliott H. Lieb. Exact analysis of an interacting bose gas. ii. the excitation spectrum. *Phys. Rev.*, 130:1616–1624, May 1963.

[143] M. Olshanii. Atomic scattering in the presence of an external confinement and a gas of impenetrable bosons. *Phys. Rev. Lett.*, 81:938–941, Aug 1998.

[144] V. Dunjko, V. Lorent, and M. Olshanii. Bosons in cigar-shaped traps: Thomas-fermi regime, tonks-girardeau regime, and in between. *Phys. Rev. Lett.*, 86:5413–5416, Jun 2001.

[145] M. Gaudin and J.-S. Caux. *The Bethe Wavefunction*. Cambridge University Press, 2014.

[146] V. E. Korepin, N. M. Bogoliubov, and A. G. Izergin. *Quantum Inverse Scattering Method and Correlation Functions*. Cambridge University Press, 1993.

[147] Márton Kormos, Aditya Shashi, Yang-Zhi Chou, Jean-Sébastien Caux, and Adilet Imambekov. Interaction quenches in the one-dimensional bose gas. *Phys. Rev. B*, 88:205131, Nov 2013.

[148] Jacopo De Nardis, Bram Wouters, Michael Brockmann, and Jean-Sébastien Caux. Solution for an interaction quench in the lieb-liniger bose gas. *Phys. Rev. A*, 89:033601, Mar 2014.

[149] Jean-Sébastien Caux and Robert M. Konik. Constructing the generalized gibbs ensemble after a quantum quench. *Phys. Rev. Lett.*, 109:175301, Oct 2012.

[150] Lewi Tonks. The complete equation of state of one, two and three-dimensional gases of hard elastic spheres. *Phys. Rev.*, 50:955–963, Nov 1936.

[151] M. Girardeau. Relationship between Systems of Impenetrable Bosons and Fermions in One Dimension. *J. Math. Phys.*, 1:516–523, November 1960.

[152] V. I. Yukalov and M. D. Girardeau. Fermi-Bose mapping for one-dimensional Bose gases. *Laser Phys. Lett.*, 2(8):375–382, Jul 2005.

[153] R. Pezer and H. Buljan. Momentum Distribution Dynamics of a Tonks-Girardeau Gas: Bragg Reflections of a Quantum Many-Body Wave Packet. *Phys. Rev. Lett.*, 98(24):240403, June 2007.

[154] A.G. Izergin and V.E. Korepin. The pauli principle for one-dimensional bosons and the algebraic bethe ansatz. *J. Math. Sci.*, 34:1933, 1986.

[155] F. D. M. Haldane. Effective harmonic-fluid approach to low-energy properties of one-dimensional quantum fluids. *Phys. Rev. Lett.*, 47:1840–1843, Dec 1981.

[156] Colin Rylands, Efim Rozenbaum, Victor Galitski, and Robert Konik. Many-body dynamical localization in a kicked lieb-liniger gas. `arXiv:1904.09473`, 2019.

[157] Benjamin Doyon, Jérôme Dubail, Robert Konik, and Takato Yoshimura. Large-scale description of interacting one-dimensional bose gases: Generalized hydrodynamics supersedes conventional hydrodynamics. *Phys. Rev. Lett.*, 119:195301, Nov 2017.

[158] E. Wigner. On the quantum correction for thermodynamic equilibrium. *Phys. Rev.*, 40:749–759, Jun 1932.

[159] Benjamin Doyon and Takato Yoshimura. A note on generalized hydrodynamics: inhomogeneous fields and other concepts. *SciPost Phys.*, 2:014, 2017.

[160] Ricardo Lima and Dima Shepelyansky. Fast delocalization in a model of quantum kicked rotator. *Phys. Rev. Lett.*, 67:1377–1380, Sep 1991.

[161] F. Borgonovi and D.L. Shepelyansky. Particle propagation in a random and quasi-periodic potential. *Physica D*, 109(1):24 – 31, 1997.

[162] Vir B. Bulchandani, Romain Vasseur, Christoph Karrasch, and Joel E. Moore. Solvable hydrodynamics of quantum integrable systems. *Phys. Rev. Lett.*, 119:220604, Nov 2017.

[163] Miłosz Panfil and Jacek Pawełczyk. Linearized regime of the generalized hydrodynamics with diffusion. *arXiv:1905.06257*, 2019.

[164] Daniel Alonso, A. Ruiz, and I. de Vega. Polygonal billiards and transport: Diffusion and heat conduction. *Phys. Rev. E*, 66:066131, Dec 2002.

[165] Baowen Li, Giulio Casati, and Jiao Wang. Heat conductivity in linear mixing systems. *Phys. Rev. E*, 67:021204, Feb 2003.

[166] David P. Sanders and Hernán Larralde. Occurrence of normal and anomalous diffusion in polygonal billiard channels. *Phys. Rev. E*, 73:026205, Feb 2006.

[167] Owen G Jepps and Lamberto Rondoni. Thermodynamics and complexity of simple transport phenomena. *Journal of Physics A: Mathematical and General*, 39(6):1311–1338, jan 2006.

[168] Rodolfo A. Jalabert, Harold U. Baranger, and A. Douglas Stone. Conductance fluctuations in the ballistic regime: A probe of quantum chaos? *Phys. Rev. Lett.*, 65:2442–2445, Nov 1990.

[169] Harold U. Baranger, David P. DiVincenzo, Rodolfo A. Jalabert, and A. Douglas Stone. Classical and quantum ballistic-transport anomalies in microjunctions. *Phys. Rev. B*, 44:10637–10675, Nov 1991.

[170] G. A. Luna-Acosta, A. A. Krokhin, M. A. Rodríguez, and P. H. Hernández-Tejeda. Classical chaos and ballistic transport in a mesoscopic channel. *Phys. Rev. B*, 54:11410–11416, Oct 1996.

[171] Iván F. Herrera-González, Gabriel Arroyo-Correa, Alberto Mendoza-Suárez, and Eduardo S. Tututi. Study of the resistivity in a channel with dephased ripples. *Int. J. Mod. Phys. B*, 25(05):683–698, 2011.

[172] G. A. Luna-Acosta, A. Krokhin, M. A. Rodriguez-Meza, and P. H. Hernandez-Tejeda. *Ballistic transport properties of a 2D rippled mesoscopic channel: Classical regime.* World Scientific, Singapore, 1995.

[173] G. A. Luna-Acosta, Kyungsun Na, L. E. Reichl, and A. Krokhin. Band structure and quantum poincaré sections of a classically chaotic quantum rippled channel. *Phys. Rev. E*, 53:3271–3283, Apr 1996.

[174] J. A. Méndez-Bermúdez, G. A. Luna-Acosta, P. Šeba, and K. N. Pichugin. Chaotic waveguide-based resonators for microlasers. *Phys. Rev. B*, 67:161104, Apr 2003.

[175] O. Bendix, J.A. Mndez-Bermdez, G.A. Luna-Acosta, U. Kuhl, and H.-J. Stckmann. Design of beam splitters and microlasers using chaotic waveguides. *Microelectronics Journal*, 36(3):285 – 288, 2005. Low Dimensional Structures and Devices Conference.

[176] Marcelo Leite Lyra, Svitlana Mayboroda, and Marcel Filoche. Dual hidden landscapes in anderson localization on discrete lattices, 2014.

[177] Gautier Lefebvre, Alexane Gondel, Marc Dubois, Michael Atlan, Florian Feppon, Aimé Labbé, Camille Gillot, Alix Garelli, Maxence Ernoult, Svitlana Mayboroda, Marcel Filoche, and Patrick Sebbah. One single static measurement predicts wave localization in complex structures. *Phys. Rev. Lett.*, 117:074301, Aug 2016.

[178] Douglas N. Arnold, Guy David, David Jerison, Svitlana Mayboroda, and Marcel Filoche. Effective confining potential of quantum states in disordered media. *Phys. Rev. Lett.*, 116:056602, Feb 2016.

[179] Douglas N. Arnold, Guy. David, Marcel. Filoche, David. Jerison, and Svitlana. Mayboroda. Computing spectra without solving eigenvalue problems. *SIAM Journal on Scientific Computing*, 41(1):B69–B92, 2019.

[180] Douglas N. Arnold, Guy David, Marcel Filoche, David Jerison, and Svitlana Mayboroda. Localization of eigenfunctions via an effective potential. *Communications in Partial Differential Equations*, 44(11):1186–1216, 2019.

[181] Guy David, Marcel Filoche, and Svitlana Mayboroda. The landscape law for the integrated density of states, 2019.

[182] Heinrich P Baltes and E R Hilf. *Spectra of finite systems.* Mannheim: Bibliographisches Institut, 1976.

[183] Christopher Jarzynski. Private Communication, 2019.

[184] G. Casati, B. V. Chirikov, I. Guarneri, and D. L. Shepelyansky. Dynamical stability of quantum "chaotic" motion in a hydrogen atom. *Phys. Rev. Lett.*, 56:2437–2440, Jun 1986.

[185] M.V. Berry, N.L. Balazs, M. Tabor, and A. Voros. Quantum maps. *Ann. Phys.*, 122(1):26 – 63, 1979.

[186] B. V. Chirikov, F. M. Izrailev, and D. L. Shepelyansky. Quantum chaos: Localization vs. ergodicity. *Physica D*, 33(1):77 – 88, 1988.

[187] Michael V Berry. Semiclassical mechanics of regular and irregular motion. *Les Houches lecture series*, 36:171–271, 1983.

[188] F. Haake, M. Kuś, and R. Scharf. Classical and quantum chaos for a kicked top. *Z. Phys. B*, 65(3):381–395, 1987.

[189] M. Toda and K. Ikeda. Quantal lyapunov exponent. *Phys. Lett. A*, 124(3):165 – 169, 1987.

[190] Fritz Haake, Harald Wiedemann, and Karol Życzkowski. Lyapunov exponents from quantum dynamics. *Ann. Phys.*, 504(7):531–539, 1992.

[191] Robert Alicki, Danuta Makowiec, and Wiesław Miklaszewski. Quantum chaos in terms of entropy for a periodically kicked top. *Phys. Rev. Lett.*, 77:838–841, Jul 1996.

[192] I. L. Aleiner and A. I. Larkin. Divergence of classical trajectories and weak localization. *Phys. Rev. B*, 54:14423–14444, Nov 1996.

[193] I. L. Aleiner and A. I. Larkin. Role of divergence of classical trajectories in quantum chaos. *Phys. Rev. E*, 55:R1243–R1246, Feb 1997.

[194] Oded Agam, Igor Aleiner, and Anatoly Larkin. Shot noise in chaotic systems: "classical" to quantum crossover. *Phys. Rev. Lett.*, 85:3153–3156, Oct 2000.

[195] Brian Swingle, Gregory Bentsen, Monika Schleier-Smith, and Patrick Hayden. Measuring the scrambling of quantum information. *Phys. Rev. A*, 94:040302, Oct 2016.

[196] Norman Y Yao, Fabian Grusdt, Brian Swingle, Mikhail D Lukin, Dan M Stamper-Kurn, Joel E Moore, and Eugene A Demler. Interferometric approach to probing fast scrambling. `arXiv:1607.01801`, 2016.

[197] Yichen Huang, Yong-Liang Zhang, and Xie Chen. Out-of-time-ordered correlators in many-body localized systems. *Ann. Phys.*, 529(7):1600318, 2017.

[198] Yu Chen. Quantum logarithmic butterfly in many body localization. `arXiv:1608.02765`, 2016.

[199] Brian Swingle and Debanjan Chowdhury. Slow scrambling in disordered quantum systems. *Phys. Rev. B*, 95:060201, Feb 2017.

[200] Ruihua Fan, Pengfei Zhang, Huitao Shen, and Hui Zhai. Out-of-time-order correlation for many-body localization. *Sci. Bull.*, 62(10):707 – 711, 2017.

[201] F. M. Izrailev and D. L. Shepelyansky. Quantum resonance for a rotator in a nonlinear periodic field. *Sov. Phys. – Dokl.*, 24:996, 1979. [Dok. Akad. Nauk SSSR **249**, 1103 (1979)].

[202] C. Tian, A. Kamenev, and A. Larkin. Weak dynamical localization in periodically kicked cold atomic gases. *Phys. Rev. Lett.*, 93:124101, Sep 2004.

[203] W. K. Hensinger, H. Haffner, A. Browaeys, N. R. Heckenberg, K. Helmerson, C. McKenzie, G. J. Milburn, W. D. Phillips, S. L. Rolston, H. Rubinsztein-Dunlop, and B. Upcroft. Dynamical tunnelling of ultracold atoms. *Nature*, 412(6842):52–55, Jul 2001.

[204] Daniel A. Steck, Windell H. Oskay, and Mark G. Raizen. Observation of chaos-assisted tunneling between islands of stability. *Science*, 293(5528):274–278, 2001.

[205] Gabriela B. Lemos, Rafael M. Gomes, Stephen P. Walborn, Paulo H. Souto Ribeiro, and Fabricio Toscano. Experimental observation of quantum chaos in a beam of light. *Nat. Commun.*, 3:1211, Nov 2012.

[206] Jonas Larson, Brandon M. Anderson, and Alexander Altland. Chaos-driven dynamics in spin-orbit-coupled atomic gases. *Phys. Rev. A*, 87:013624, Jan 2013.

[207] Asher Peres. Stability of quantum motion in chaotic and regular systems. *Phys. Rev. A*, 30:1610–1615, Oct 1984.

[208] H.M Pastawski, P.R Levstein, G Usaj, J Raya, and J Hirschinger. A nuclear magnetic resonance answer to the boltzmannloschmidt controversy? *Physica A*, 283(1-2):166 – 170, 2000.

[209] Ph. Jacquod, P.G. Silvestrov, and C.W.J. Beenakker. Golden rule decay versus lyapunov decay of the quantum loschmidt echo. *Phys. Rev. E*, 64:055203, Oct 2001.

[210] Rodolfo A. Jalabert and Horacio M. Pastawski. Environment-independent decoherence rate in classically chaotic systems. *Phys. Rev. Lett.*, 86:2490–2493, Mar 2001.

[211] F. M. Cucchietti, C. H. Lewenkopf, E. R. Mucciolo, H. M. Pastawski, and R. O. Vallejos. Measuring the lyapunov exponent using quantum mechanics. *Phys. Rev. E*, 65:046209, Apr 2002.

[212] F. M. Cucchietti, H. M. Pastawski, and D. A. Wisniacki. Decoherence as decay of the loschmidt echo in a lorentz gas. *Phys. Rev. E*, 65:045206, Apr 2002.

[213] S. Chaudhury, A. Smith, B. E. Anderson, S. Ghose, and P. S. Jessen. Quantum signatures of chaos in a kicked top. *Nature*, 461(7265):768–771, Oct 2009.

[214] Ignacio García-Mata and Diego A Wisniacki. Loschmidt echo in quantum maps: the elusive nature of the lyapunov regime. *J. Phys. A*, 44(31):315101, 2011.

[215] Shmuel Fishman and Mark Srednicki. Private Collaboration, 2019.

[216] M C Gutzwiller. *Chaos in Classical and Quantum Mechanics*. Interdisciplinary Applied Mathematics. Springer New York, 1991.

[217] Michael V Berry. Semiclassical theory of spectral rigidity. *Proc. R. Soc. Lond. A*, 400(1819):229–251, 1985.

[218] A. V. Andreev, O. Agam, B. D. Simons, and B. L. Altshuler. Quantum chaos, irreversible classical dynamics, and random matrix theory. *Phys. Rev. Lett.*, 76:3947–3950, May 1996.

[219] A V Andreev, B D Simons, O Agam, and B L Altshuler. Semiclassical field theory approach to quantum chaos. *Nucl. Phys. B*, 482(3):536 – 566, 1996.

[220] Alexander Altland, Sven Gnutzmann, Fritz Haake, and Tobias Micklitz. A review of sigma models for quantum chaotic dynamics. *Rep. Prog. Phys.*, 78(8):086001, 2015.

[221] E B Stechel and E J Heller. Quantum ergodicity and spectral chaos. *Ann. Rev. Phys. Chern.*, 35(1):563–589, 1984.

[222] Steve Zelditch. Quantum ergodicity and mixing. *arXiv:math-ph/0503026*, 2005.

[223] Steve Zelditch. Recent developments in mathematical quantum chaos. *Current Developments in Mathematics*, 2009:115–204, 2010.

[224] M V Berry. Regular and irregular semiclassical wavefunctions. *J Phys A*, 10(12):2083, 1977.

[225] M V Berry. Statistics of nodal lines and points in chaotic quantum billiards: perimeter corrections, fluctuations, curvature. *J Phys A*, 35(13):3025, 2002.

[226] R. Blümel and U. Smilansky. Classical irregular scattering and its quantum-mechanical implications. *Phys. Rev. Lett.*, 60:477–480, Feb 1988.

[227] G. Casati, I. Guarneri, and D.L. Shepelyansky. Classical chaos, quantum localization and fluctuations: A unified view. *Physica A*, 163(1):205 – 214, 1990.

[228] Asher Peres. *Quantum Theory: Concepts and Methods*. Kluwer, Dordrecht, 1995.

[229] Diego A. Wisniacki, Eduardo G. Vergini, Horacio M. Pastawski, and Fernando M. Cucchietti. Sensitivity to perturbations in a quantum chaotic billiard. *Phys. Rev. E*, 65:055206, May 2002.

[230] Efim B Rozenbaum, Sriram Ganeshan, and Victor Galitski. Lyapunov exponent and out-of-time-ordered correlator's growth rate in a chaotic system. *Phys. Rev. Lett.*, 118:086801, Feb 2017.

[231] S.V. Syzranov, A.V. Gorshkov, and V.M. Galitski. Interaction-induced transition in the quantum chaotic dynamics of a disordered metal. *Annals of Physics*, 405:1 – 13, 2019.

[232] Igor L Aleiner, Lara Faoro, and Lev B Ioffe. Microscopic model of quantum butterfly effect: Out-of-time-order correlators and traveling combustion waves. *Ann. Phys.*, 375:378 – 406, 2016.

[233] Juan Maldacena and Douglas Stanford. Remarks on the sachdev-ye-kitaev model. *Phys. Rev. D*, 94:106002, Nov 2016.

[234] Dmitry Bagrets, Alexander Altland, and Alex Kamenev. Sachdevyekitaev model as liouville quantum mechanics. *Nucl. Phys. B*, 911:191 – 205, 2016.

[235] Jordan Cotler, Nicholas Hunter-Jones, Junyu Liu, and Beni Yoshida. Chaos, complexity, and random matrices. *J. High Energy Phys.*, 2017(11):48, Nov 2017.

[236] Guy Gur-Ari, Masanori Hanada, and Stephen H. Shenker. Chaos in classical d0-brane mechanics. *Journal of High Energy Physics*, 2016(2):91, 2016.

[237] Masanori Hanada, Hidehiko Shimada, and Masaki Tezuka. Universality in chaos: Lyapunov spectrum and random matrix theory. *Phys. Rev. E*, 97:022224, Feb 2018.

[238] Steven W McDonald and Allan N Kaufman. Spectrum and eigenfunctions for a hamiltonian with stochastic trajectories. *Phys. Rev. Lett.*, 42:1189–1191, Apr 1979.

[239] Akira Shudo and Yasushi Shimizu. Universality and nonuniversality of level statistics in the stadium billiard. *Phys. Rev. A*, 42:6264–6267, Nov 1990.

[240] Fausto Borgonovi, Giulio Casati, and Baowen Li. Diffusion and localization in chaotic billiards. *Phys. Rev. Lett.*, 77:4744–4747, Dec 1996.

[241] H Alt, C Dembowski, H.-D Gräf, R Hofferbert, H Rehfeld, A Richter, and C Schmit. Experimental versus numerical eigenvalues of a bunimovich stadium billiard: A comparison. *Phys. Rev. E*, 60:2851–2857, Sep 1999.

[242] H.-D Gräf, H. L. Harney, H. Lengeler, C. H. Lewenkopf, C. Rangacharyulu, A. Richter, P. Schardt, and H. A. Weidenmüller. Distribution of eigenmodes in a superconducting stadium billiard with chaotic dynamics. *Phys. Rev. Lett.*, 69:1296–1299, Aug 1992.

[243] M Sieber, U Smilansky, S C Creagh, and R G Littlejohn. Non-generic spectral statistics in the quantized stadium billiard. *J Phys A*, 26(22):6217, 1993.

[244] Vincent Heuveline. On the computation of a very large number of eigenvalues for selfadjoint elliptic operators by means of multigrid methods. *J. Comput. Phys.*, 184(1):321 – 337, 2003.

[245] A Y Abul-Magd, G Akemann, and P Vivo. Superstatistical generalizations of wishartlaguerre ensembles of random matrices. *J. Phys. A: Math. Theor.*, 42(17):175207, 2009.

[246] Jordan S. Cotler, Dawei Ding, and Geoffrey R. Penington. Out-of-time-order operators and the butterfly effect. *Ann. Phys.*, 396:318 – 333, 2018.

[247] J E Moyal. Quantum mechanics as a statistical theory. *Mathematical Proceedings of the Cambridge Philosophical Society*, 45(1):99124, 1949.

[248] Wojciech Hubert Zurek and Juan Pablo Paz. Decoherence, chaos, and the second law. *Phys. Rev. Lett.*, 72:2508–2511, Apr 1994.

[249] Koji Hashimoto, Keiju Murata, and Ryosuke Yoshii. Out-of-time-order correlators in quantum mechanics. *J. High Energy Phys.*, 2017(10):138, Oct 2017.

[250] Č Lozej. Private Communication, 2018.

[251] Brian R Hunt and Edward Ott. Defining chaos. *Chaos: An Interdisciplinary Journal of Nonlinear Science*, 25(9):097618, 2015.

[252] George M. Zaslavsky. Stochasticity in quantum systems. *Phys. Rep.*, 80(3):157 – 250, 1981.

[253] Yan Gu. Evidences of classical and quantum chaos in the time evolution of nonequilibrium ensembles. *Physics Letters A*, 149(2):95 – 100, 1990.

[254] Wojciech Hubert Zurek and Juan Pablo Paz. Quantum chaos: a decoherent definition. *Physica D: Nonlinear Phenomena*, 83(1):300 – 308, 1995.

[255] Wojciech H. Zurek. Decoherence, chaos, quantum-classical correspondence, and the algorithmic arrow of time. *Physica Scripta*, T76(1):186, 1998.

[256] Michael Berry. Chaos and the semiclassical limit of quantum mechanics (is the moon there when somebody looks?). In Robert John Russell, Philip Clayton, Kirk Wegter-McNelly, and John Polkinghorne, editors, *Quantum Mechanics*, Scientific Perspectives on Divine Action, pages 41–54. CTNS/Vatican Observatory, 2001.

[257] M. Schlosshauer. Classicality, the ensemble interpretation, anddecoherence: Resolving the hyperion dispute. *Found. Phys.*, 38(9):796–803, Sep 2008.

[258] N. Wiebe and L. E. Ballentine. Quantum mechanics of hyperion. *Phys. Rev. A*, 72:022109, Aug 2005.

[259] Leslie Ballentine. Classicality without decoherence: A reply to schlosshauer. *Found. Phys.*, 38(10):916–922, Oct 2008.

[260] Efim B. Rozenbaum, Leonid A. Bunimovich, and Victor Galitski. Early-time exponential instabilities in non-chaotic quantum systems. `arXiv:1902.05466`, 2019.

[261] L. P. Gor'kov and G. M. Eliashberg. Minute metallic particles in an electromagnetic field. *Sov. Phys. – JETP*, 21:940, 1965. [Zh. Eksp. Teor. Fiz. **48**, 1407 (1965)].

[262] K. B. Efetov. Supersymmetry and theory of disordered metals. *Advances in Physics*, 32(1):53–127, 1983.

[263] B. L. Al'tshuler and B. I. Shklovskii. Repulsion of energy levels and conductivity of small metal samples. *Sov. Phys. – JETP*, 64:127, 1986. [Zh. Eksp. Teor. Fiz. **91**, 220 (1986)].

[264] E. Doron, U. Smilansky, and T. Dittrich. The domino billiard. *Physica B*, 179(1):1 – 5, 1992.

[265] R.A. Serota. Chaotic quantum billiards in magnetic field: A semiclassical analysis of mesoscopic effects. *Solid State Commun.*, 84(8):843 – 845, 1992.

[266] Nathan Argaman, Yoseph Imry, and Uzy Smilansky. Semiclassical analysis of spectral correlations in mesoscopic systems. *Phys. Rev. B*, 47:4440–4457, Feb 1993.

[267] Gilles Montambaux. *Spectral Fluctuations in Disordered Metals*, page 387. Les Houches lecture series, session LXIII. Elsevier, 1997.

[268] Katsuhiro Nakamura and Takahisa Harayama. *Quantum Chaos and Quantum Dots*. Mesoscopic Physics and Nanotechnology. Oxford University Press, 2004.

[269] A. N. Zemlyakov and A. B. Katok. Topological transitivity of billiards in polygons. *Math. Notes Acad. Sci. USSR*, 18(2):760–764, 1975. [Mat. Zametki **18** 291 (1975)].

[270] Carlo Boldrighini, Michael Keane, and Federico Marchetti. Billiards in polygons. *Ann. Probab.*, 6(4):532–540, 08 1978.

[271] Mark Bolding. *Topics in Dynamics: First Passage Probabilities and Chaotic Properties of the Physical Wind-Tree Model*. PhD thesis, School of Mathematics, Georgia Institute of Technology, Atlanta, GA 30332, USA., 2018.

[272] L. A. Bunimovich. Physical versus mathematical billiards: From regular dynamics to chaos and back. *Chaos: An Interdisciplinary Journal of Nonlinear Science*, 29(9):091105, 2019.

[273] Daniel A. Roberts, Douglas Stanford, and Leonard Susskind. Localized shocks. *J. High Energy Phys.*, 2015(3):51, Mar 2015.

[274] Daniel A. Roberts and Brian Swingle. Lieb-robinson bound and the butterfly effect in quantum field theories. *Phys. Rev. Lett.*, 117:091602, Aug 2016.

[275] Márk Mezei and Douglas Stanford. On entanglement spreading in chaotic systems. *J. High Energy Phys.*, 2017(5):65, May 2017.

[276] Vedika Khemani, David A. Huse, and Adam Nahum. Velocity-dependent lyapunov exponents in many-body quantum, semiclassical, and classical chaos. *Phys. Rev. B*, 98:144304, Oct 2018.

[277] Shenglong Xu and Brian Swingle. Accessing scrambling using matrix product operators. `arXiv:1802.00801`, 2018.

[278] Jorge Chávez-Carlos, B. López-del Carpio, Miguel A. Bastarrachea-Magnani, Pavel Stránský, Sergio Lerma-Hernández, Lea F. Santos, and Jorge G. Hirsch. Quantum and classical lyapunov exponents in atom-field interaction systems. *Phys. Rev. Lett.*, 122:024101, Jan 2019.

[279] Efim B. Rozenbaum, Sriram Ganeshan, and Victor Galitski. Universal level statistics of the out-of-time-ordered operator. *Phys. Rev. B*, 100:035112, Jul 2019.

[280] Giulio Casati and Tomaz Prosen. Mixing property of triangular billiards. *Phys. Rev. Lett.*, 83:4729–4732, Dec 1999.

[281] Arul Lakshminarayan. Out-of-time-ordered correlator in the quantum bakers map and truncated unitary matrices. *Phys. Rev. E*, 99:012201, Jan 2019.

[282] T. Prosen. General relation between quantum ergodicity and fidelity of quantum dynamics. *Phys. Rev. E*, 65:036208, Feb 2002.

[283] T. Prosen and M. Žnidarič. Quantum freeze of fidelity decay for a class of integrable dynamics. *New J. Phys.*, 5:109–109, aug 2003.